Dissertation
submitted to the
Combined Faculties for the Natural Sciences and for Mathematics
of the Ruperto-Carola University of Heidelberg, Germany
for the degree of
Doctor of Natural Sciences

Put forward by
M.Sc. Man Jiang
Born in Hulin (China)

Oral examination: 09. February 2017

Femtosecond UV Transient Absorption Study of Coumarin Dimers

Referees: Prof. Dr. Marcus Motzkus

Prof. Dr. Thomas Pfeifer

Abstract

The phenomena of photo-induced chemical reactions can exhibit kinetics as short as a few femtoseconds. The development of femtosecond UV pulses enables the investigation of such ultrafast phenomena in more experimentally challenging, UV absorbing systems. This thesis describes, chronologically, development of a UV transient absorption (TA) system and its application to various coumarin-based molecular systems. The experimental section details the TA system comprising of three major components: two tunable UV excitation sources giving a total excitation range of 250-350 nm, supercontinuum generation enabling 240-700 nm probe range, and multichannel detection with greater than 5×10^{-5} OD sensitivity. The potential of the TA setup was tested on the study of ultrafast relaxation in 7-hydroxy coumarin. Following successful tests, the photo-induced cleavage reaction of coumarin dimer was studied in order to understand the ultrafast dynamics. The experiments utilized 280 nm excitation and broadband (300-650 nm) probing. The results revealed fast cleavage occurring through short-lived nonradiative (<200 fs) singlet states. Two branched kinetic models were developed to describe the monomer formation and dimer relaxation dynamics, identify intermediate states, and determine the quantum yields. The anti-hh displayed the highest cleavage efficiency of ~20 %. Finally, variation in the quantum yields between isomers was rationalized using a sequential bond cleavage mechanism over a concerted, “pericyclic-style” ring cleavage.

Kurzzusammenfassung

Die Phänomene photoinduzierter chemischer Reaktionen können eine Kinetik innerhalb einiger Femtosekunden aufweisen. Die Entwicklung von Femtosekundenimpulsen im UV erlaubt die Erforschung solcher ultraschnellen Phänomene an experimentell herausfordernden, UV absorbierenden Systemen. In dieser Arbeit sind chronologisch die Entwicklung eines Systems für UV transiente Absorption (TA) und seine Anwendung an verschiedenen Cumarin-basierten molekularen Systeme beschrieben. Der experimentelle Teil erläutert das TA-System, das drei Hauptkomponenten umfasst: zwei durchstimmbare UV Anregungsquellen mit einem Gesamtspektrum von 250-350 nm, die Erzeugung eines Superkontinuums von 240-700 nm als Probeimpuls und die Multikanaldetektion mit einer Sensitivität größer als 5×10^{-5} OD. Das Potential des TA-Aufbaus wurde im Rahmen einer Studie der ultraschnellen Relaxation in 7-Hydroxycumarin überprüft. Nach erfolgreichen Tests wurde die photoinduzierte Spaltungsreaktion von Coumarindimeren untersucht mit dem Ziel die ultraschnelle Dynamik im Detail zu verstehen. In den Experimenten wurde ein Anregungsimpuls bei 280 nm und ein breitbandiger Probeimpuls (300-650 nm) verwendet. Die Ergebnisse lassen eine schnelle Spaltungsreaktion erkennen, die über kurzlebige strahlungslose (<200 fs) Singulettzustände stattfindet. Zwei verzweigte Kinetikmodelle wurden entwickelt, um die Erzeugung des Monomers und die Relaxationsdynamik des Dimers zu beschreiben, die Zwischenzustände zu identifizieren und die Quantenausbeute zu bestimmen. Das Isomer anti-hh weist die höchste Spaltungseffizienz von ~20 % auf. Abschließend konnte der Unterschied der Quantenausbeuten zwischen den Isomeren, basierend auf einem Mechanismus einer sequentiellen Bindungsspaltung anstelle einer geschlossenen, pericyclischartigen Ringspaltung begründet werden.

Contents

Chapter 1

Introduction

The phenomena of light-induced changes to molecular structure, function and composition has long been one of the classic, but imminently exciting scientific avenues. Photo-induced chemical reactions play a crucial role in the function of many natural systems, such as displayed in photosynthesis, and now find ever increasing use in modern photovoltaic and optoelectronic technologies. They are capable of proceeding at extremely short timescales, the shortest of which are over in a few femtoseconds. The study of such events requires spectroscopic methods with sufficient time resolution being able to "freeze" the molecular structure far from equilibrium, and prior to their vibrational and rotational modes of relaxation.[1] Ahmed Zewail and his group were the first to successfully realize the capability of ultrashort, laser pulse physics and developed a new research field, which is now known as "femtochemistry" (Figure 1.1).[2-4] Nowadays a variety of advanced time-resolved spectroscopic techniques, ranging from the ultraviolet (UV) through to the deep infrared (IR), have been developed in order to understand the nature of molecular dynamics, and characterize the photochemistry of molecules.

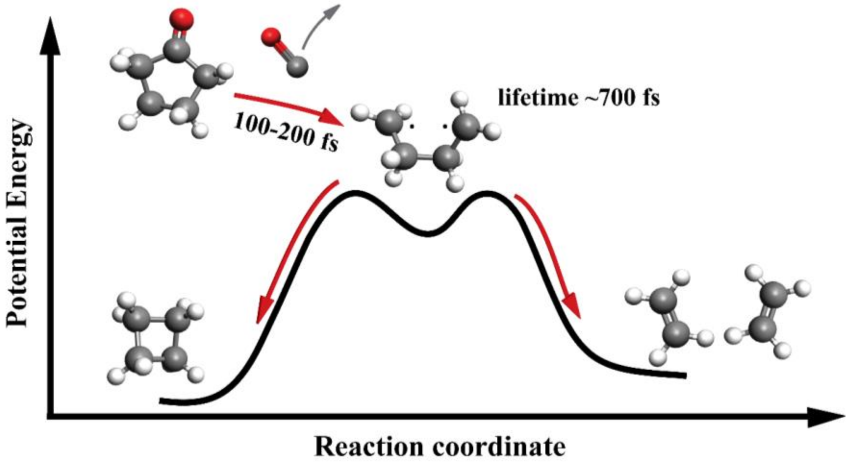

Figure 1.1: The ring opening of a cyclobutane molecule to form two ethylene molecules. Zewail and his co-workers showed with femtosecond spectroscopy that first one bond breaks and tetramethylene as an intermediate is formed in 100-200 fs and has a lifetime of about 700 fs.[4]

UV irradiation is best known for its detrimental effects on organic compounds, particularly upon prolonged sunlight exposure. However, UV radiation can also have a beneficial effect and be used to initiate desired chemical reactions. For example, one of the detrimental effects of UV irradiation on the biosphere is the formation of cyclobutane-based DNA lesions (Figure 1.2), which has been considered to be the major cause of DNA damages and high rates of skin cancer.[5] However, upon specific UV irradiation the DNA lesions can also be repaired with high efficiency by a light-driven photolyase using electron donor and electron acceptor photosensitizers (Figure 1.2).[6, 7] A large variety of photoactive molecules have their absorption in the UV spectral domain. The typical absorption ranges of some important classes of organic compounds are listed in Table 1.1, which are constituents of bio-molecules, many molecular devices and supra-molecular structures. Molecules based on these basic compounds are of significant importance for synthetic chemistry, as well as biological and technical processes. For example, the photosynthesis of vitamin D and vision processes in pigments rely on electrocyclic ring opening and closing reactions.[8, 9] Retinal proteins are among the most popular examples of bio-photosensors, where light-induced redistribution of charge on the chromophore drives the structural changes needed for the biological function. The sensitivity of retinal increases exponentially into the UV, and thus in order to obtain the information of local charge reorganization during protein function UV spectroscopies are usually applied.[10] Besides the general interests in bio-oriented activities, UV irradiation is also capable of causing fast polymerization from a liquid resin into a solid polymer, and inducing the polymerization of reactive groups present in a solid polymer to achieve insolubilization, thus modify its physical properties.[11]

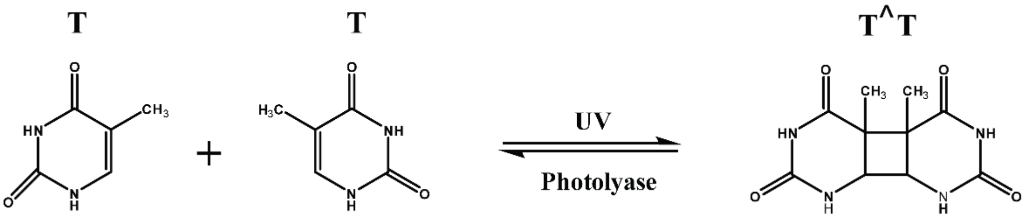

Figure 1.2: Under UV irradiation, the formation of thymine-thymine cyclobutane-pyrimidine dimers and their repair (reverse) reaction by the enzyme photolyase.

Table 1.1 Typical absorption range of some important classes of organic compounds[12, 13]

Molecule	Absorption range
1. Simple alkene	190-200 nm
2. Acyclic diene	220-250 nm
3. Cyclic diene	250-270 nm
4. Styrene	270-300 nm
5. Saturated ketones	270-280 nm
6. Aromatic compounds	250-280 nm

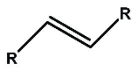

(1)

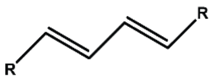

(2)

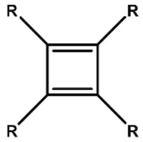

(3)

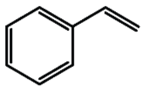

(4)

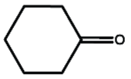

(5)

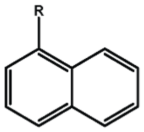

(6)

The development of ultrafast spectroscopic techniques has been supported by the availability of ultrashort laser pulses. UV-based femtosecond experiments are rarer than their visible and NIR counterparts due to technological limitations, many of which are materials related or rather UV compatible materials are still few in number. Consequently, few time-resolved groups utilize UV femtosecond optics. This is unfortunate as whilst the larger, more complicated visible-NIR absorbing systems are easy to experimentally probe, the simpler UV absorbing materials are substantially less easy to measure. Back to the early 90s, the first UV transient experiments were performed based on dye laser technology giving a time resolution of hundreds of femtoseconds to a few picoseconds.[14, 15] With the availability of mJ pulse energy, titanium sapphire (Ti:sapphire) amplifiers, femtosecond pulses can now be generated in different spectral ranges, with extension into the UV by nonlinear frequency up-conversion.[16, 17] However, no fine tuning was possible by frequency doubling or tripling of the amplifier's fundamental frequency, and the bandwidth of the generated UV pulses was not able to support pulse durations into the sub-100 fs regime. The realization of non-collinear optical parametric amplifiers (NOPA) changed all this. Broadband pulses with μJ pulse energies, which can support transform limits of < 10 fs became a reality with this advancement.[18] Most NOPA systems are designed to operate in the visible to NIR range (~ 500-1000 nm) but some have been tailored for UV generation. Utilizing frequency doubling or sum frequency generation of visible NOPA outputs, sub-30 fs pulses with tuning range from 200 nm to 350 nm can be efficiently generated.[19-21] However, high time resolution of time-resolved measurements call for even shorter pulses, which require broader spectral bandwidth. Recent advanced techniques of UV pulse generation mainly focus on how to overcome the bandwidth limits, which usually come at the expense of significant complication to the experimental setup, potentially making it unfeasible for robust, long term usage. In addition, pulse characterization in the UV is complicated by the short-wavelength absorption of nonlinear materials and unfavourable phase-matching conditions. Finally, the generation of broad probe pulses spanning from the deep UV extending to near IR is still not available, primarily due to the lack of suitable materials with high bandgap and high damage thresholds.

The aim of this thesis is two-fold. The first part describes in detail the successful construction of a high-quality, robust UV pump-probe setup. The main focus will be on the implementation of two NOPA apparatus for easy to tune, UV pump pulse generation. Two simple schemes outline the components of sum frequency generation (SFG) based NOPA and a second harmonic generation (SHG) based NOPA. Both are designed to efficiently generate UV pulses with enough pump energy for most molecular systems, and with sufficient bandwidth to support sub-30 fs pulse duration. In addition, to characterize the generated UV pulses, a compact autocorrelator based on two-photon absorption in a photomultiplier tube was developed.

In the second part, we demonstrate the application of femtosecond UV transient absorption to investigate the cleavage dynamics of coumarin dimers. The near UV/high energy (> 300 nm) photo-induced dimerization of coumarin is well-known to give the cyclobutane-based dimer molecule via the cycloaddition reaction (Figure 1.3). Conversely, mid to deep UV irradiation (< 280 nm) triggers the cycloreversion of the coumarin dimer back to the monomer form (Figure 1.3).[22] Generally, the photo-induced reaction of the cyclobutane ring is regarded to be pericyclic, which facilitates the scission and creation of chemical bonds within one step.[23, 24] In reality though, this reaction does not have to be concerted, but can proceed via the formation of intermediates (Figure 1.1).[4] The mechanism of cyclobutane-based reactions have long been a central topic in photochemistry as the cyclobutane unit is found as a basic structural element in a wide range of naturally occurring compounds, such as in bacteria, fungi, plants and skin.[25] In particular, cellular DNA strongly absorbs shorter-wavelength solar UV irradiation, resulting in various types of DNA damage, among which the cyclobutane pyrimidine dimers are predominant.[7] For the cyclobutane-based coumarin dimer, it has been found to be a valuable non-invasive therapeutic tool in the treatment of second cataract based on the photo-induced cleavage reaction of the cyclobutane ring.[26, 27] Using time-resolved spectroscopy to examine the underlying photocleavage dynamics of coumarin dimer is of crucial importance to understand and optimize the cleavage efficiency for its drug delivery applications. It is also very helpful to understand other cyclobutane-containing groups as studies of the cyclobuane amino acids and peptides are limited.

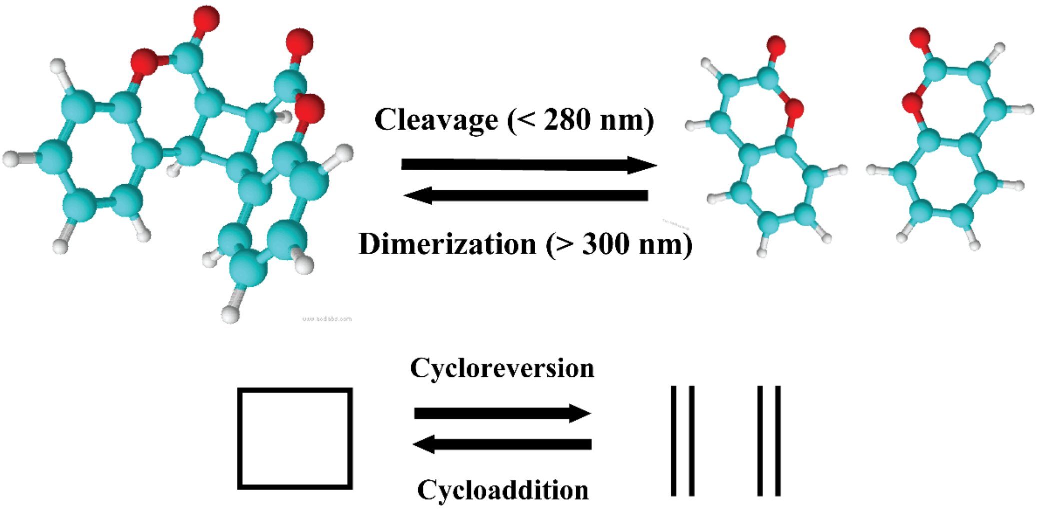

Figure 1.3: Upon direct irradiation of coumarin monomers with wavelength above 300 nm, a [2+2] cycloaddition reaction occurs, producing cyclobutane-based coumarin dimers. Under UV irradiation below 280 nm, the cyclobutane rings of dimer molecules undergo cycloreversion resulting in the monomer product.

Outline of the thesis

In **Chapter 2**, to obtain ultrashort UV pulses, two nonlinear up-conversion processes, sum frequency generation and second harmonic generation, are applied. Different from conventional configurations, the two UV generation schemes are improved in the consideration of conversion efficiency, spectral handling and group velocity mismatch. To characterize the generated UV pulses, a simple autocorrelator is introduced in **Chapter 3**, which is based on two-photon absorption in a photomultiplier tube. In order to confirm the reliability of the measured autocorrelation trace, an experimental verification is conducted for various fluences. Other aspects influencing the reliability and suitability of the autocorrelator, like window and photocathode material are also discussed. In **Chapter 4**, the supercontinuum generation is investigated for various condensed materials and pump wavelengths. The main focus is on how to broaden the anti-Stokes side of the supercontinuum spectrum. **Chapter 5** addresses the principal of the transient absorption (TA) experiment. All relevant components which play a role in building and running a femtosecond UV TA experiment are assembled to give a complete pump-probe system. Data processing and data analysis are elucidated. The entire pump-probe system, including the experiment measurement software, is tested in the study of the electronic levels and the dynamics of the excited state of 7-hydroxy coumarin. The experimental results of the cleavage reaction of coumarin dimer studied by UV transient absorption experiments is given in **Chapter 6**. The interpretation of the experimental data is supported by exponential analysis, singular value decomposition and global target analysis, from which two branched kinetic models are developed to describe the formation of monomers and dimer relaxation dynamics, to identify possible intermediate states, and to determine the quantum yields of the dimer splitting. Moreover, the effect of molecular structure on the quantum yield of cleavage reaction is analyzed by comparing the three isomers. A summary of the results and proposals for future experiments are given in **Chapter 7**.

Chapter 2

Generation of Sub-30 fs UV Pulses Tunable from 250 nm to 350 nm

The generation of ultraviolet (UV) pulses with sufficiently short pulse duration is the key prerequisite for the successful realization of femtosecond time-resolved spectroscopy in the UV spectral domain. This chapter starts with a background information regarding the development of UV pulse lasers, in particular recent advances in ultrashort UV solid-state amplifiers. Following this, two UV nonlinear parametric amplifier (NOPA) systems based on the sum frequency generation (SFG) and the second harmonic generation (SHG), respectively, are discussed in detail. For the SFG UV NOPA, different arrangements of the visible and NIR pulses are discussed with respect to the conversion efficiency. The physical effects influencing conversion efficiency and pulse duration for the SHG UV NOPA, such as dispersion compensation and group velocity mismatch (GVM), are discussed with the simulation. The final section briefly summarizes the basic features of the two UV NOPAs.

2.1 The development of ultrafast UV pulses

Over the last decades, due to the introduction of new gain materials, mode-locking and amplification techniques, there have been spectacular developments in ultrafast laser technologies. However, the development of ultrashort pulses in the UV domain has been a challenge, mainly due to the scarcity of nonlinear optical materials possessing suitable optical and mechanical characteristics for the UV spectral region. Moreover, direct sources being able to generate UV pulses with femtosecond duration remain unavailable. Therefore, generation of ultrashort UV pulses has to make use of readily available longer wavelength pulses, such as visible and NIR pulses, by frequency up-conversion processes (Figure 2.1). Recently, experimental approaches and theoretical studies of UV pulses have been focusing on increasing conversion efficiencies and shortening pulse durations. So far, there have been two well developed media for generating ultrashort UV pulses: one is gas, and the other is solid-state material.

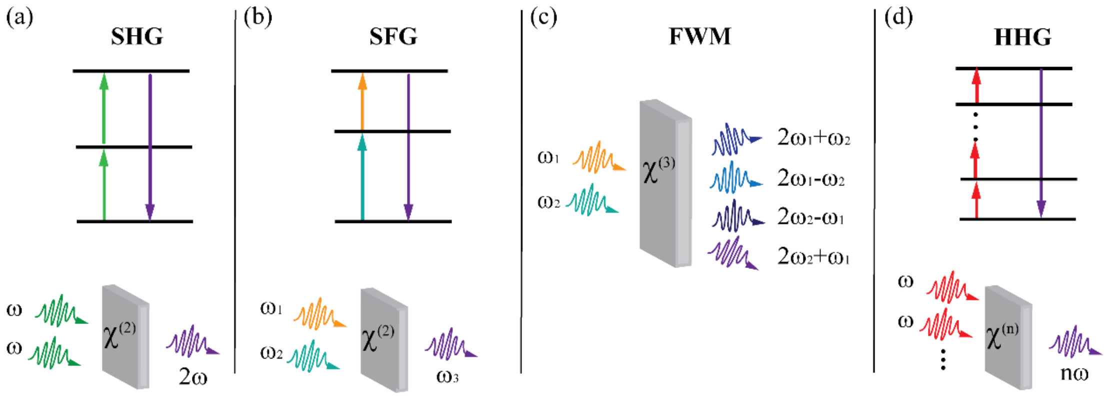

Figure 2.1: Frequency up-conversion processes in an optical medium possessing (a, b) quadratic $\chi^{(2)}$, (c) cubic $\chi^{(3)}$, and (d) higher order nonlinear susceptibility $\chi^{(n)}$. (a) Two electromagnetic waves with the same frequency ω, generate a higher frequency wave with a frequency of 2ω by the SHG; (b) two electromagnetic waves with frequencies ω_1 and ω_2 can generate a wave with frequency $\omega_3=\omega_1+\omega_2$ by SFG; (c) two photons with frequencies ω_1 and ω_2 are converted into higher frequency photons by four wave mixing (FWM), depending on the phase-matching conditions; (d) high harmonic generation (HHG) gives a output wave with a frequency of nω.

Gas has been successfully applied in the ultrashort UV generation because it can avoid complications such as a finite phase-matching bandwidth, which limits the obtainable pulse duration. By focusing 22 fs, 1-mJ fundamental 800 nm pulses in air, third harmonic UV pulses were generated.[28] Its advantages are the short pulse duration (16 fs) and the relative ease of implementation, but the conversion efficiency was only about 0.1 %. A higher conversion efficiency can be obtained with argon. Beutler et al. applied filamentation in argon to broaden the spectral bandwidth of third harmonic UV pulses from 1.4 nm to about 10 nm, leading to sub-20 fs UV pulses with ~ 7 % conversion efficiency.[29] In addition to argon, neon has been found to provide the highest output of the nondegenerate FWM signal at 260 nm with 12 fs pulse duration.[30] Down to wavelengths shorter than 250 nm, FWM in gases is a simple and efficient way to generate ultrashort pulses. Zuo and co-workers extended UV pulse generation down to 237 nm by spectral phase transfer through FWM process in neon gas.[31] The value of this approach is that the temporal width of the generated UV pulses were controlled by simple manipulation of the NIR pulse chirp, giving a 25 fs pulse duration without a complex compressor system. Moreover, compared to other UV generation techniques in gas phase, this method provided tunability of the output spectrum by tuning the center wavelength of the NIR pulses. However, the low nonlinear susceptibility of gas media is still the primary limitation to be applied widely in the generation of UV pulses.

The other frequency conversion medium is the solid-state nonlinear crystal, in particular the β-BaB_2O_4 (BBO) and LiB_3O_5 (LBO) family, which are the most commonly used frequency up-conversion nonlinear materials in the UV pulses generation because of their high nonlinear susceptibility and wide range of transparency.[32, 33] However, operation of BBO below 200 nm becomes challenging since its absorption edge is around 190 nm. So far, the $KBe_2BO_3F_2$ (KBBF) crystal is found to be the only solid material which can fulfil the stringent requirement of wide transparency in the deep UV, and therefore enable the harmonic generation down to 157 nm.[33-35] In general, a good nonlinear crystal for the generation of UV pulses should satisfy the following requirements: (1) large nonlinear coefficient, (2) large angular acceptance, (3) small spatial walk-off effect, (4) small linear and nonlinear absorption at the UV region, (5) high damage threshold, (6) good chemical and mechanical stability.[36] The most straightforward way for femtosecond UV pulse generation relies on direct second[37] or third harmonic generation[38], and sum frequency mixing[21, 39] of ultrashort pulses provided by optical parametric amplifiers (OPA) operating in the visible and NIR. However, large group velocity mismatch and narrow phase matching bandwidth limit the conversion efficiency and restrict the achievement of spectrally broad pulses. Efficient generation of tunable UV pulses under 50 fs is a non-trivial task. To overcome the bandwidth limit, some frequency conversion techniques have been successfully employed. Positively chirped NIR pulses mixing with visible pulses allowed the visible spectrum efficiently transfer to the UV region and therefore led to 20-30 fs UV pulses in a broad tuning range from 295-450 nm.[19] Various modifications of the achromatic phase-matching technique have been applied to the frequency doubling[20, 40] and sum frequency mixing[41] in BBO crystals, which improved ultraviolet pulse durations to 7 fs and 13.2 fs, respectively. The basic idea of the achromatic approach is that a broadband visible pulse is angularly dispersed such that each frequency component converts to the UV region at its individual phase matching angle, which can give an extremely broad UV spectrum. All the above mentioned UV generation schemes are based on the traditional type-I phase matching. For a BBO crystal, type I phase matching has the intrinsic advantage of a higher nonlinear coefficient. However, type-II phase matching provides a broader acceptance bandwidth for the ordinary beam and a narrower one for the extraordinary beam, thus allowing for more efficient energy conversion from the broad visible pulses to the UV. Manzoni et al. reported a sub-10 fs UV pulses generation by type II phase matching configuration.[42] In analogy to the visible pulse generation, a tunable UV pulse can also be achieved by employing direct OPA[43] or optical parametric chirped pulse amplification (OPCPA).[44, 45] However, intense deep UV pumping can induce nonlinear and thermal effects in the nonlinear crystal and optical elements. Finally, FWM allows the conversion of the visible pulses into the UV and amplification at the same time, which can be simply realized in the transparent solid medium, like fused silica[46] or CaF_2[47].

In addition to gases and solid media, for the enhancement of the conversion efficiency, hollow fibers filled with rare gas have been used.[48-51] However, this technique does not provide tunable light generation. There are also a number of excimer lasers which can emit in the deep UV spectral range under 200 nm, but mostly with a pulse duration of picoseconds to nanoseconds.[52-54]

2.2 Generation of sub-30 fs UV pulses by chirped sum frequency generation

In transient absorption spectroscopy, the fluctuation of the signal is typically three times larger than the energy fluctuation of the laser pulses,[55] hence, a stable light source is highly required. It is common to attribute the good stability of optical parametrically generated pulses to the stable input pulses and optical elements. SFG of UV pulses typically mixes NIR pulses at 800 nm with amplified visible pulses, therefore it can take full advantage of the stability of the commercial Ti:sapphire chirped pulse amplifier (CPA) system. However, the intensity of the input light and crystal length also impact on the stability of the output.[56] In order to achieve excellent pulse stability, a combination of crystal length and input parameters, such as spectral phase and polarization, has to be carefully chosen.

In SFG, two optical waves $\boldsymbol{E}(\omega_1, z)$ and $\boldsymbol{E}(\omega_2, z)$ with frequencies ω_1 and ω_2 generate a nonlinear polarization $\boldsymbol{P}^{(2)}(\omega_3)$ at the frequency $\omega_3 = \omega_1 + \omega_2$ in the second-order nonlinear medium with a nonlinear susceptibility $\boldsymbol{\chi}^{(2)}(\omega_1, \omega_2)$ (Figure 2.2 (a)), which can be expressed as[57]:

$$\boldsymbol{P}^{(2)}(\omega_3) = 2\varepsilon_0 \boldsymbol{\chi}^{(2)}(\omega_1, \omega_2) : \boldsymbol{E}(\omega_1, z)\boldsymbol{E}(\omega_2, z) \tag{2.1}$$

The incident pair of waves at frequency ω_1 and ω_2 can also produce polarization densities at frequencies $\omega_1 - \omega_1$, $\omega_1 + \omega_1$, $\omega_2 - \omega_2$, $\omega_2 + \omega_2$ and $|\omega_1 - \omega_2|$, however, not all of these waves are necessarily generated, as certain phase matching conditions must be satisfied. The process of wave mixing involves energy exchange among the interacting waves. Photon energy and momentum conservation require the conditions $\omega_3 = \omega_1 + \omega_2$ and $\boldsymbol{k}_1 + \boldsymbol{k}_2 = \boldsymbol{k}_3$, respectively. For the most efficient energy transfer amongst the waves, one naturally expects that both photon energies and momentum conservations should be satisfied in the wave interaction. In the course of frequency up-conversion, two low frequency photons ω_1 and ω_2 are annihilated, and one high frequency photon ω_3 is gained. The photon momentum condition is known in nonlinear optics as the phase matching condition (Figure 2.2 (b)). The phase matching condition also can be easily understood from the concept of energy transfer.

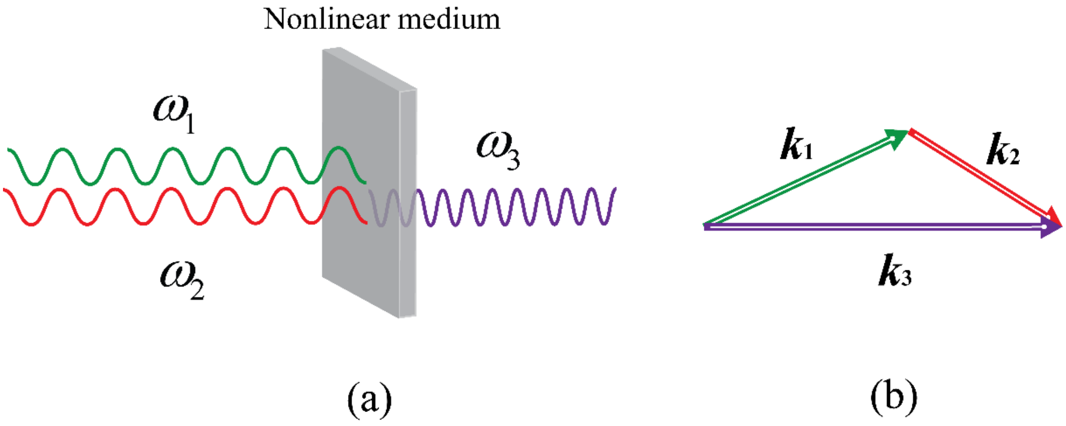

Figure 2.2: (a) The interaction of two incident waves with frequencies ω_1 and ω_2 generates a wave with frequency $\omega_1+\omega_2=\omega_3$, (b) the phase matching condition of $\boldsymbol{k}_1+\boldsymbol{k}_2=\boldsymbol{k}_3$.

For simplification, we represent the electric field $\boldsymbol{E}(\omega_n, z)$ with the form of quasi-monochromatic plane wave by $\boldsymbol{E}(\omega_n, z) = E(\omega_n, z)\boldsymbol{a}e^{ik_n z}$, where $\boldsymbol{k}_n$ and E_n (ω_n, z) are the wave vector and the envelope of the electric field, and $\boldsymbol{a}$ is the unit vector of the electric field. The coupled complex equations for slowly varying envelopes of the laser fields E_1 (ω_1, z), E_2 (ω_2, z), and the nonlinear signal E_3 (ω_3, z) are written as[57]

$$\frac{dE(\omega_1, z)}{dz} = \frac{\mathrm{i}2\pi\omega_1^2}{k_1c^2}\chi_{eff}^{(2)}E(\omega_3, z)E^*(\omega_2, z)e^{-\mathrm{i}\Delta \mathrm{k}z} \tag{2.2}$$

$$\frac{dE(\omega_2, z)}{dz} = \frac{\mathrm{i}2\pi\omega_2^2}{k_2c^2}\chi_{eff}^{(2)}E(\omega_3, z)E^*(\omega_1, z)e^{-\mathrm{i}\Delta \mathrm{k}z} \tag{2.3}$$

$$\frac{dE(\omega_3, z)}{dz} = \frac{\mathrm{i}2\pi\omega_3^2}{k_3c^2}\chi_{eff}^{(2)}E(\omega_1, z)E^*(\omega_2, z)e^{-\mathrm{i}\Delta \mathrm{k}z} \tag{2.4}$$

where $\chi_{eff}^{(2)}$ is the effective nonlinear coefficient which determines the rate of energy transfer among the three waves. $\boldsymbol{k}_1$, $\boldsymbol{k}_2$ and $\boldsymbol{k}_3$ are wave vectors of the fields with frequencies ω_1, ω_2 and ω_3, respectively, and $\Delta\boldsymbol{k} = \boldsymbol{k}_1+\boldsymbol{k}_2-\boldsymbol{k}_3$ is the wave-vector mismatch.

We consider SFG in the non-depletion regime, in which the intensity of the generated high frequency beam is so low that the intensities of the incident laser fields ω_1 and ω_2 are assumed to remain during the interaction. Then the solution of Equation (2.4) yields

$$E(\omega_3, z) = \frac{2\pi\omega_3^2}{k_3 c^2 \Delta k} \chi_{eff}^{(2)} E(\omega_1, 0) E(\omega_2, 0) \left(e^{-i\Delta kz} - 1\right). \tag{2.5}$$

We can write Equation (2.5) as

$$E(\omega_3, z) = \frac{2\pi\omega_3^2}{k_3 c^2 \Delta k} \chi_{eff}^{(2)} E(\omega_1, 0) E(\omega_2, 0) \sin\left(\frac{\Delta kz}{2}\right) e^{-i\Delta kz/2}. \tag{2.6}$$

The intensity of SFG output can be determined from the electric field as

$$I_3 = \left(\frac{2\pi\omega_3^2}{k_3 c^2 \Delta k} \chi_{eff}^{(2)}\right)^2 I_1 I_2 \sin^2\left(\frac{\Delta kz}{2}\right) \tag{2.7}$$

Equation (2.7) shows that the intensity of the generated wave depends on the intensity of the incident waves, and the effective coefficient of the crystal. Only when $\Delta k \rightarrow 0$, $\sin^2(\Delta kz/2) \rightarrow (\Delta kz/2)^2 = (z/z_c)^2$, where $z_c = 2/\Delta k$ is defined as the coherence length, the intensity of the generated sum frequency grows as a quadratic function of the length z of the nonlinear medium. If the phase matching is not satisfied, the phase of $E(\omega_3, z)$ is z dependent, which means all generated radiation contributions from different z positions with a thickness unit of Δz in the crystal cannot be added coherently, or they may even cancel each other out leading to a low output.

The phase matching condition $\boldsymbol{k}_1+\boldsymbol{k}_2=\boldsymbol{k}_3$ can also be expressed as $\omega_1 n_1 + \omega_2 n_2 = \omega_3 n_3$ which can never be satisfied in isotropic or cubic materials with normal dispersion properties, $n(\omega_3) > \{n(\omega_1), n(\omega_2)\}$. Therefore, collinear phase matching can only be achieved with anomalous dispersion or birefringent crystals.[58] The dispersion of nonlinear media not only limits the energy transfer efficiency, but also affects the bandwidth of the frequency conversion. If the phase-matching requirement is satisfied for the central frequencies $\omega_1^c n_1^c + \omega_2^c n_2^c = \omega_3^c n_3^c$ then it will not be equally satisfied for most other pairs of interacting frequencies because the refractive index is frequency dependent. (Figure 2.3). When $\Delta k > \pi/z_c$, the process of SFG vanishes.

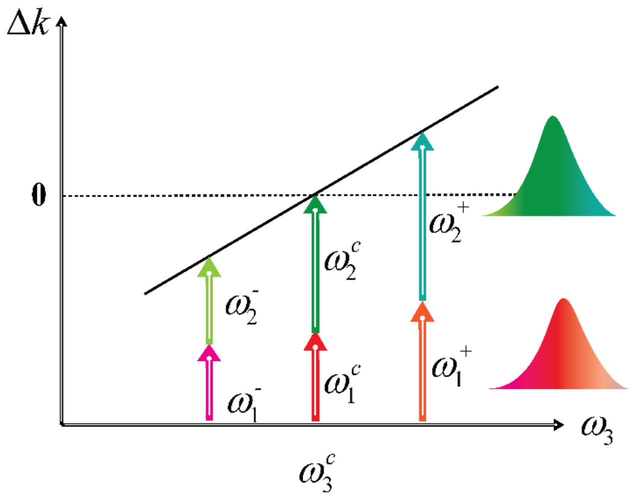

Figure 2.3: Phase matching condition scheme for SFG. The phase matching condition Δk=0 is satisfied with the frequency pair ω_1^c and ω_2^c, while for other pairs $\Delta k \neq 0$.

2.2.1 Chirped SFG

There are three possible schemes for SFG arrangement of the incident waves, which in our case are NIR pulses at 800 nm and visible pulses from the NOPA (Figure 2.4).

One can assume that well compressed incident pulses should also render short output pulses. If all wave components are assumed to have Gaussian temporal profiles, the pulse duration of the generated wave can be estimated as[59]

$$\frac{1}{\tau_3^2} = \frac{1}{\tau_1^2} + \frac{1}{\tau_2^2} \tag{2.8}$$

where τ_1, τ_2 and τ_3 are the pulse durations of the laser fields with frequencies ω_1, ω_2 and ω_3, respectively. In the arrangement shown in Figure 2.4 (a), a NIR pulse mixes with a compressed visible pulse, the pulse duration of the high frequency pulse is dominated by the visible pulse which renders the output pulse a duration of about 20 fs. However, because of the dispersion in the nonlinear crystal, the output pulse still needs to be further compressed which adds complexity to the experimental setup. Furthermore, a large part of the energy of the NIR pulses is wasted because of the poor temporal overlap between the two interacting pulses.

An improved arrangement is shown in Figure 2.4 (b), which reduces the number of required compressors to be just one. One shortcoming of this arrangement is that, the duration of the visible pulse is slightly longer than the NIR pulse so the frequency components at the spectral wings cannot be converted to the UV, resulting in a narrower bandwidth.

In the third arrangement shown in Figure 2.4 (c), the NIR pulse is positively chirped to a duration well overlapped with the visible pulse. Although the generated UV bandwidth is mainly affected by the dispersion induced group velocity mismatch, as well as the acceptance bandwidth of the nonlinear crystal, a good temporal overlap between the NIR pulse and the visible pulse enables a generated UV pulse with sufficient bandwidth which potentially supports sub-20 fs pulse duration. Additionally, this arrangement provides a high conversion efficiency and simplifies the adjustment by using only one compressor. Further increasing the pulse duration of the NIR pulse to be even longer will not improve conversion efficiency as the low peak intensity does not support high energy transfer. Based on the third arrangement, the schematic of the nonlinear mixing scheme in our experiment, and the relevant pulse parameters are shown in Figure 2.5.

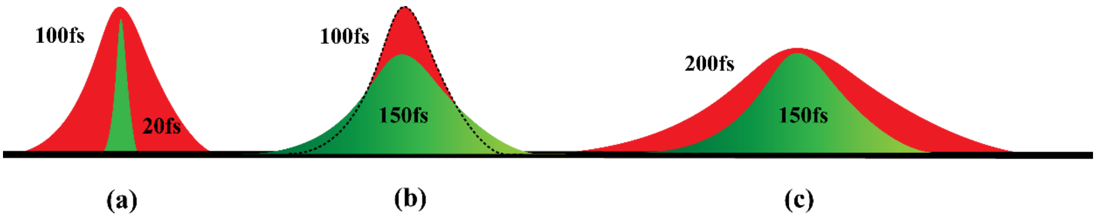

Figure 2.4: (a) Compressed visible pulses mixing with NIR pulses, (b) uncompressed visible pulses mixing with NIR pulses, (c) uncompressed visible pulses mixing with stretched NIR pulses.

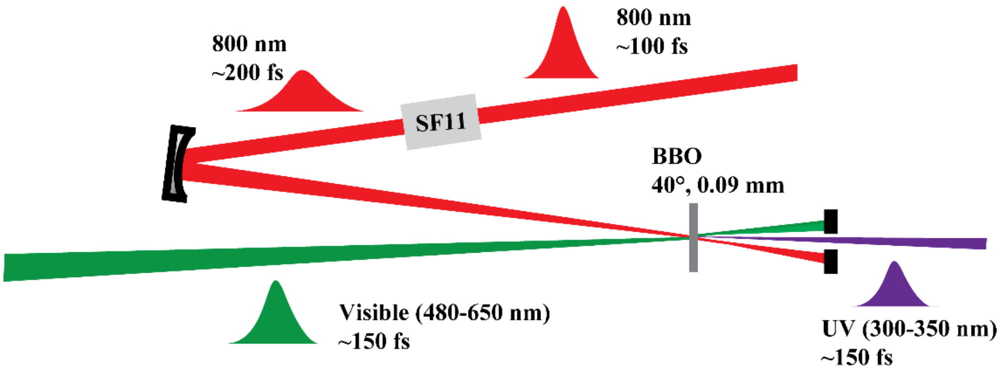

Figure 2.5: Schematic of the nonlinear mixing scheme. A chirped NIR pulse mixes with a visible pulse to generate a UV pulse. The relevant pulse parameters are indicated.

2.2.2 Experimental realization and characterization

The SFG NOPA (Figure 2.6) is fed by a regenerative Ti:sapphire amplifier system (CPA 1000 Clark-MXR) which delivers 640 µJ/pulse at 800 nm with a repetition rate of 1kHz. Briefly to describe the NOPA, a few µJ of the Ti:sapphire fundamental is used for the generation of a supercontinuum by focusing into a 2 mm sapphire plate. A selected spectral component of the supercontinuum is amplified in a 1 mm BBO crystal. The first-stage amplifier gives a major contribution to the stability and beam profile of the final visible output energy. A thicker 2 mm BBO crystal is used in the second amplifier stage. Tuning the intersection angle between the pump and the seed, and the phase matching angle of the BBO make it is possible to obtain the output with 12 µJ energy and a tunable range from 490 nm to 660 nm. The spectral bandwidth of the NOPA pulses can be controlled by changing the chirp of the supercontinuum and the phase matching angle of the nonlinear crystal. After transmission through the lenses and nonlinear crystals, the visible pulse is positively chirped to a pulse duration of more than 150 fs. To achieve better temporal overlap between the NIR and visible pulses, we add extra positive chirp to the NIR pulses by sending it through a block of glass (SF 11, 4 cm) leading to a pulse duration of about 200 fs. A BBO crystal with a cutting angle of 40.5° and 90 µm thickness is used to mix the visible and NIR pulses. After synchronizing the visible and NIR with a mechanical delay stage, the two beams are focused and overlapped in the crystal with a 3° beam intersection angle which is sufficient to spatially select the UV output whilst maintaining beam overlap inside the crystal. To avoid permanent damage on the crystal, the BBO is located 2 cm behind the focuses of both beams. To compress the UV pulses to a minimum duration, a fused silica prism pair is chosen because of its transparency in the UV range. Considering the polarization dependence from the Fresnel reflection, the polarization orientations of both visible and NIR pulses are rotated to S-polarization by using half-wave plates, thus the reflection losses are minimized for P-polarized UV output at Brewster's angle during the compression. The distance between the two prisms varies between 40 and 60 cm depending on the tuning range of the spectrum. An aluminium mirror is used at the end as the folding mirror, so that the beam exiting the second prism travels back in the same vertical plane as the entering beam.

The SFG-NOPA system produces UV pulses (Figure 2.7 (a)) with energy up to 2 μJ tunable from 300 to 350 nm (Figure 2.7 (b)). The frequency conversion efficiency is about 16 %. The output energy can be increased by repositioning the BBO crystal close to the focus region to change the pump intensity. This will also influence the output beam profile and divergence. By adjusting the position of the BBO crystal towards the focus, a FWM signal around 420 nm is observed (Figure 2.7 (a)). In the application of transient absorption measurements, our system is not optimized for maximum output power, but for optimal quality of the beam profile and short pulse duration. The typical throughput of fused silica prisms in the UV region is about 55 %, giving ~1 μJ UV output after compression. Adjusting the time delay between the two incident pulses only varies the output intensity. No evident spectral tuning is observed because of the narrow bandwidth of the NIR pulse. All generated UV pulses display spectral bandwidths of 6-8 nm (Figure 2.8 (a))

The pulse duration of the UV output is characterized via two-photon absorption autocorrelation in a photomultiplier tube, which will be elaborated in the following chapter of UV pulse characterization. To determine the pulse duration from the autocorrelation curve, the UV pulse is fit with a Gaussian distribution. The fitting shows no satellite pulses or detectable shoulders, which indicates that there is no spectral components with high order chirp (Figure 2.8 (b)). The measured pulse is almost transform-limited ($\Delta\nu\Delta\tau = 0.44$). The ~9 % above the Fourier limit is due to the dispersion in the MgF_2 window of photomultiplier tube. The pulse duration varies from 26 to 32 fs for different spectral range. At the cost of output energy, broader spectral width is possible with a thinner BBO crystal, and therefore a shorter pulse duration can be obtained.

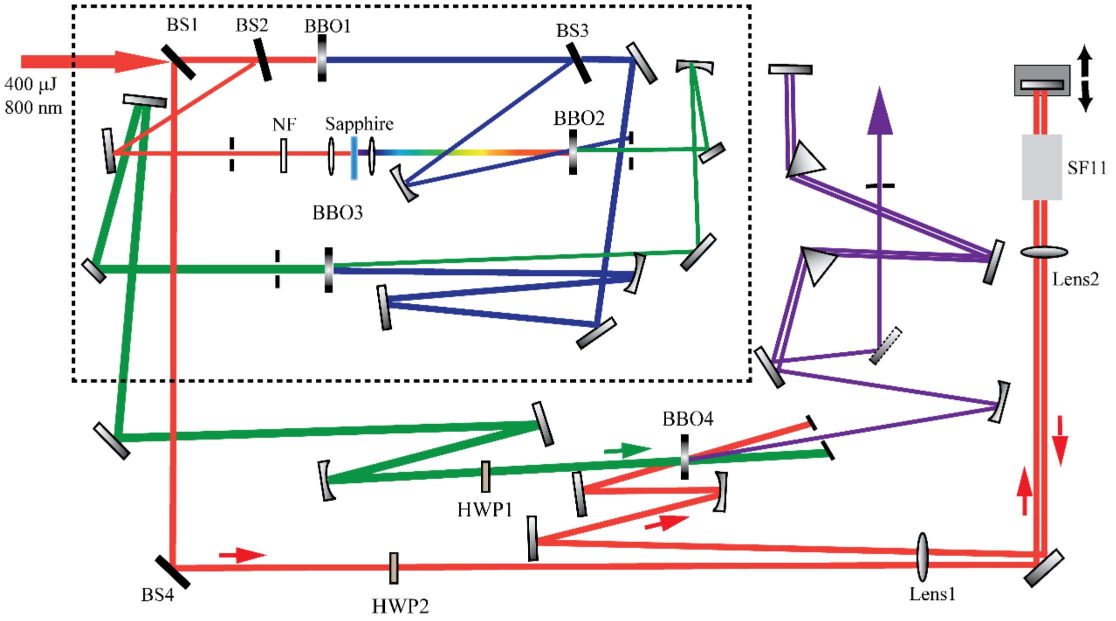

Figure 2.6: Experimental setup for SFG based on chirped NIR pulses is as following: 400 µJ pulses at 800 nm is used to pump the whole system which includes a two-stage visible NOPA (marked with dashed line) and one stage of frequency mixing of the visible pulses and NIR pulses. The energy distribution of the fundamental input pulses is: 25 % (100 µJ) is split off and contributes to the final SFG-UV generation, 5 % (15 µJ) of the transmitted pulses are used to generate supercontinuum serving as the seed light for the first-stage NOPA (preamplifier), and the remainder (285 µJ) is frequency converted to 400 nm serving as the pump light for the two-stage amplifier. The bandwidth of the NOPA output is about 45 nm. A fraction of the 100 µJ fundamental pulses is sent through a 4 cm SF11 block. To avoid optical damage and degradation of the glass block, a telescope system based on Lens1 and Lens2 is used to double the beam size of the NIR. The uncompressed NOPA output and stretched NIR pulses are polarization-rotated by half-wave plates and focused into a 90-µm-thick BBO crystal (θ=40.5°) for type I non-collinear SFG. The beam intersection angle is about 3°. To compress the UV pulses to a minimum duration, a double-pass prism pair is used.

BS1: 25 % reflection beam splitter, BS2: 5 % reflection beam splitter, BBO1: 0.5 mm thickness, cutting angle of 29.2°, BS3: 20 % reflection beam splitter, NF: neutral density filter, BBO2: 1 mm thickness, cutting angle 32.5°, BBO3: 2 mm thickness, cutting angle of 32.5°, BS4: 80 % or 50 % reflection beam splitter, HWP1: achromatic half-wave plate, HWP2: half-wave plate at 800 nm, BBO4: 0.9 mm thickness, cutting angle of 40.5°, Lens1: convex lens with 10 cm focal length, Lens2: concave lens with 5 cm focal length.

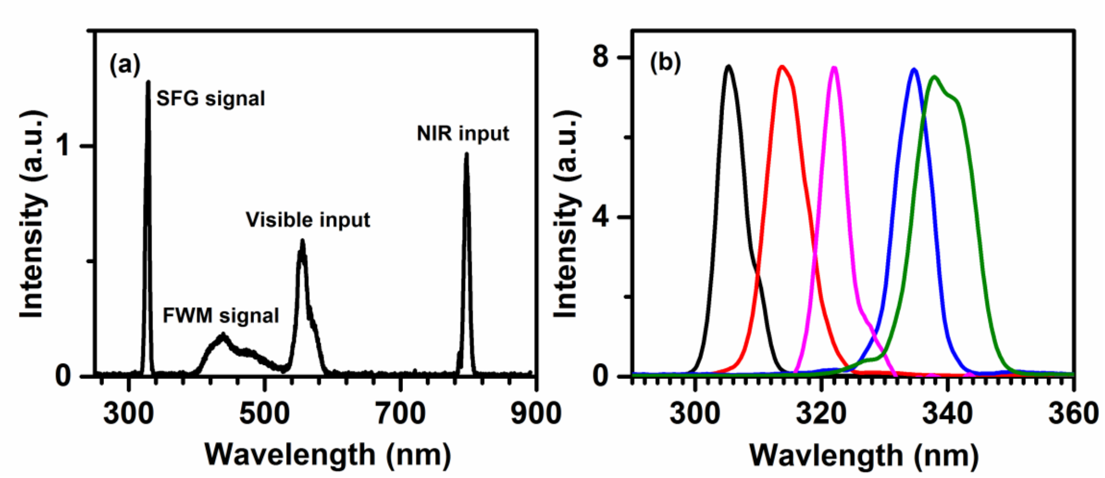

Figure 2.7: (a) SFG with cascaded FWM of $2\omega_{vis}$-ω_{NIR}, (b) UV pulse spectra in the tuning range from 300 to 350 nm.

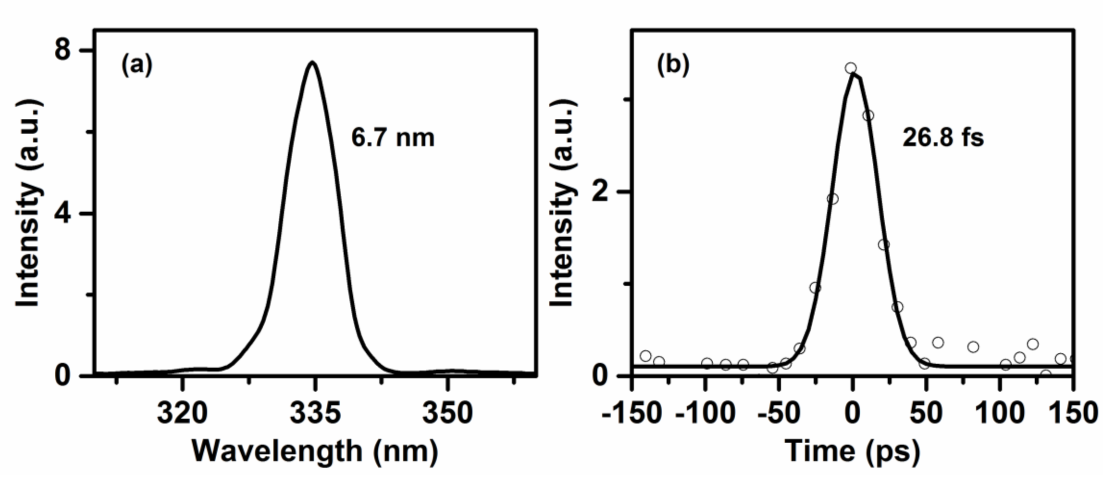

Figure 2.8: (a) Spectrum of UV output at 334 nm with a bandwidth of 6.7 nm, giving a transform-limit duration of 24.5 fs. (b) Autocorrelation trace at 334 nm with a temporal width of 26.8 fs. The open dots are experimental data and the solid line is the Gaussian fit.

2.3 Generation of UV pulses from 250 to 300 nm by frequency doubling

2.3.1 Dispersive compensation

In the SHG, an incident wave with a frequency ω generates a signal at the frequency 2ω as it propagates through a nonlinear medium. The mechanism and theory of SHG process follow exactly that of SFG discussed in the previous section, and it also has the same limiting effects, such as dispersion induced phase mismatch and phase distortion. Spectral phase distortion which pre-exists in the input fundamental pulses, commonly as quadratic phase (linear chirp) or in rare case higher order phases, results in broadening of the SH pulses and low conversion efficiency. It is well known that, the phase distortions can be removed by dispersive compensation, either in the fundamental pulses or in the SH pulses.[60, 61]

There are three possible schemes of spectral phase compensation in SHG (Figure 2.9). All three schemes have been experimentally applied in the generation of ultrashort pulses.[37, 40, 62-64] Depending on the chosen scheme, the fundamental pulses may be transformed differently during frequency doubling in terms of conversion efficiency and the output pulse duration. For the generated signal in the visible range, all three schemes are able to remove the chirp identically and therefore result in the same transform-limited SH pulses. However, for the generation of UV pulses, the high oscillation frequency induces severe dispersion in the nonlinear medium, especially in thick crystals, thus different schemes will behave distinctively.

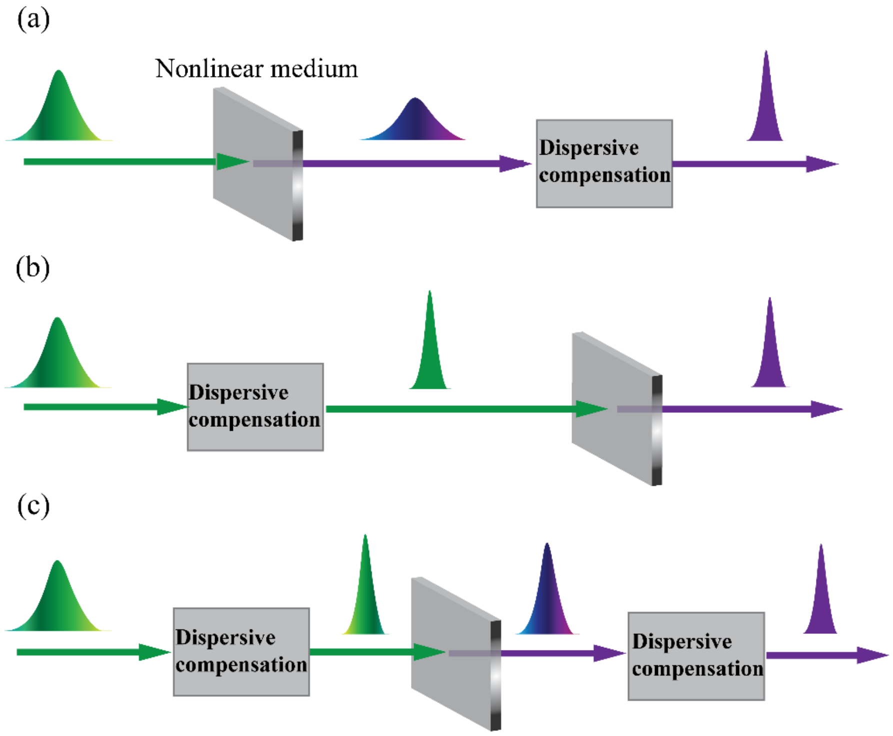

Figure 2.9: Dispersion compensation schemes used in SHG (a) compensation performed in the SH pulses, (b) pre-compensation in the fundamental pulses, (c) compensation in the SH pulses after pre-compensation of the fundamental pulses.

A detailed theoretical and qualitative description of SHG using transform-limited or non-transform-limited fundamental pulses is given by Sidick and coworkers.[60, 61] To simplify the model, in the following discussion we only consider the quadratic spectral phase from the fundamental pulses and internal dispersion of the nonlinear crystal, which are the primary contributors to pulse broadening. For a fundamental pulse centered at the frequency ω_0 with only quadratic spectral phase, it can be expressed with a Gaussian shape:

$$E(\omega) = E_0 \exp\left[\frac{-(\omega-\omega_0)^2}{2\sigma^2}\right]\exp\left[i\Phi(\omega)\right] \tag{2.9}$$

where σ is the spectral width, $\Phi(\omega)$ is the spectral phase which can be written as

$$\Phi(\omega) = A(\omega-\omega_0)^2 \tag{2.10}$$

where A is the coefficient of the linear chirp. Substituting Equation (2.9) and (2.10) into (2.5), the SH field in the frequency domain can be expressed as[40]

$$\left|E_{SH}\left(\omega\right)\right|^2 \propto \sin c^2\left(\frac{\Delta kz}{2}\right)\frac{\sigma^{-2}}{\sqrt{\sigma^{-4}+4A^2}}\exp\left(\frac{-\left(\omega-2\omega_0\right)^2}{2\sigma^2}\right), \tag{2.11}$$

and the spectral phase is

$$\Phi_{SH}(\omega)=\frac{1}{2}A(\omega-2\omega_0)^2. \tag{2.12}$$

Comparison of Equation (2.12) and (2.10) shows for a Gaussian pulse with linear chirp, the SH process reduces the coefficient of linear chirp by half. This result is based on the assumption that GVM doesn’t play a major role in SHG. If cubic spectral phase is taken into consideration, the coefficient is reduced by a factor of 4 in SH process.[40] Although the SH process, can suppress linear and higher-order chirps, to some extent, to achieve transform-limited pulses further compensation is still necessary (Figure 2.9 (a)). If Gaussian input pulses exhibits purely with quadratic spectral phase, the final SH pulse shape and duration are independent of whether the dispersive compensation is performed in the fundamental pulse or the generated SH pulse. However, pulse shortening is found to be limited by a residual higher-order spectral phase in the compressor stage,[64] which cannot be compensated by using well-known methods of dispersive compression, e.g. prism pair. For pulses in the UV range, due to higher order dispersion in optical materials and also to the lack of suitable chirped mirrors, dispersion compensation after SH process is more challenging than in other spectral ranges. Therefore, for SH-based UV pulse generation, pre-compensation of the fundamental pulses (Figure 2.9 (b)) is more advantageous than the compensation of the SH pulses. Moreover, from the point of conversion efficiency, pre-compensation increases the peak intensity of the fundamental pulse and thus results in a higher conversion efficiency.

2.3.2 Group velocity mismatch in SHG

For UV pulse generation, GVM can severely affect the conversion efficiency and pulse duration of the output pulses. In the case of SHG, group velocity mismatch can be quantitative expressed as

$$\mathrm{GVM} = \left(\frac{1}{\upsilon_{2\omega_0}} - \frac{1}{\upsilon_{\omega_0}} \right) \tag{2.13}$$

where $\upsilon_{2\omega_0}$ and υ_{ω_0} are the group velocities of the SH pulse and the fundamental pulse. The group velocity is wavelength and refractive index dependent, given by

$$\upsilon(\lambda) = \frac{c}{n(\lambda) - \lambda \dfrac{dn(\lambda)}{d\lambda}} \tag{2.14}$$

where c is the velocity of light in vacuum, and $n(\lambda)$ is the refractive index at wavelength λ.

In fact, the transform-limited SH pulse does not occur at exact phase cancellation from the pre-compensation. When the input pulses with minimum pulse duration propagate through the nonlinear crystal, the spectral phase will be further distorted, and the spectral distortion is transferred to the SH pulses leading to pulse broadening. The GVM causes the fundamental pulses and growing SH pulses to undergo temporal drift from each other while traversing the crystal, creating broader SH pulse with increasing interaction length. Moreover, due to the GVM, the SH pulse lags behind the fundamental. When the temporal interval of the two interacting waves reaches to the pulse duration of either, the SH process is suppressed. To compensate the broadening in the SH process, a second compensator can be applied, although it makes the tuning difficult when the central wavelength is changed (Figure 2.9 (c)). Another way to preserve the pulse duration during frequency doubling of femtosecond pulses requires the use of very thin nonlinear crystals. For UV pulses in the 20 fs regime with centre wavelength of 270 nm, the preservation of pulse duration and minimization of the temporal walk-off would require a crystal thinner than 50 μm. However, as we discussed in the section of SFG, the intensity of the generated signal is proportional quadratically to the thickness of nonlinear medium. Minimum pulse duration of the SH pulse is at the cost of conversion efficiency. In order to obtain short SH pulses with high conversion efficiency, a suitable combination of crystal length and dispersion compensator should be carefully chosen.

A simulation was performed to study the effect of spectral phase on the pulse duration and the output energy. The simulation is based on the Lab2 program from LAB2-A virtual femtosecond laser lab by using a non-depleted fundamental wave approximation.[65] Simulated UV spectra with varying degrees of quadratic spectral phase added to the transform-limited fundamental pulses are shown in Figure 2.10. The approximation is valid for small conversion efficiency, which requires a thin nonlinear crystal and low intensity of the input pulses. The fundamental input is set to be centered at 560 nm with 30 nm bandwidth and 1 μJ per pulse. We applied type I phase matching in a 55 μm BBO crystal, and the cutting angle was intentionally set to be 44.3°, in order to maximize the conversion efficiency at 560 nm and minimize the phase mismatching. As such, the only influential factors are the GVM and the limited spectral acceptance of the crystal. The material dispersion in the 55 μm BBO crystal can be neglected. For example, the SH pulses at 280 nm with a Fourier limit of 16.6 fs is lengthened by less than 0.5 fs after propagating through a 55 μm crystal. The higher order spectral phase is not considered in the simulation.

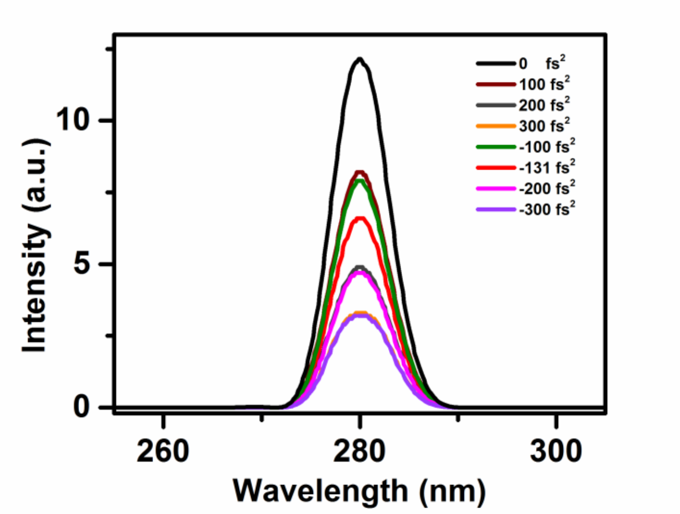

Figure 2.10: Simulated spectra under various quadratic phase.

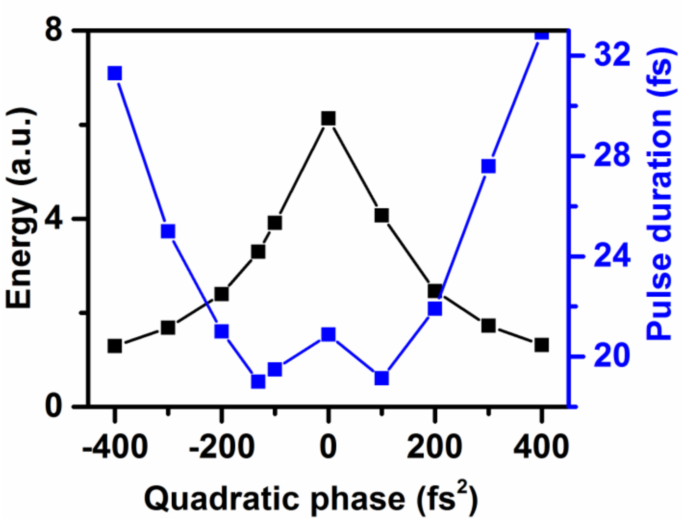

Figure 2.11: Simulated output energies and pulse durations under various quadratic phase.

The simulated spectra in Figure 2.10 show no spectral tuning by changing the quadratic spectral phase which means the peak wavelength of the generated pulse is independent of the quadratic phase. With increasing of quadratic phase, the output intensity decreases because the peak intensity of the fundamental pulse is reduced. If the fundamental pulses are stretched with the same amount of quadratic phase but with opposite sign, the resulting generated spectrum doesn't show any major change, because in the thin crystal, the direction of the chirp doesn't play a substantial role. When a BBO crystal with doubled thickness (110 μm) is used, the difference of spectral intensities between pulses with opposite phases will be increased by a factor of 5. A more quantitative description of the generated SH pulses under various quadratic phase is shown in Figure 2.11. The output energy curve shows a symmetric dependence on the applied phase. In the case of transform-limited pulses (τ=15.4 fs), the generated SH pulses have the maximum energy output. However, the exact phase cancellation doesn't result in the shortest SH pulses. Instead, a negative phase (-131 fs^2) very near zero compensation gives the minimum pulse duration of 19 fs. The group velocity mismatch becomes more severe with shorter fundamental pulses, which can explain the longer SH pulses at 0 phase. The improvement of pulse duration at -131 fs^2 is due to the internal group velocity dispersion of the SH pulse.[61] The internal group velocity dispersion of the generated pulses rearranges the phases of different frequency components in an opposite direction compared to the GVM. Of course, the obtained minimum SH pulse is still not transform-limited, especially when a thick crystal is used, an extra phase compensator may still be needed after the SH process. In conclusion, the SH pulse duration is determined by the combined effects of GVM in the nonlinear crystal and the phase added to the fundamental pulses.

2.3.3 Experimental realization and characterization

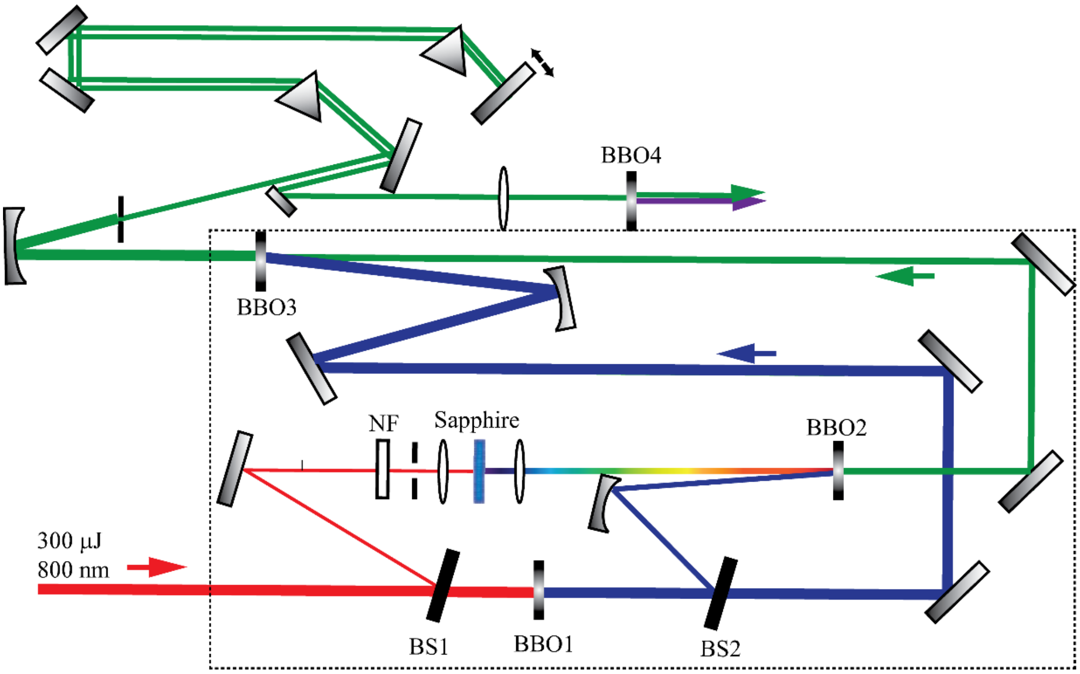

Figure 2.12: Experimental setup for the UV SHG NOPA using pre-compensation of the fundamental pulses. 300 µJ pulses from Ti:sapphire CPA is used to pump the two-stage visible NOPA (marked with dashed line). An iris is placed after the collimation of the visible pulses, which is used as a spatial filter to attenuate the fundamental energy of the SHG and also to keep a good beam profile of the generated UV light. The output pulses of the two-stage NOPA are over-compressed by a double-pass pair of fused silica prisms to be negatively chirped with a pulse duration of about 30 fs. Subsequently, the negatively chirped pulses are focused into a 55 µm BBO crystal (θ=45°) for collinear frequency doubling using type I phase matching. Since the output UV pulses and the fundamental visible pulses are spatially overlapped as they exit from the BBO crystal, four dielectric mirrors (HR 262-266 nm) are used to filter out the residual visible pulses. BS1: 5 % reflection beam splitter, BBO1: 0.5 mm thickness, cutting angle of 29.2°, NF: neutral density filter, BBO2: 1 mm thickness, cutting angle 32.5°, BBO3: 2 mm thickness, cutting angle of 32.5°, BBO4: 55 µm thickness, cutting angle of 45°.

Our experimental setup for the SH UV generation is shown in Figure 2.12, which is based on the scheme performing pre-compensation in the fundamental pulses, as showed in Figure 2.9 (b). The fundamental visible pulses generation is identical to that used for SFG-based UV pulse generation (see last section). The typical bandwidth of amplified visible pulses can potentially support sub-20 fs pulse duration in most of the tuning range (Figure 2-13 (a)). The output energy of the visible pulses is up to 15 μJ. After the second stage of nonlinear amplification, the spectral phase of the visible pulses is controlled by a pair of fused silica prisms. The apex angle of the prism is cut such that the angle of incidence is the Brewster angle at the central wavelength. The tip-to-tip spacing of prisms is adjusted from 70 to 90 cm depending on the spectral range of the visible light. Afterwards the visible pulses are focused into a 55 μm type I BBO crystal (θ=45°) for frequency doubling, which is a compromise between attainable energy and the duration of the generated pulses. Our system is optimized for the shortest pulse duration, which as demonstrated in the simulation, the value of spectral phase giving the shortest pulse duration is very close to the value giving the highest conversion efficiency. The UV beam is collimated with a spherical mirror with 10 cm focal length. The residual visible light is removed from the output beam using four dielectric mirrors, which are high reflective at 266 nm and transmissive in the visible. Although the reflection of each dielectric mirror gives rise to about 5-10 % energy loss, UV pulses up to 500 nJ are obtained. Visually no significant fluctuation is observed. The output stability can be kept under 3 % for hours during our transient absorption measurements. The conversion efficiency is about 8 % when the BBO is positioned a half centimeter before the focus. The tunable range of the UV output is dependent on the tunability of the visible NOPA. Using visible pulses in the range of 480 nm to 660 nm, the output UV is tunable from 250 to 330 nm.

Employing fine adjustment of the BBO crystal and tuning of the prism compressor, we can obtain UV pulses with more than 6 nm bandwidth in the whole tuning range (Figure 2.13 (b)), which potentially supports a pulse duration of sub-30 fs. The observed pulse durations are summarized along with the corresponding spectra in Figure 2.14, which are not optimized to be the broadest. The time-bandwidth product varies from 0.47 to 0.58. Compared to the simulation, a slight broadening of the UV pulses is observed, which could come from the higher-order chirp and further dispersion in the MgF_2 window of the photomultiplier tube. These effects cannot be compensated by a prism compressor alone. The unavoidable spectral distortion in the SH pulses can be partially removed by applying an extra chirped mirror.

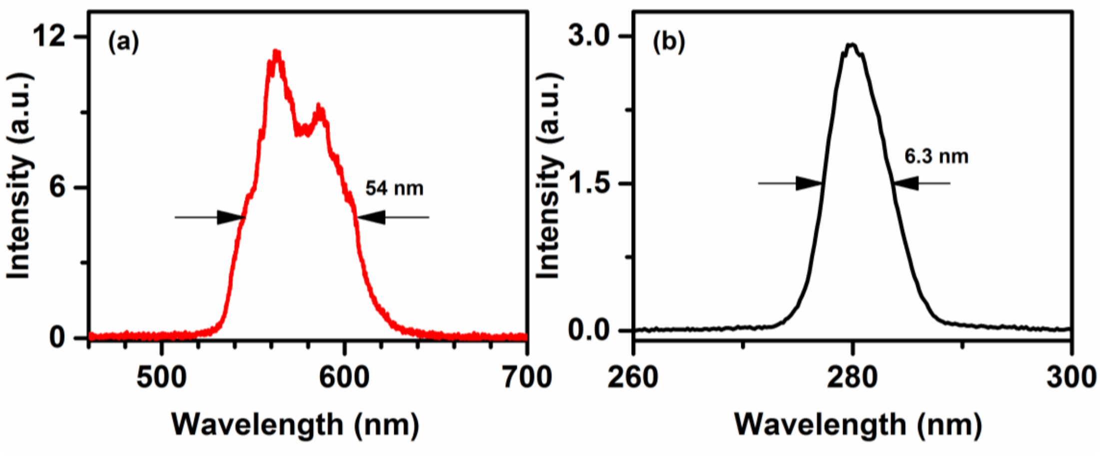

Figure 2.13: (a) Spectrum of the visible fundamental pulses obtained from a two-stage NOPA, (b) spectrum of the UV output generated by SHG.

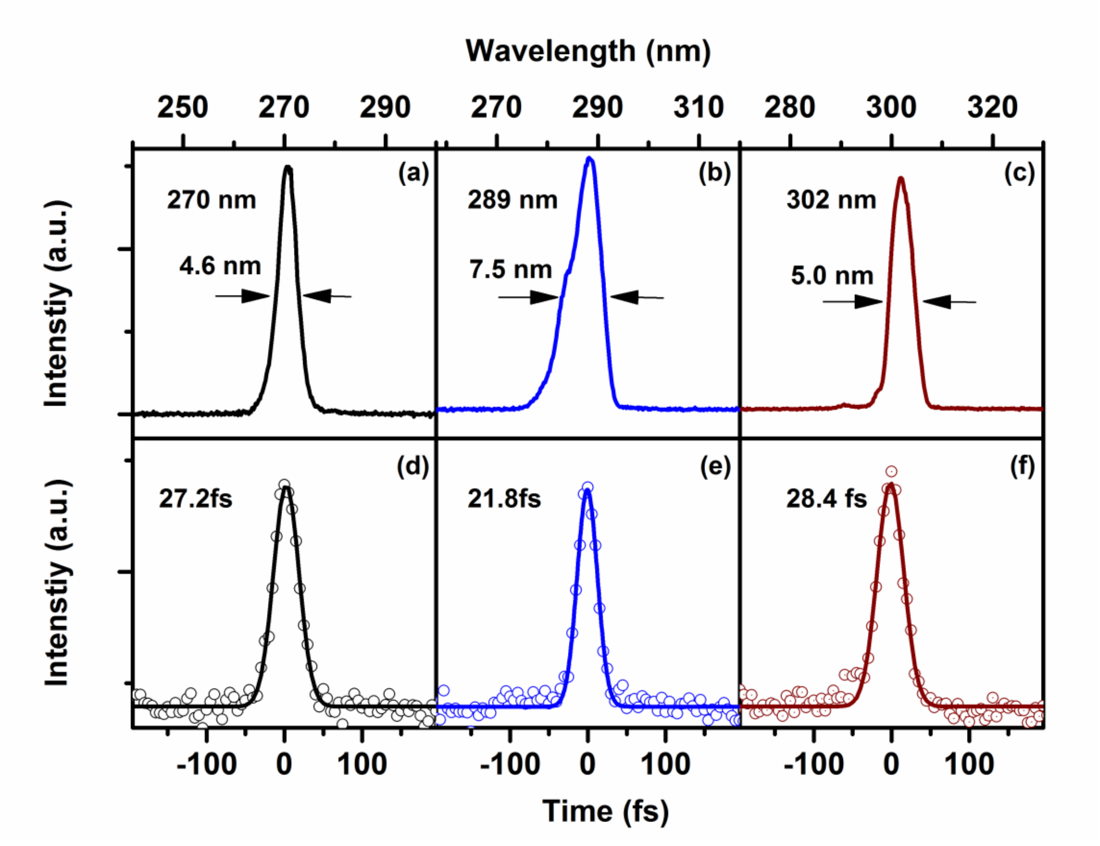

Figure 2.14: Spectral (a-c) and temporal (d-f) characterization of SHG UV output pulses. For pulses at 270 nm, (a) the spectral bandwidth is 4.6 nm and (d) pulse duration is 27.2 fs, corresponding to the time-bandwidth product $\Delta\nu\Delta\tau$ of 0.52. For pulses at 289 nm, (b) the spectral bandwidth is 7.5 nm and (e) pulse duration is 21.8 fs, $\Delta\nu\Delta\tau$= 0.58. For pulses at 302 nm, (c) the spectral bandwidth is 5.0 nm and (f) pulse duration is 28.4 fs, $\Delta\nu\Delta\tau$= 0.47.

2.4 Conclusion and outlook

Nonlinear frequency up-conversion processes via SFG and SHG have been presented. The essential aspects for the generation of ultrashort UV pulses were identified and analyzed both theoretically and experimentally. In terms of energy conversion efficiency, pulse duration and ease of implementation, the best performance of UV generation based on SFG is obtained by mixing uncompressed visible pulses with stretched NIR pulses. Conversely, for SHG the best results were obtained when the fundamental pulses were compressed and deliberately left slightly negatively chirped. The experimental results of both UV generation schemes are summarized in the following table.

Table 2.1 Experimental results of the generation of UV pulses

	SFG	**SHG**
Supplied energy	400 nJ	300 nJ
Output energy	2 μJ	< 1 μJ
Tunable range	300- 350 nm	250- 330 nm
Pulse duration	Sub-30 fs	Sub-30 fs
Band width	> 6 nm	4.5- 7.5 nm
Compression	After UV generation, about 50 % energy is lost during the compression	Prior to UV generation, about 20 % energy loss during the compression of the fundamental visible pulses
Comments	The time zero has to be regained after any alteration of the optical system	Easy to adjust and keep stable

Independent of the frequency conversion process, the duration of the UV pulses is mainly limited by the bandwidth, particularly at shorter UV wavelengths. The bandwidth is determined by the acceptance bandwidth of the nonlinear crystal and GVM. The GVM effect is more severe towards shorter UV wavelengths. Thus, it seems realistic that the UV pulses generated in SHG have less bandwidth than in SFG. However, if both schemes generate the UV pulse at the same wavelength, for example at 300 nm, the SHG gives more bandwidth than the SFG as in the BBO crystal, the SHG acceptance bandwidth is 20 % more than the SFG.

By current SFG and SHG schemes, the generated UV pulses are very close to the transform limit which is supported by the bandwidth shown in Table 2.1. In order to generate UV pulses with shorter duration, the limitation of the bandwidth has to be overcome. One proposed method is to arrange the frequency components of each input pulse into an appropriate order to form frequency pairs that satisfy the same phase matching condition. A simple way of doing this is to substantially chirp the two input pulses with opposite sign, by tuning the delay between them different frequency components of the input pulses can be arranged into pairs to meet the same phase-matching requirement. In the case of ordinary frequency conversion, if the phase matching condition is satisfied for the central frequencies $\omega_3^c n_3^c = \omega_1^c n_1^c + \omega_2^c n_2^c$ then it will not be satisfied for most pairs at other frequencies resulting a restricted bandwidth (Figure 2.15 (a)). However, in the chirp-assisted scheme, the phase matching requirement is met not only by the central frequency pair, but also other pairs which generate off-center sum frequencies resulting a wider bandwidth or more-efficient conversion (Figure 2.15 (b)). This chirp-assisted frequency conversion will be applied to SFG and SHG UV generation and shorter pulses sub-20 fs are expected.

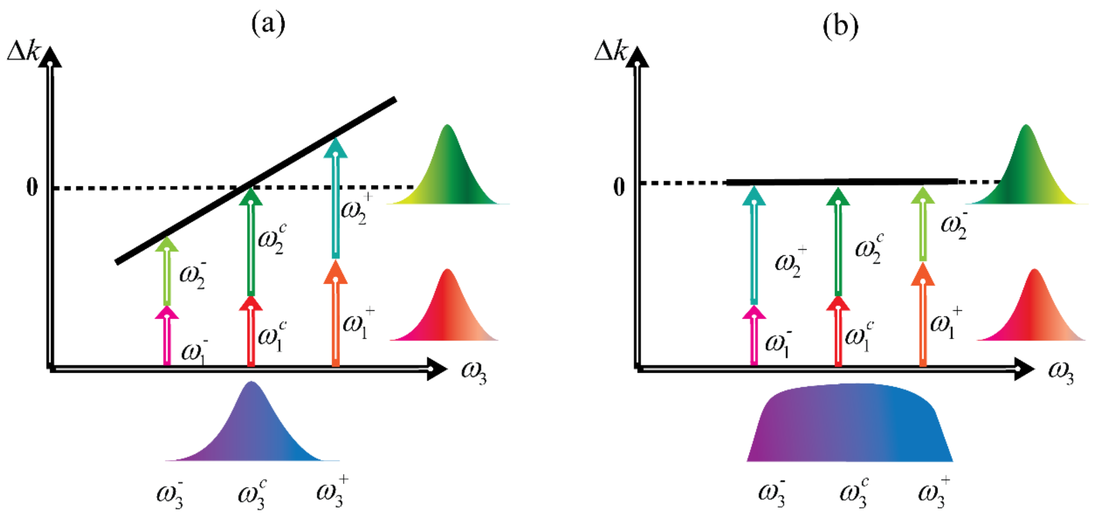

Figure 2.15: (a) Ordinary frequency conversion. The phase matching requirement is satisfied for the central frequencies pair $\omega_3^c n_3^c = \omega_1^c n_1^c + \omega_2^c n_2^c$. (b) Chirped-assisted frequency conversion. The phase matching is achieved for a broad bandwidth of generating waves.

Chapter 3

Characterization of UV Pulses by Two Photon Absorption

In this chapter, the ultrashort pulses are characterized by a very compact and simplified autocorrelator device based on two photon absorption (TPA) in a photomultiplier tube (PMT). An online-read configuration for acquisition and evaluation of the data is introduced, which makes full use of the collected data and allows a visual control of relevant measurement parameters. In order to confirm the reliability of the pulse duration measured from autocorrelation experiments, an experimental verification is conducted for various pulses fluences. The reliability and suitability of TPA autocorrelation are discussed by investigating different window materials and photocathodes of the PMT.

3.1 UV pulses characterization

A direct and unambiguous characterization of femtosecond pulses in the UV spectral range is much more demanding than in the visible. The routine method of phase matched second-harmonic (intensity) autocorrelation[66-68] in nonlinear crystals cannot be applied in the UV range due to the lack of nonlinear crystals with phase matching and optical transmittance.[69, 70] Other alternatives like cross correlation through sum frequency or different frequency mixing[71] can partially overcome these limitations. However, the characterization is restricted to the spectral range over 300 nm and requires an additional auxiliary pulse with comparable pulse duration, which complicates the adjustment of the optical system. Moreover, a relative large group velocity walk-off between the UV and visible pulses tends to broaden the correlation curve and therefore induces errors in the determination of the pulse duration.

Picosecond and femtosecond autocorrelation measurements of UV pulses based on TPA induced photoconductivity have been performed in solid materials[72-81], gases[82-84], and even solutions[85]. The TPA involved characterization is insensitive to the phase matching condition as well as the polarization and therefore can be applied to the pulses with a broad spectral band. For solid-state materials, because of the wide band gap, diamond (5.45 eV),[72] BBO (6.6 eV),[86] fused silica (9 eV),[79, 87] and MgF_2 (11 eV)[79] can be potential candidates for the TPA process (Figure 3.1). In a typical pulse characterization based on TPA, two replicas of UV beam are temporally and spatially overlapped on the medium, and either the optical depletion signal or the induced electric charge signal is recorded by the photodiode and integrated in an amplifier. A simplified setup is designed by using the PMT photocathode as the active medium as well as the detection device,[73, 88] which are taking advantages of the photoelectric property of photocathodes. Each two-photon transition produces a photoelectron within the photocathode, which can be directly measured by the internal electrical detection. However, the pulse duration signal is often superimposed with a significant linear background signal from one-photon absorption and the thermal emission at the photocathode.[73]

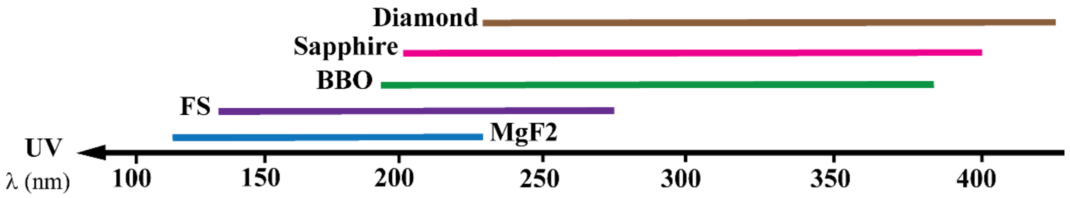

Figure 3.1: The detection ranges of TPA autocorrelation based on various solid-state materials.

In order to obtain the autocorrelation signal without background, the self-diffraction and degenerate four wave mixing based on the third order nonlinear effect in glass can be used to extract the pulse duration information.[89, 90] However, the use of these approaches has not become widespread in the UV range, because the significant nonlinear processes take place within the high-intensity of the focused beam. In the generation of UV pulses, it is difficult to reach the output energy up to micro joules or higher, so these high-energy required autocorrelations are not suitable for the characterization of low energy UV pulses.

Several methods have been developed in recent years, which are not only able to monitor the pulse duration, but also reconstruct the phase from a measured autocorrelation and the pulse spectrum. Techniques as multiphoton intrapulse interference phase scan (MIIPS)[91] and dispersion scan (d-scan)[92, 93] have been reported, which consist in applying spectral phases to the pulse to be characterized and measuring the resulting second harmonic signal. However, the transfer of both methods to the UV range are intricate because a nonlinear crystal is still needed to get the respective spectrogram or a sonogram to retrieve the phase information of the pulses. Multiple frequency-resolved optical grating (FROG) techniques have been successfully transferred to the UV spectral region. Capable UV characterizations of FROG setups are often relying on third-order nonlinearities. Therefore, they again require frequently high intensity, like in the case of transient grating (TG)[94], self-diffraction (SD)[28, 50] and polarization gating (PG)[95, 96]. Besides to the requirement of high intensity, the complex implementation of setups and mathematical retrieval procedures add cumbersome works in the spectroscopic applications. Additionally, the UV pulses are usually generated through several nonlinear optical processes combined in series, the incidental instability and the beam profile with multi-modes will influence the accuracy of the measured pulse duration.

For a straightforward and easy-to-handle characterization of UV pulses in our application of transient absorption spectroscopy, a simple on-site measurement of the pulse duration is performed based on a solar blind PMT. A significant advantage of incorporating a PMT into the autocorrelation measurements is that the desired two-photon response, the transformation of light into electric voltage and voltage amplification are all combined into one single compact device. Another advantage distinguishing our setup from other TPA autocorrelators is its construction which is based on a simple split mirror design without using any beam splitter which induces extra dispersion in one beam. The reduced degrees of freedom render this TPA autocorrelator well suited to obtain everyday pulse validation in the spectroscopic applications.

3.2 Characterization of PMT

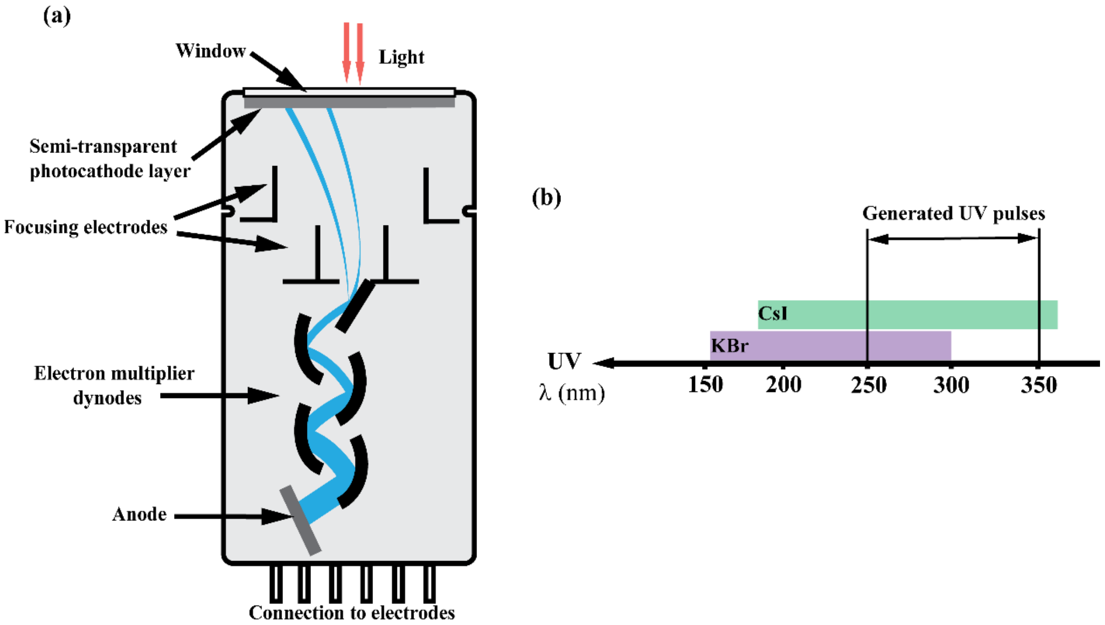

Figure 3.2: (a) Illustration of the PMT. The photocathode is sealed in a vacuum shield tube with the electron multiplier. The PMT operates in a semi-transparent configuration in which a thin film of photocathode is coated over a UV transparent window. The input UV pulses are incident on the photocathode film after transmission through the MgF_2 window. The TPA induced free electrons are focused and amplified by multi-stage of dynodes. (b) The bandgaps of KBr and CsI cathode allow for the observation of TPA signal for pulses in the wavelength range of approximately 151-302 nm and 179-358 nm, respectively.

The PMT is an extremely sensitive light detector providing a current output proportional to the incident light intensity. When the incident photon strikes onto the photocathode, and its energy $h\nu$ is more than the work function W of the photocathode material, then an electron is ejected. If the incident photon satisfies another condition as $h\nu<W<2h\nu$, under high incident intensity, the photocathode will absorb two photons simultaneously and eject one electron. The intensity of the photoemission has a nonlinear quadratic dependence on the incident intensity. After ejection from the photocathode, electrons are electrostatically accelerated and focused on the first dynode of the electron multiplier, and further focused and amplified onto the next dynodes repeatedly (Figure 3.2 (a)). The amplification of each dynode depends on the energy of the incident electrons and the inter-electrode voltage provided by a high-voltage power supply.

According to the application, the PMT can be designed and manufactured with various photocathode materials. Each type of photocathode has a characteristic spectral response. The performance of the entire photon-detecting device is determined by the conversion efficiency from photons into electrons, which is radiation wavelength dependent and can be described as the spectral response. As mentioned in the chapter of UV pulse generation, the total spectral range of the generated UV pulses from SFG and SHG NOPA is spanning from 250 nm to 350 nm, thus photocathodes with high linear response efficiency in the range of 125-175 nm are required. Two commercial PMT (Electron Tubes 9423B/9424B) manufactured with different cathode materials, KBr and CsI, are applied to characterize pulses at the wavelength region of 250-300 nm and 300-350 nm, respectively. The spectral response curves of two solar blind photocathodes are shown in Figure 3.3. Multiplying the wavelength of the spectral response curve by the factor of 2 gives the corresponding TPA response curve. Both photocathodes are visible blind and only sensitive to vacuum-UV and UV light. Both photocathodes show a maximum spectral response at 120 nm. The overall quantum yield of CsI is higher than KBr, but KBr is more sensitive to the shorter wavelength and pushes the linear optical response to 160 nm. Therefore, KBr is expected to give higher signal-to-background ratio by supressing linear response at wavelengths below 300 nm. The responses at long wavelength for CsI and KBr cut off at 230 nm and 160 nm, respectively, which is determined by the work function of the photocathode. The work function of CsI is about 6.9 eV[97], and about 8.2 eV for KBr[98]. Due to the transmission limit of the window material, the spectral responses at short wavelength cut off at 110 nm for both photocathodes. The window material of the two PMT is 2.5 mm thick MgF_2, which allows the transmission of UV light down to 115 nm and is free from radioactive contaminants in the wavelength range of pulses to be characterized. The transmission curve of MgF_2 window is shown in Figure 3.4. For a particular photocathode to be suitable for TPA autocorrelation, it should possess a quadratic nonlinear response to the incident optical radiation. The response of CsI photocathode has shown a quadratic behaviour with a slop of 1.93 in the double logarithmic plot against the input optical energy.[78]

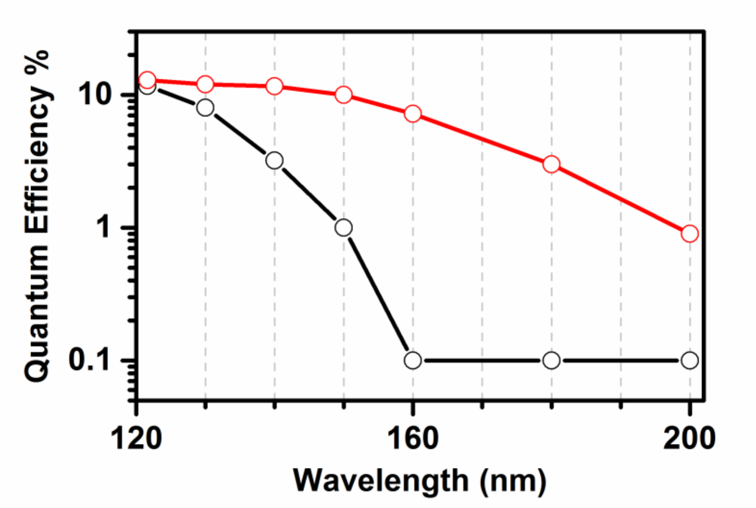

Figure 3.3: Spectral response curves of CsI (red) and KBr (black). The data are provided by ET Enterprises.

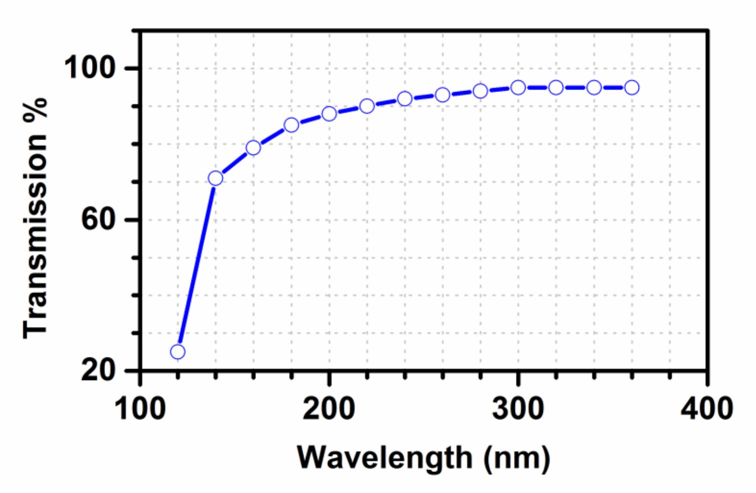

Figure 3.4: UV transmission curve for MgF_2 window used in the PMT. The data are provided by ET Enterprises.

3.3 Autocorrelation setup

The layout of the TPA autocorrelator is shown in Figure 3.5. In this setup, instead of using conventional beam splitters, the replica beams are realized by spatial cutting the beam profile in two D-shape aluminum mirrors. The gap between the mirrors is set as small as 300 μm that allows the separation of two replicas and leads to minimal energy loss in the gap. One of the D-shape mirrors is mounted on the piezo-stage translator to realize a time scan up to 3.3 ps. The two replicas are focused on the photocathode of the PMT by an Aluminum focus mirror (150 mm focal length). The photoelectrons generated from TPA in the photocathode give the information of the pulse duration in the form of an autocorrelation trace as a function of the temporal delay between the two replicas. The TPA efficiency can be improved by focusing more efficiently into the photocathode. Since the response of TPA increases quadratically with inverse spot area. Without the consideration of self-focusing effect, the smallest obtainable spot size of the incident UV light is estimated about 11 μm at the photocathode by enlarging the beam size before focusing and using 150 mm spherical mirror. However, the spot size might be larger than the estimated size, because of the strong aberration of the UV beam.[99] The input energy is varied by using a set of neutral-density filters as reflective attenuators. The autocorrelator is designed to be very compact in order to minimize the variation of the optical path when changing the filter.

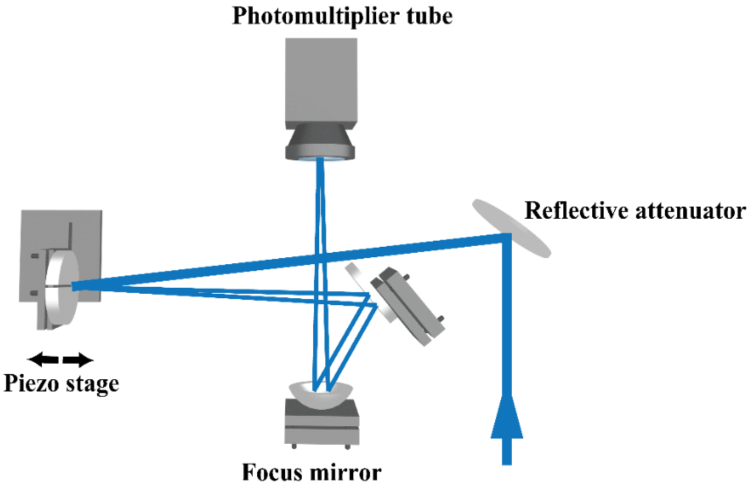

Figure 3.5: Layout of the autocorrelation setup. The input UV pulses are attenuated by the reflective neutral density filter. The two replicas are reflected off the D-shape-mirror pair. One of the D-shape mirrors is mounted on a two-dimension adjustable mirror mounting and the other one is fixed on a piezo stage. The two replicas are focused and overlapped in the PMT by using an aluminum coated focusing mirror (150 mm focal length).

3.4 Data acquisition

For the data acquisition, evaluation and real-time display, a PXI system (National Instrument) with a Labview software is used. The output voltage of the PMT is amplified by a factor of 20 with a voltage amplifier and integrated with an external gated Boxcar-integrator. The piezo stage (PI P-625.1CD) is operated in an open loop configuration, and the whole travel range is 500 μm corresponding to a maximum temporal delay about 3 ps.

In the beginning stage of our experiment, the piezo stage was driven by the voltage generator with a triangle waveform. The voltage range and frequency were set to be 6 V and 2 Hz depending on the temporal length of the pulses to be measured. The output voltage of PMT was read as an Analog Input in the virtual instrument (VI) which was triggered and sampled with 1 kHz rate from the laser repetition rate. The voltage was converted into time delay using a pre-recorded voltage-time calibration function. For the evaluation of autocorrelation traces, as shown in Figure 3.6, only data obtained from the high or low ramp of the drive voltage were selected and displayed with a Gaussian fitting curve, which has been introduced previously in the SHG autocorrelation.[100] However, applying this rapid scanning configuration to the TPA autocorrelation makes the extraction of the pulse duration information difficult because of the strong background signal and relatively noisy UV pulses. The data acquisition proceeds independently of the drive-voltage generation. For example, in order to read one valid data set with 200 samples as shown in Figure 3.6, more than one period of drive voltage is needed and 75 % acquired data cannot be used because they are either in the low ramp or between the low and high ramp in each sampled range. It is possible to obtain more valid data by reducing the number of samples to read, however, it will compromise the resolution of the autocorrelation trace (Figure 3.7 (a)) and lead to a wrong interpretation of the autocorrelation curve. This problem is particularly severe for the TPA signal with low contrast ratio of the peak and background.

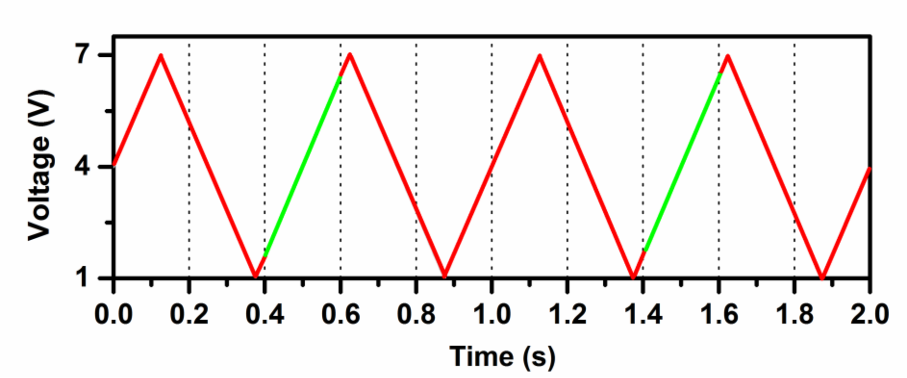

Figure 3.6: The piezo stage is driven by the generated voltage with 2 Hz triangle waveform. Read 200 samples per channel with 1 kHz laser repetition rate, giving a reading cycle of 0.2 s. Only data obtained from the high or low ramp of the drive voltage are selected. In the high ramp mode, the data marked with green are selected, and red marked data are invalid.

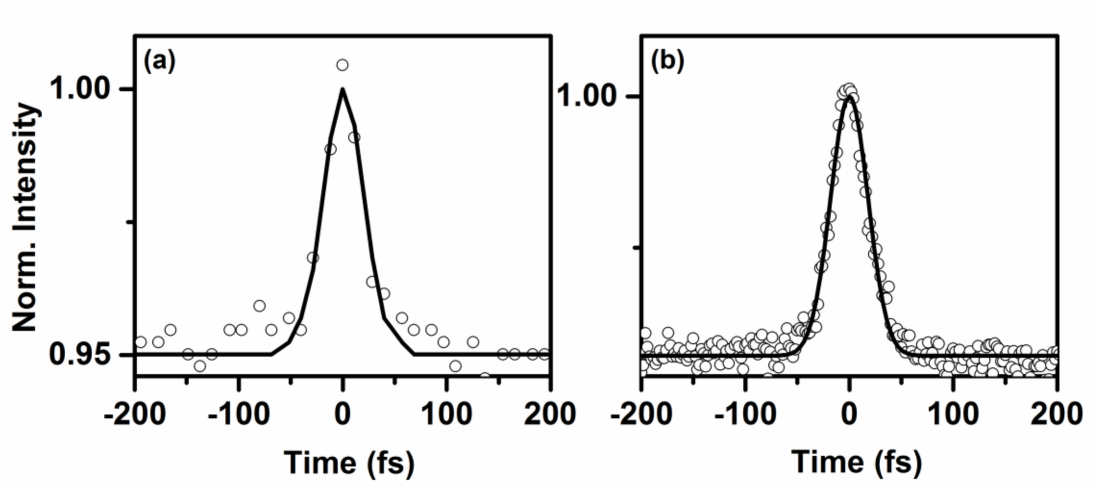

Figure 3.7: Autocorrelation trace at 280 nm acquired and evaluated by (a) rapid scanning configuration giving a pulse duration of 34 fs, and (b) online-read configuration giving a pulse duration of 28 fs. The open dots are experimental data, and black lines are fits.

In order to improve the performance of data evaluation, a modified configuration is applied in the TPA autocorrelation, in which the drive-voltage generation and the data acquisition proceed in synchronization. Depending on the duration of the pulses to be measured, the autocorrelation VI (shown in Figure 3.8) creates an Analog Output signal to drive the piezo stage with a chosen scan range and time resolution. The time resolution is only limited by the positioning resolution of the piezo stage, which is under 1 nm in the case of our setup corresponding to a time resolution of less than 0.01 fs. The output voltage of PMT is read as an Analog Input Signal from the same VI. Both data acquisition and voltage generation proceed in parallel with 1 kHz rate. One data point is read after one-step movement of the piezo stage. Each data point corresponds to a single laser shot. When the whole scan range is complete, the signal data points are displayed and the pulse duration is calculated from the Gaussian fitting parameters. Compared to the rapid scanning, the advantages of this online-read configuration can be summarized as: (1) all data acquired can be used for evaluation, thus less time is needed to obtain an entire autocorrelation profile; (2) a sufficient number of data points can be obtained; (3) full visual control of all measurement parameters, such as the scan range and resolution. The autocorrelation trace based on this configuration is shown in Figure 3.7 (b).

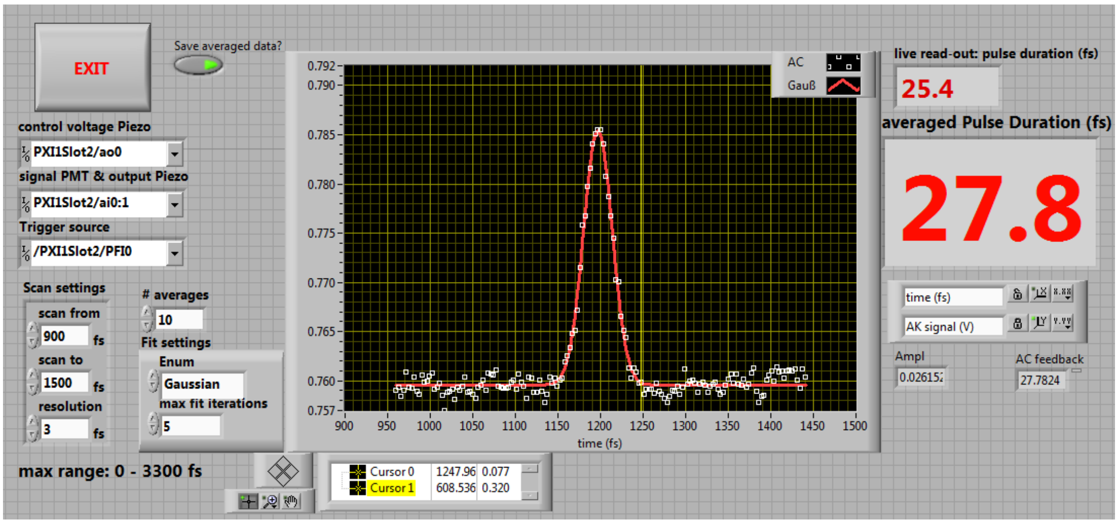

control voltage Piezo: PXI1Slot2/ao0
signal PMT & output Piezo: PXI1Slot2/ai0:1
Trigger source: /PXI1Slot2/PFI0

Scan settings
scan from: 900 fs
scan to: 1500 fs
resolution: 3 fs

averages: 10

Fit settings
Enum: Gaussian
max fit iterations: 5

max range: 0 - 3300 fs

Cursor 0	1247.96	0.077
Cursor 1	608.536	0.320

live read-out: pulse duration (fs): 25.4
averaged Pulse Duration (fs): 27.8

time (fs)
AK signal (V)

Ampl: 0.026152
AC feedback: 27.7824

Figure 3.8: Screenshot of the autocorrelation VI. The scan range and resolution can be chosen according to the pulse to be measured. If the pulses are noisy, an averaging mode can be applied.

3.5 Experimental results and discussion

A precise and reliable measurement of pulse duration plays an important role in time-resolved spectroscopy applications. Several factors could influence the fidelity of the autocorrelation trace obtained by TPA in the PMT, such as the intensity and spectral range of the input pulses, the intrinsic response time of the photocathode, as well as the window material which could lead to distorted pulse duration measurement. Moreover, to extract reliable information of the pulse duration, it is important to reduce the background signal and increase the signal-to-noise ratio which is dependent on a combination of the spectral response of photocathode and the spectral range of input pulses. In the following, a detailed investigation about the reliability of measurements and evaluation of the data will be carried out in the aspects of pulse energy influence, material dispersion effect and photocathode effect.

3.5.1 Pulse energy influence

A theoretical model of TPA-induced photon-detection is developed,[57] in which electron ejection takes place through the simultaneous absorption of two photons. If linear absorption and free-carrier absorption are neglected, the TPA photoelectric signal is primarily determined by the amount of energy absorbed by the photocathode, then the autocorrelation signal can be expressed as the absorption of the incident beam. The intensity change of the two replicas can be expressed as follow

$$\frac{dI_1}{dz} = -\beta I_1 I_2 - \beta I_1^2 \tag{3.1}$$

$$\frac{dI_2}{dz} = -\beta I_2 I_1 - \beta I_2^2 \tag{3.2}$$

where I_1 and I_2 are the intensities of the replicas, $I = I_1 + I_2$ is the total intensity of the incident pulses, and β is the TPA coefficient. The generated TPA signal is governed by β, which is related to the imaginary part of the third-order susceptibility $\chi^{(3)} = \chi_R^{(3)} + i\chi_{im}^{(3)}$ of the TPA medium[101]:

$$\beta = \frac{\omega \chi_{im}^{(3)}}{n_0^2 \varepsilon_0 c^2} \tag{3.3}$$

in which ω is the carrier frequency of the input pulses, n_0 is the refractive index of the TPA medium, ε_0 is the permittivity in vacuum, and c is light speed in vacuum.

For input pulses with the spatial and temporal profile described by Gaussian distribution as $I_i(r,t) = I_{i0}\exp\left[-t^2/\tau^2\right]\exp\left[-r^2/w^2\right]$, the solutions for I_1 and I_2 at distance r from laser beam axis and time t are given by[102]

$$I_1(z,r,t) = \frac{I_1^0(r,t)}{1+\beta z\cdot\left[I_1^0(r,t)+I_2^0(r,t-\Delta t)\right]} \tag{3.4}$$

$$I_2(z,r,t) = \frac{I_2^0(r,t)}{1+\beta z\cdot\left[I_1^0(r,t-\Delta t)+I_2^0(r,t)\right]}. \tag{3.5}$$

$I_i^0(r,t)$ refers to the pulse intensity at z=0. A delay time Δt between the replicas is scanned in the autocorrelation measurement. Take one beam I_1 as an example, integration of Equation (3.4) over space and time gives the transmission T_1 of the pulse for delay time Δt:

$$T_1 = \frac{1}{E_1}\int_{-\infty}^{\infty}\int_R \frac{I_1^0(r,t)}{1+\beta z\cdot\left[I_1^0(r,t)+I_2^0(r,t-\Delta t)\right]}\,dRdt \tag{3.6}$$

where E_1 is the incident energy of one beam, and R is the overlapping area of the replicas. The integrant can be expanded in a power series and perform the integral on each of the series terms. The absorption behaviour can be obtained as A_1=1-T_1. For the condition that the nonlinear absorption is small, as $\left|\beta z I_{i0}\right| \ll 1$, the A_1 is approximated as [102]

$$A_1(\Delta t) = \frac{\beta z}{2\sqrt{2}} I_{10} + \frac{\beta z}{2\sqrt{2}} I_{20}\cdot\exp\left(-\frac{\Delta t^2}{2\tau^2}\right). \tag{3.7}$$

The first term of Equation (3.7) shows the self-induced TPA which is the main contribution of the background signal, and the second term corresponds to the autocorrelation of the two pulses which gives the pulse duration information. For Gaussian pulses, the temporal width of the autocorrelation trace is broadened by a factor of $\sqrt{2}$ compared to the pulse duration of the input beam. In case of our experiment $I_{10} = I_{20} = I_0/2$, the autocorrelation signal AC of the photoconductivity is expressed as

$$AC = \frac{k\beta z}{2\sqrt{2}} I_0^2 \left(1 + \exp\left(-\frac{\Delta t^2}{2\tau^2}\right)\right) \tag{3.8}$$

where k is the spectral response of the PMT. Although the solution of TPA absorption is given under the approximation of $|\beta z I_{i0}| \ll 1$, when the transmission change is smaller than 15-20 %, the error from this approximation is less than 6 %.[77, 102]

Figure 3.9 shows the TPA autocorrelation traces recorded by the CsI PMT for various incident pulse energies. The light source is taken from the SHG-UV NOPA at the wavelength of 280 nm. The spectral bandwidth of UV pulses is about 6.6 nm, corresponding to a Gaussian pulse with a Fourier limit of 17.5 fs. All measured autocorrelation traces are symmetric relative to the peak. The values of pulse duration are evaluated from the full width half maximum (FWHM) of the autocorrelation traces based on the deconvolution factor of $\sqrt{2}$ for the Gaussian pulse profile. The pulse duration is broadening with increased input pulse energy. The measured autocorrelation width is lengthened by 25 % when the input pulse energy is increased to 130 nJ (Figure 3.9 (e)). If the input pulse energy is increased over 200 nJ, a decreased autocorrelation signal is observed, which can be explained as the depleted input due to the cubic response from the MgF_2 window. With a bandgap energy (11 eV) of MgF_2, the photon energy (4.4 eV) of 280 nm pulses is high enough to induce a cubic response. A general limit for the autocorrelation based on TPA in a PMT is the strong background signal from one-photon absorption and TPA signals of the two individual pulses. The pulse energy dependence of the background offset signal shows a similar trend as the pulse duration broadening when increase the input pulse energy (Figure 3.9 (f)). Note that, in Equation (3.8) the width of autocorrelation signal is independent of the incident pulse intensity, which is different from the observation in our experiments. The increase of the deviation from the real pulse duration for large fluences is due to the saturation of signals from the PMT and the increase of the free-carrier absorption.[103] The curve of offset versus the input pulse energy can be fit as a second order polynomial function. The disagreement of our data (Figure 3.9 (f)) from the quadratic dependence is probably due to the free-carrier absorption under large optical fluences. Besides, for high energy excitation the linear absorption below the bandgap may be sufficient to generate photoelectrons.

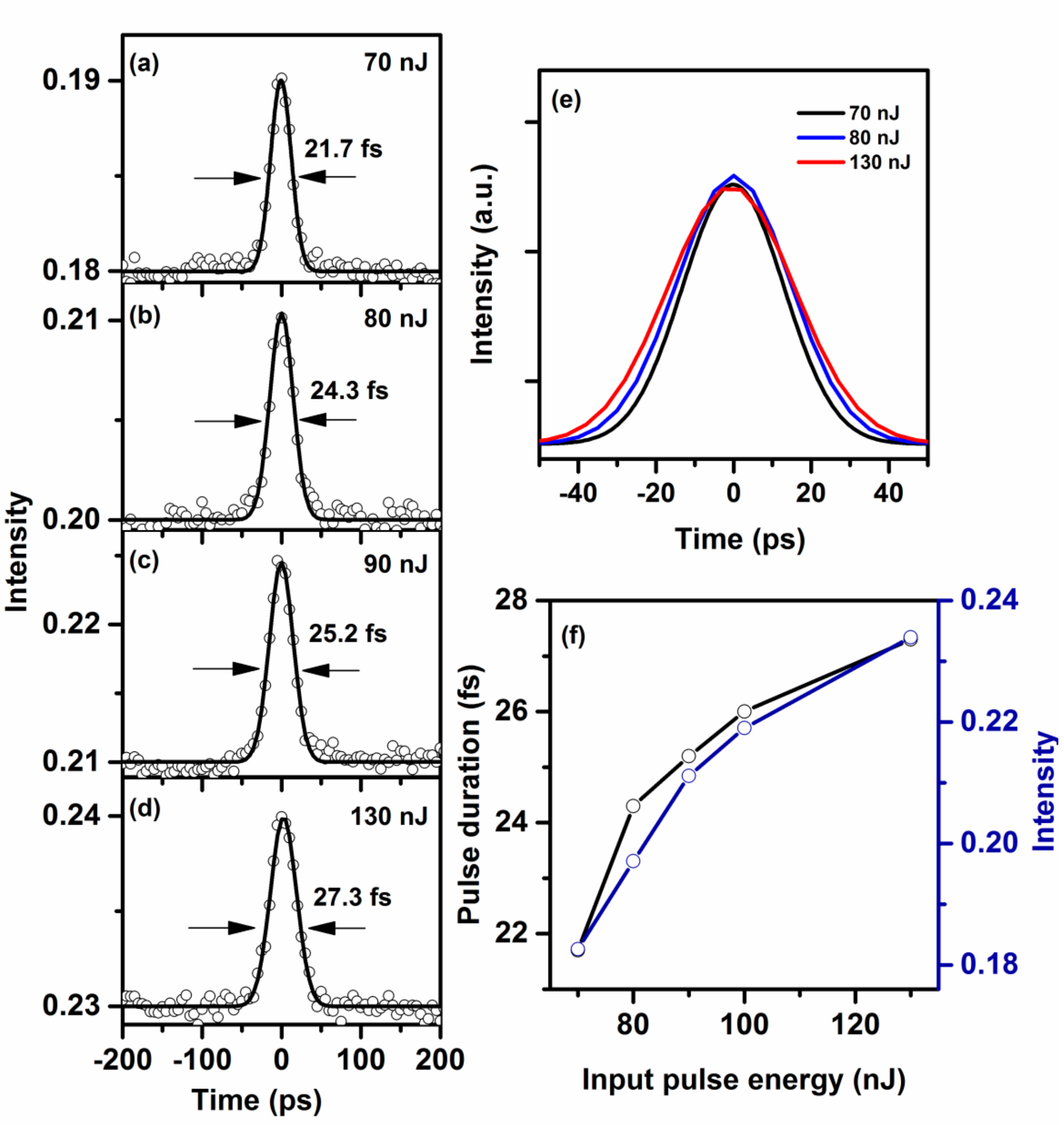

Figure 3.9: Measured autocorrelation traces at 280 nm with increasing pulse energy, the pulse widths obtained are (a) 21.7 fs, (b) 24.3 fs, (c) 25.2 fs, and (d) 27.3 fs. The open dots are measured autocorrelation data, and solid lines are Gaussian traces. (e) Selected autocorrelation Gaussian traces at different pump energies. (f) Temporal pulse broadening (black) and background offset (dark blue) versus input pulse energy.

3.5.2 Material dispersion effect

The temporal resolution of the autocorrelator is partly deteriorated by the dispersion from the thick window material of the PMT, since the PMT in our experiment is not designed to be used for the characterization of ultrashort pulses. The input surface window of the

PMT is MgF_2 with a thickness of 2.5 mm. As the laser beam passes through an optical glass, pulse lengthening is produced, which leads to a falsified pulse characterization. This problem is especially pronounced when the pulses to be characterized are in the UV part of the spectrum.

For a Gaussian pulse with the pulse duration of τ_0 and central wavelength at λ_0, after propagating a distance L in an optical glass, the stretched pulse duration can be expressed as[104]

$$\tau = \tau_0 \sqrt{1 + \left(\frac{2\,\mathrm{In}\,2L\lambda_0^3}{\pi c^2 \tau_0^2} \frac{d^2 n}{d\lambda^2} \right)^2} \tag{3.9}$$

with c being the speed of light in vacuum, and $d^2 n / d\lambda^2$ being the second derivative of the refractive index at λ_0, which can be calculated from the Sellmeier equation. For various materials, Sellmeier equation will be given in different forms. The Sellmeier equation of three common UV materials, MgF_2, CaF_2 and fused silica (FS) is

$$n^2(\lambda) = A + \frac{B_1 \lambda^2}{\lambda^2 - C_1^2} + \frac{B_2 \lambda^2}{\lambda^2 - C_2^2} + \frac{B_3 \lambda^2}{\lambda^2 - C_3^2} \tag{3.10}$$

where A, B_1, B_2, B_3, C_1, C_2, C_3 are experimentally determined constants. The values of constants for MgF_2, CaF_2 and fused silica are listed in the Table 3.1. The second derivative of the refractive index is given by

$$\begin{aligned} \frac{d^2 n}{d\lambda^2} = \frac{-1}{n^3} & \left(\frac{B_1 C_1 \lambda}{\left(\lambda^2 - C_1\right)^2} + \frac{B_2 C_2 \lambda}{\left(\lambda^2 - C_2\right)^2} + \frac{B_3 C_3 \lambda}{\left(\lambda^2 - C_3\right)^2} \right) + \\ \frac{1}{n} & \left(\frac{3B_1 C_1 \lambda^2 + B_1 C_1^2}{\left(\lambda^2 - C_1\right)^3} + \frac{3B_2 C_2 \lambda^2 + B_2 C_2^2}{\left(\lambda^2 - C_2\right)^3} + \frac{3B_3 C_3 \lambda^2 + B_3 C_3^2}{\left(\lambda^2 - C_3\right)^3} \right). \end{aligned} \tag{3.11}$$

Table 3.1 Sellmeier constants

	A	B_1	B_2	B_3	C_1	C_2	C_3
MgF_2	1.27620	0.60967	0.00800	2.14973	0.08636	18.80	25.00
CaF_2	1.33973	0.69913	0.11994	4.35181	0.09374	21.18	38.46
FS	1.00	0.696166	0.407943	0.897479	0.068404	0.116241	9.89616

The calculated results of the second order derivative of refractive index with respect to the wavelength are shown in Figure 3.10, from which it is observed that the refractive index vary strongly in the spectral range below 300 nm. When working in the spectral domain of UV, MgF_2 is the material with the lowest dispersion, compared to the other two common UV materials. However, a Fourier-limited pulse at 280 nm with 22 fs pulse duration is lengthened to 39 fs after propagation through a 2.5 mm thick MgF_2 window. Substituting Equation (3.11) into (3.9), the temporal spreading of the pulse after propagating a distance of L can be evaluated. Conversely, the initial pulse duration also can be calculated with Equation (3.11) and (3.9) if the pulse duration after propagating through the material is known.

Due to the dispersion problems encountered with MgF_2 window, the pulse duration obtained from the raw measured autocorrelation is longer than the actual pulse duration, which will falsify the time resolution in spectroscopic applications. To overcome this problem, it has to ensure that the UV pulse reaching the sample has almost the same duration as being characterized in the PMT autocorrelator. Therefore, the flow cell used in our experiment is designed to have a similar thickness as the MgF_2 window. Care is also taken to have a comparable path length in air from the UV NOPA to the flow cell and PMT autocorrelator. In practice, the UV light is pre-compressed by the prism compressor prior to the PMT and flow cell, in order to compensate the dispersive broadening of the pulses induced by the window materials of the PMT and flow cell.

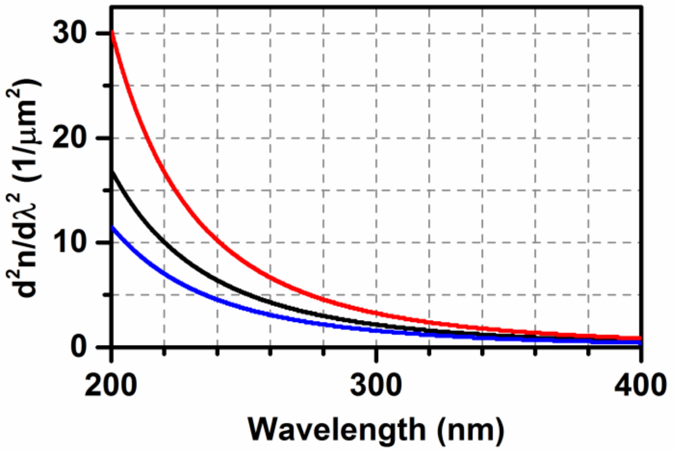

Figure 3.10: Calculated second order derivatives of the refractive index with respect to the wavelength for FS (red), CaF_2 (black) and MgF_2 (blue).

3.5.3 Photocathode effects

If the photon energy satisfies $E_{\mathrm{bg}} < h\nu < W$, where E_{bg} is the bandgap energy, one-photon absorption takes place, giving rise to the energy relaxation of the conduction electron, which increases the time resolution of the pulse characterization.[73] In general, the one-photon absorption is increasingly significant towards shorter wavelengths. Our original motivation in choice of KBr is to suppress one-photon absorption in the spectral range below 300 nm, and thus lead to a better autocorrelation performance compared to CsI. Figure 3.11 shows the autocorrelation traces measured by KBr and CsI PMT at 281 nm and 267 nm, respectively. At wavelength of 281 nm, the autocorrelation trace in KBr is shown to be more than 15 fs longer than in CsI (Figure 3.11 (a) and (b)). For a measurement of shorter wavelength at 267 nm (Figure 3.11 (c) and (d)), the durations of observed autocorrelation traces are similar in two PMT, but still KBr gives a longer pulse duration. These behaviours are contrary to what is expected. From the experimental results, CsI shows a better time resolution than KBr. The different behaviours can be explained in terms of the PMT properties: the response time and spectral response.

Cathodes for both these photomultiplier tubes contain the same under-layer. The photoemission time from both cathodes is significantly lower than timing performance of the multiplier which is the same for both types. In other words, the response time of the PMT does not depend on the type of photocathode. The response time varies approximately as $1/V^{1/2}$, and V is the voltage applied on dynodes. Therefore, the CsI photocathode has the faster response time, because of the higher voltage for a given gain than the KBr photocathode. Other factors affecting the timing are the number of dynodes and the photocathode diameter which are the same for both CsI and KBr PMT.

As mentioned in the section of 3.2, two PMT show different spectral response in the detecting UV region. The photoemission efficiency increases with a shorter wavelength. The linear spectral responses of KBr and CsI at 140 nm, corresponding to TPA at 280 nm, are 3.2 % and 11.6 %, respectively, which is about 5 times difference. For the linear response at shorter wavelength around 130 nm, corresponding to TPA at 260 nm, two PMT have similar same quantum yield of about 10 %, which gives both TPA autocorrelation traces similar duration (33 fs and 29.8 fs). These trends suggest that, the time resolution is more limited by the spectral response instead of the bandgap or work function. In our measurements, CsI is able to characterize pulses of the total spectral range from 250 nm to 350 nm. While, KBr can only give the autocorrelation trace with the duration close to the actual value on the very edge of the UV spectrum. Thus, to obtain the best time resolution for a particular photoelectric material, one must take into account the spectral response in the spectral range of interest.

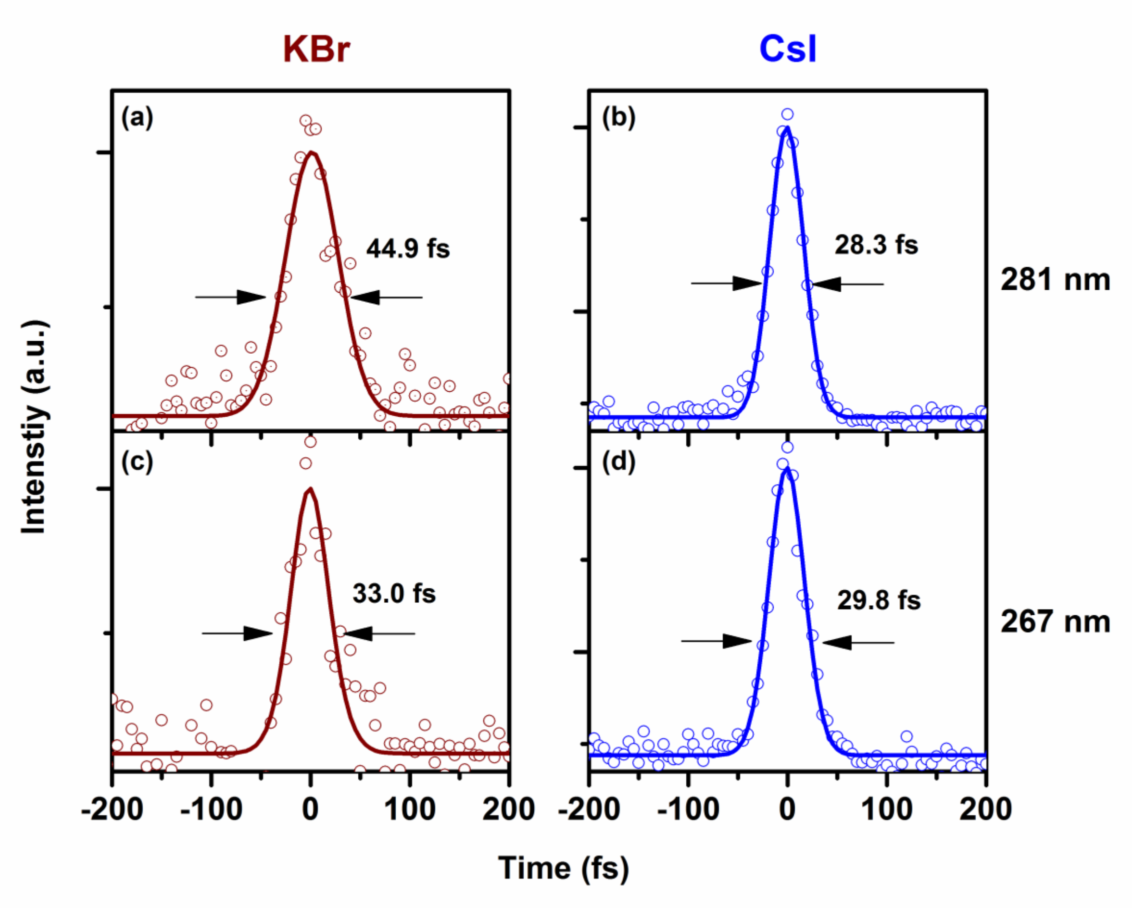

Figure 3.11: Autocorrelation traces measured by KBr ((a), (c)) and CsI ((b), (d)) photocathode. The pulse durations are (a) 44.9 fs at 281 nm, (b) 28.3 fs at 281 nm, (c) 33.0 fs at 267 nm, and (d) 29.8 fs at 267 nm.

Chapter 4

Supercontinuum Generation to the UV

A broadband supercontinuum (SC) is commonly used as the probe light in time-resolved spectroscopies. SC generation gives broadband probe light on both the Stokes and anti-Stokes flanks of the pump frequency. In this chapter, the investigation of SC focuses on the anti-Stokes side to generate a UV continuum. Spectral broadening is investigated for different pump wavelengths (800 nm and 400 nm) and intensities, and various optical media with high bandgap (CaF_2, sapphire and YAG). It is shown that the shorter pump wavelength and material with higher bandgap are more advantageous for generating shorter-wavelength SC. The spectra of each generated SC are measured in a multichannel detector. The grating-based and prism-based spectrometer are introduced and compared in terms of the spectral resolution and transmission efficiency.

4.1 UV supercontinuum generation

In 1970, Alfano and Shapiro have found that when an intense ultrashort pulse was focused into an optical transparent medium, some different frequency components appeared leading to extreme spectral broadening of the pulse,[105, 106] which is referred as supercontinuum (SC) or white light (Figure 4.1 (a)). Applications of SC have spread widely including the probe pulses in time-resolved spectroscopy[107, 108], pulse compression[109-111] and seed pulses of optical parametric amplifiers[112, 113].

The mechanism of SC generation is controversial and involves complex processes. It is generally accepted that the continuum generation is triggered by self-focusing, because the energy threshold for the continuum generation coincides with the critical energy for self-focusing.[114] Self-phase modulation is considered as the dominant mechanism leading to spectral broadening.[115] However, self-phase modulation associated with self-focusing cannot explain complicated spectral characteristics of continua completely. For example, water has been widely used to generate continuum with very broad spectrum despite the low Kerr nonlinear index.[116] Recently, it has been suggested that multiphoton ionization,[117, 118] self-steepening,[119, 120] four-wave mixing[121] and chromatic dispersion[122] play roles as well.

Under a variety of experimental conditions, many media have been found able to generate SC in the visible-to-infrared region, while much less research has been carried out in the UV spectral range. There are some reasons for the difficulties of UV SC generation. Firstly, laser pulses with high intensity are required to achieve shorter wavelength, because the spectral intensity of the continuum decreases rapidly as it diverges from the pump wavelength.[115] Secondly, most of optical materials have absorption in the UV region. For example, the photonic crystal fibers have been proved useful to push the short wavelength edge of SC down to 280 nm, while the fundamental barrier to the generation of even shorter wavelengths is the large two photon absorption in silica.[123] Moreover, it is believed that there is a bandgap threshold of the material for continuum generation, and the material with higher bandgap is more advantageous for shorter wavelength generation.[122] Nowadays only a few materials have large enough bandgaps to generate frequency components extending to UV, such as CaF_2 (10.2 eV) and LiF (11.8 eV).[118, 124] Figure 4.1 (b) summarizes several media which have been studied for continuum broadening into UV, and under the same pumping LiF produces the shortest wavelength due to having the largest bandgap.

The generation of anti-Stokes components in SC strongly depends on the pump wavelength, in other words, shorter pump wavelength can extend the anti-Stokes components more into UV (Figure 4.1 (b)). The SC generation is possible when the energy of the pump photons exceeds one third of the band gap of the medium because the self-focusing is stopped by avalanche ionization from the valence band to the conduct band.[125] Nonlinear processes like optical amplification, second harmonic generation, and sum frequency generation allow the generation of pulses deep to UV, which can be used as the pump light in the SC generation to access an even wider UV spectral range.[110] For example, the CaF_2 based continuum generation pumped by the second or third harmonic pulses of 800 nm extends the spectrum from close to the pump wavelengths down to 250 nm and 225 nm, respectively.[126] Instead of using single color pump, generated high harmonic pulses combing with the fundamental pulses via two-color filamentation lead to SC generation extending up to 230 nm in air.[127, 128] The frequency broadening around the high harmonic components, is mainly dictated by cross-phase modulation induced by the fundamental pulses.

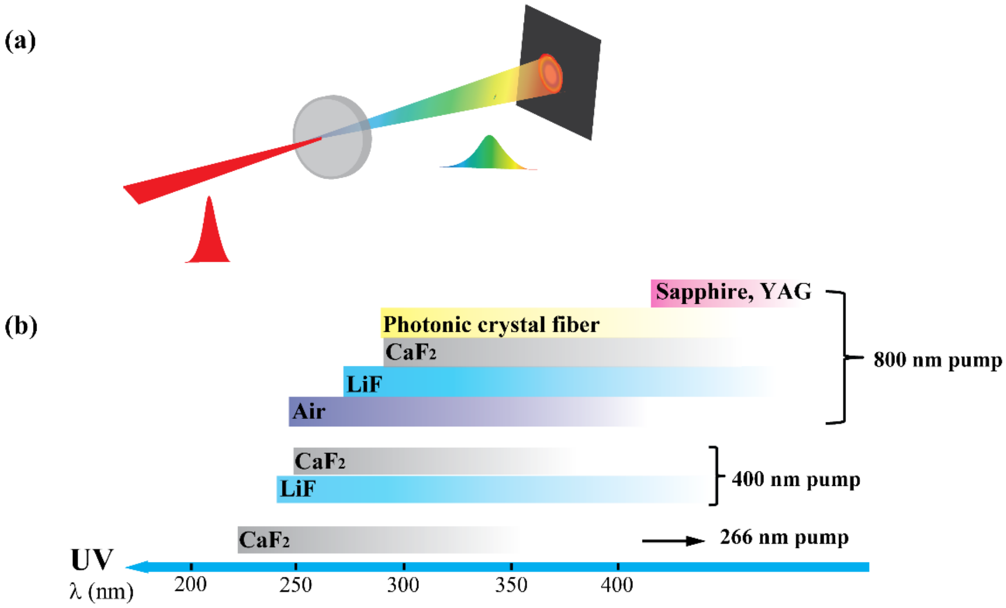

Figure 4.1: (a) The SC is generated when an intense ultrashort laser pulse is focused into a transparent medium. Because self-phase modulation and material dispersion, the generated continuum is usually temporal stretched compared to the input pump pulse. (b) The cut-off wavelength of SC generated in various media for the pump wavelengths at 800, 400 and 266 nm.[115, 120, 123, 126, 128-130]

The high pulse-to-pulse stability, high amount of coherence and low energy threshold render continuum generated from the condensed medium a valuable source of broadband radiation for spectroscopic applications.[131] As mentioned in the previous chapters, the tuning range of UV pump pulses is from 250 nm to 350 nm. In the UV spectroscopic applications, extending the probe to wavelengths as short as the pump allows the direct observation of the ground state bleach. For molecules with transition in the visible, it is also helpful to be able to monitor the ground state recovery of higher absorption bands since they do not overlap with the stimulated emission.[132]

CaF_2 and LiF tend to generate broader anti-Stokes spectrum than other materials because of the broad bandgap (Figure 4.1 (b)). However, the UV light is likely to cause color-center degradation in the ionic crystals, such as LiF.[129, 133] Therefore, of all the materials that support a broad spectrum to the UV region, only CaF_2 has been found to be useable in routine applications.[130, 132, 134] In our UV transient absorption experiment, CaF_2 is chosen as the continuum material to generate the broad probe spectrum under the pump wavelength of 800 nm and 400 nm.

4.1.1 Experimental setup

The setup for the continua generation under the fundamental 800 nm and second harmonic 400 nm pumping is shown in Figure 4.2. The laser source is a commercial 800nm Ti:sapphire regenerative amplifier system with 1 kHz repetition rate and about 100 fs pulse duration. A fraction of the amplifier output with energy about 30 μJ per pulse is selected as the input pump for the whole setup of continua generation. For 800 nm pumping, 20 % input pulses (6 μJ) is focused in a 5 mm CaF_2 substrate by a 100 mm lens. To adjust the energy, a step-variable attenuator in combination with an iris is used. The CaF_2 is polished and cut to [001] direction, so the linearly polarized laser beam propagates along the optical axis. Since CaF_2 is prone to material degradations, the crystal has to be moved continually. A motor-driven stage is designed to eccentrically move the crystal with a period of a few seconds, as shown in Figure 4.2. The pump beam is carefully aligned to be normal to the crystal surface, in order to reduce the instability induced by the continuous motion. The generated continuum is then collimated by a 1 inch off-axis parabolic mirror with a focal length of 50 mm. The 800 nm residual pump light is removed by an 800 nm edge filter. The threshold of continuum generation is lower than 3 μJ. This setup is also used for SC generation in sapphire and YAG, only by exchanging the substrate. The thickness of sapphire is 2 mm and YAG is 3 mm. Since sapphire and YAG have high damage threshold, no translation stage is needed.

For 400 nm pump, 80 % input pulses are firstly frequency doubled by a 1 mm BBO crystal with cutting angle of 29°, and then focused in CaF_2 substrate by a 100 mm fused silica lens. The maximum output energy of the second harmonic pulses is about 5 μJ. The generated continuum is collimated with an f = 50 mm off-axis parabolic mirror before passing through the 400 nm high-reflective dielectric mirror which is used to suppress the high spectral power near the pump wavelength. Since the reflection efficiency of the dielectric mirror depends on the incident angle of the beam, with a fine angle-adjustment, some more spectral range in the vicinity of the 400 nm pump can be added.

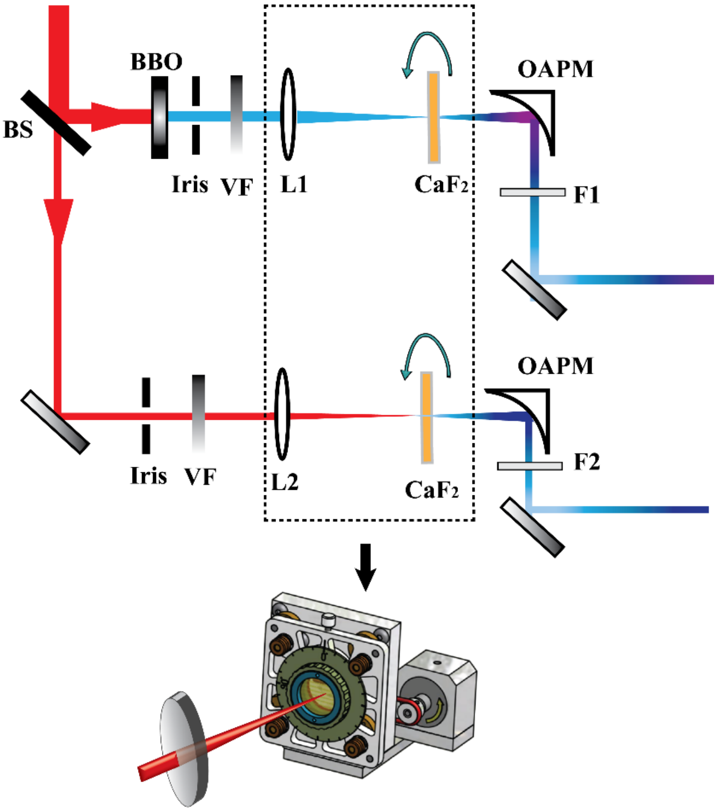

Figure 4.2: Schematic of the SC generation setup pumped by the fundamental 800 nm pulses and second harmonic 400 nm pulses. 20 % input energy is used to directly pump CaF_2 and the remaining 80 % is frequency doubled to generate SC more into UV. BS: 80 % reflection beam splitter, VF: variable filter, L1 and L2: 100 mm fused silica lens, OAPM: off-axis parabolic mirror with 50 mm focal length, F1: 800 nm edge filter (visible and UV high transmission, 800 nm high reflection), F2: 400 nm high reflection mirror.

4.1.2 Results and discussion

The spectra of generated SC in CaF_2, sapphire and YAG under 800 nm pumping are shown in Figure 4.3. The spectra of SC is measured by a prism-based spectrometer and recorded by a home-made photomultiplier array, which will be elaborated in the next section. The spectrum of SC generated in CaF_2 under 800 nm pumping spans from 300 nm to 750 nm. The dip at about 400 nm and long wavelength cut-off are due to the 800 nm edge filter used to remove the fundamental pulses. The blue wing of the spectrum is about 10000 cm^{-1} broader than sapphire, and 12000 cm^{-1} than YAG. This is not surprising, considering the dependence of spectral broadening on the medium's bandgap. One feature of the continuum is a trend of increasing anti-Stokes broadening with increasing bandgap, which has been explained by the mechanism of multiphoton excitation enhanced self-phase modulation.[118] The energy ratio of the medium's bandgap to the incident photon, $E/h\nu$, determines the amount of anti-Stokes broadening. The bandgaps of sapphire and YAG are estimated by measuring the absorption edge using UV-spectrophotometer (SHIMADZU UV-1800) and the values are 6.2 and 4.9 eV, respectively. The absorption of CaF_2 is out of the detection range (UV cut-off at 190 nm) of the spectrophotometer, but as reported early, the bandgap of CaF_2 is about 10.2 eV.[118] Thus, because of the wide bandgap, CaF_2 is chosen to further extend the SC spectrum to the deep UV under higher frequency pumping.

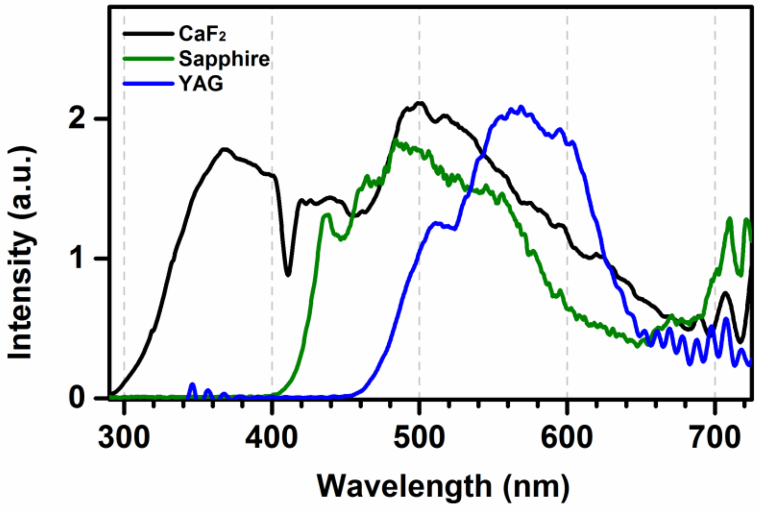

Figure 4.3: Spectra of the continua generated in CaF_2, sapphire and YAG under the fundamental 800 nm pumping.

The threshold of SC generation is under 3 μJ, and a slight increase of the pump energy gives a stable single filament. Upon further increasing the energy, the spectral broadening increases and a plateau-like spectrum starts to develop. When the pump energy is increased over 5 μJ, spectral interference and wiggles are observed. Generation of a continuum is always associated with self-focusing, which leads to a largely increased intensity and therefore enhances self-phase modulation. When the pump energy is low, self-focusing is not reached before the beam gets out of the medium. As the pump energy is increased to a critical value, the continuum generation is started. This critical value can be defined as the continuum threshold, which is slightly higher than the threshold causing self-focusing. The threshold of self-focusing is given by[135]

$$P = \frac{0.15\lambda^2}{n_0 n_2} \tag{4.1}$$

where n_0 and n_2 are linear and nonlinear refractive indices of the medium, and λ denotes the central wavelength of the pump pulse. When the pump power is low but enough to start self-focusing, for a medium with a certain thickness shorter than the self-focusing length, the self-focus of the beam will be out of the medium and thus the self-modulation is not enhanced. The self-focusing length is given by[125]

$$Z_{\mathrm{sf}}(P) = \frac{0.367ka_0^2}{\left[\left(\sqrt{R}-0.852\right)^2-0.0219\right]^{1/2}} \tag{4.2}$$

where $k = 2\pi/\lambda$ is the wave number, a_0 is the radium of the pump beam at the $1/e$ level of intensity, and $R = P/P_{\mathrm{th}}$ is the energy ratio between the pump beam and the threshold of self-focusing. Equation (4.2) shows that high intensity is required to reach short self-focusing length. The continuum threshold can be understood as the intensity where the self-focusing length equals the thickness of the medium. When the continuum generation is initiated but the pump intensity is not high enough to induce strong self-modulation, a narrow spectral broadening is commonly observed. The continuum broadening increases with an increase of intensity. Limited by the bandgap of the medium, a further increase in the intensity cannot produce more spectral components but creates multiple filaments.

The output polarization of SC light is calibrated by using a Glan polarizer. It is observed that most parts of the SC are polarized in the direction of the incident pulses polarization, but a small part of the spectrum in the blue wing changes polarization. A continuum is supposed to maintain the same polarization direction as its incident pump for an isotropic medium.[105] However, due to self-induced polarization changes of the pump light in isotropic media with cubic crystal structure, such as CaF_2, an intensity modulation of the blue wing of the SC along polarization axes orthogonal to the polarization of the pump beam could occur.[133]

The spectrum of SC pumped by the second harmonic pulses is shown in Figure 4.4. The SC spectrum spans most of the visible range and extends into the deep UV up to 240 nm. The missing part of the spectrum from 370 nm to 450 nm is due to the 400 nm high-reflective mirror which is used to isolate the SC from the 400 nm pump light. According to Equation (4.1), the continuum generation strongly depends on the pump wavelength. Shorter pump wavelengths lower the self-focusing threshold, and therefore less energy is needed to initiate the continuum generation. The continuum generation occurs above a threshold value of less than 2 μJ. It is interesting to note that, pumping at 400 nm enables the anti-Stokes side extending more into UV compared to 800 nm pumping, but the overall broadening is less. The Stokes side of the SC pumped by 400 nm is cut-off at 600 nm which is at least 200 nm less than pumped by 800nm. It seems that tuning the pump wavelength to be shorter results in a narrower SC spectrum. Such a behavior has been observed in other studies[115, 131] and explained as the competition between multi-photon excitation and self-phase modulation.[125] For example, if the bandgap E of the medium is in relation with the incident photon ν as $E/h\nu$, free electrons induced by two photon absorption restricts self-focusing.

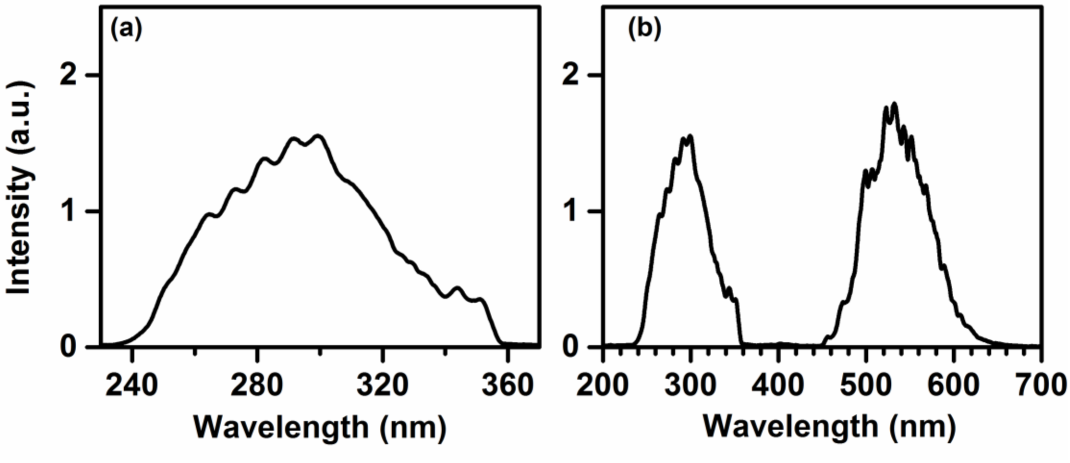

Figure 4.4: The SC generated in CaF_2 with the second harmonic pump source. (a) The anti-Stokes side of the generated SC is highlighted. (b) SC spectra in UV and visible. A 400 nm high-reflective mirror is used to remove the pump, which results in the spectral gab around 400 nm.

4.2 Multichannel detection system

To characterize the spectral properties of the generated SC, a multichannel detection system is designed, which comprises a spectrometer and a photodiode array. For the application of UV time-resolved spectroscopy, the detection system is required to be able to efficiently realize data acquisition with minimal signal loss. In the beginning stage of our experiments, a commercial grating-based spectrometer (Oriel, Newport) was applied (Figure 4.5 (a)). A 150 mm lens focused the SC to the slit, which has a width of 50 μm. A spherical mirror was used to collimate the SC and reflect it to the grating. Each frequency component was spectrally separated and horizontally focused to the photodiode array after the second spherical mirror. The whole detection setup is very easy to align, and versatile for different spectral ranges by simply changing the grating which has high reflection efficiency in the spectral range of interest. However, for the broad spectral range (250 nm to 700 nm) in our measurements, there is no suitable commercial grating available, which can provide high efficiency for all frequency components, especially in the UV. The low efficiency of grating will decrease the detection sensitivity, and therefore leads to undesired baseline and signal shifts.[136]

In addition to grating, prisms are also very common materials providing angular dispersion. The advantages of using a prism over a grating as the dispersive element in the spectrometer (Figure 4.5 (b)) are: (1) high transmission throughout the whole spectral range of the SC, without zero or high order loss, (2) avoidance of the order sorting problem, when the spectrum of SC spans more than one octave, spectral components from different orders may overlap on the same pixel, and (3) high spectral resolution in the blue part of the spectrum due to the wavelength dependence of the dispersion.[132]

After the dispersion in prism, the beam is focused horizontally by a quartz lens. The combination of the prism and the lens is chosen depending on the geometry of the photodiode array. In our case, a fused silica prism together with a 20 mm focusing lens allows spectral components from 300 nm to 650 nm imaging into the photodiode array which contains a sensor with area of 12.5 x 2.5 mm^2. The photodiode array is placed on the horizontal focal point of the SC to achieve the optimal spectral resolution and highest detection intensity.

To calibrate the wavelength of the multichannel detection system, a set of band-pass filters from 300 nm to 800 nm with 10 nm differences in the center wavelength are used. The known spectrum of each filter can be used to assign the wavelength to its corresponding pixel. In our routine measurement, 20 filter/pixel couples are sufficient to use as input data for a nonlinear curve fitting ($y = a_1 + a_2 e^{b_1 x} + a_2 e^{b_2 x}$, y: wavelength, x: pixel, a_1-b_2: fit parameters) which correlates each of the 256 pixels to a wavelength.

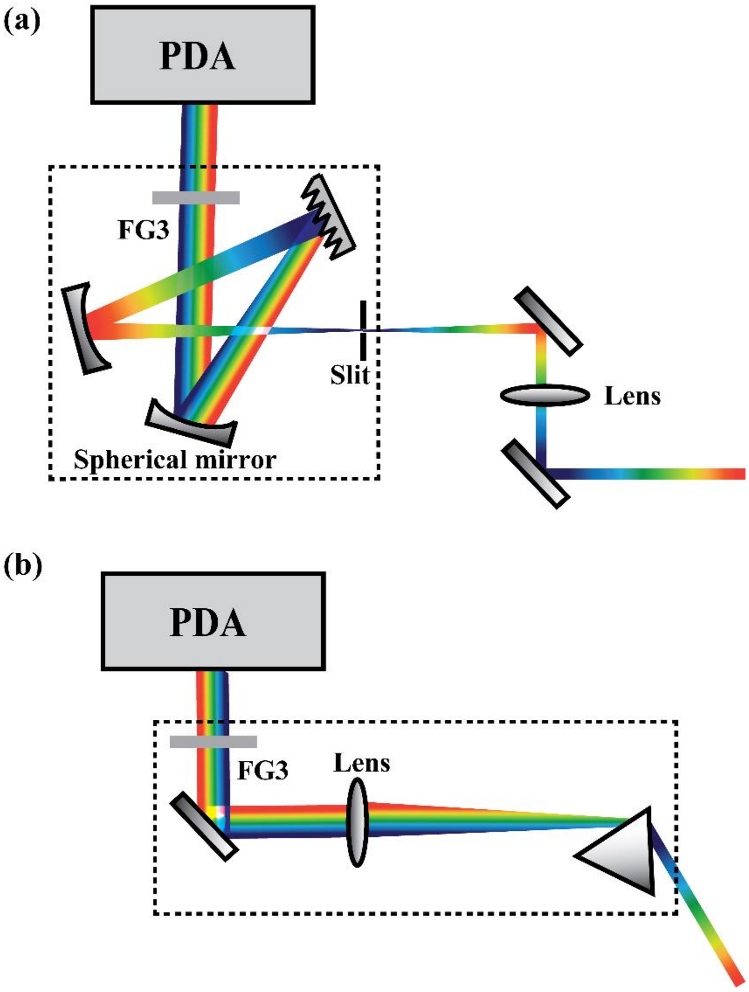

Figure 4.5: Schematic diagrams of the multichannel detection system. The spectrometers are marked with dashed lines. (a) Grating-based spectrometer. A fused silica lens with a focal length of 150 mm focuses the SC to the 50 μm slit. A spherical mirror (10 cm focal length) is used to collimate the SC and reflect it to the grating (77417, Oriel). The first order of the SC is horizontally focused into the PDA by another spherical mirror (10 cm focal length). (b) Prism-based spectrometer. The fused silica prism is cut such that the angle of incidence is the Brewster angle at the central wavelength. After the prism, the SC is horizontally focused into the PDA by a 20 mm focusing lens. The FG3 filter (Schott) is used to suppress the strong components around 600 nm in order to balance the intensity of the whole spectrum to be detected.

Chapter 5

Implementation and Performance of the UV Transient Absorption Experiment

This chapter addresses the principal of the transient absorption (TA) experiment. All relevant components which play a role in building and running a femtosecond UV TA experiment are assembled to give a complete pump-probe system. Data processing including time-zero correction and coherent artifact subtraction, as well as data analysis by using multi-exponential analysis and global target analysis are elucidated. The performance parameters are crucial in the study of ultrafast molecular and chemical dynamics. The entire pump-probe system, including the experiment measurement software, is tested in the study of the electronic levels and the dynamics of the excited state of 7-hydroxy coumarin.

5.1 Transient absorption experiment

In TA spectroscopy, the pump pulse induces the transition of a fraction of the molecules to the excited state by a vertical Franck Condon transition and the induced optical transmission changes are monitored as a function of delay time by the absorption measurement of the broad continuum probe (Figure 5.1). According to Lambert Beer's law, the change of spectral intensity $OD(\lambda, \tau)$ of the probe light propagating through the sample is recorded as

$$OD(\lambda,\tau) = \log_{10}\frac{I_0(\lambda)}{I(\lambda,\tau)} = c\cdot\varepsilon\cdot d \tag{5.1}$$

where $I_0(\lambda)$ is the spectral intensity of the probe light before passing through the sample, $I(\lambda, \tau)$ is the spectral intensity of the probe light having passed through the sample at a delay time τ after the photo-excitation, c is the concentration of the absorbing substance, ε is the molar absorption coefficient, and d is the path length of the sample. In practice, transient absorption meausrements are generally presented as the difference absorbance of the sample, which can be calculated as:

$$\Delta OD(\lambda,\tau) = \log_{10}\frac{I_0(\lambda)}{I(\lambda,\tau)_{\mathrm{on}}} - \log_{10}\frac{I_0(\lambda)}{I(\lambda,\tau)_{\mathrm{0ff}}} = \log_{10}\frac{I(\lambda,\tau)_{\mathrm{0ff}}}{I(\lambda,\tau)_{\mathrm{on}}} \tag{5.2}$$

where $I(\lambda,\tau)_{\mathrm{on}}$ and $I(\lambda,\tau)_{\mathrm{off}}$ denote the transmitted intensity of the probe light having passed through the excited sample and the unexcited sample, respectively. The alternating pumping of the sample is realized by blocking every second pump pulse. The setting of a variable and well-defined delay time τ between the pump and the probe light enables the collection of spectra as a function of time. The recorded TA spectra $\Delta OD(\lambda, \tau)$ is a combination of several negative and positive signals. Assignment of the various signals permits discussion of the nature of excited states. If $I(\lambda,\tau)_{\mathrm{on}} > I(\lambda,\tau)_{\mathrm{off}}$, a transient gain is observed, which results in the depopulation of the ground state with possible stimulated emission.[137] When the sample is excited by the pump, a certain amount of the molecules from the ground state are transferred to the excited state. Thus, after excitation, the probe light will be less well absorbed in the spectral range of static absorption, which leads to a negative signal known as the ground state bleach (GSB) (Figure 5.2 (a)). The amplitude of the GSB is proportional to the total population in the excited states. If an excited state has optically allowed transitions back to the ground state or relaxing to lower states, the probe light in certain wavelengths can stimulate this transition with additional photons emitted, from which a negative signal called stimulated emission (SE) is observed (Figure 5.2 (b)). If $I(\lambda,\tau)_{\text{off}} > I(\lambda,\tau)_{\text{on}}$, a positive signal is observed. The predominant cause of the positive absorption is optically allowed transitions from the initial excited state to higher energy excited states (Figure 5.2 (c)). If a chemical reaction is caused by the pump pulse, a created species or product can also show a positive absorption signal.

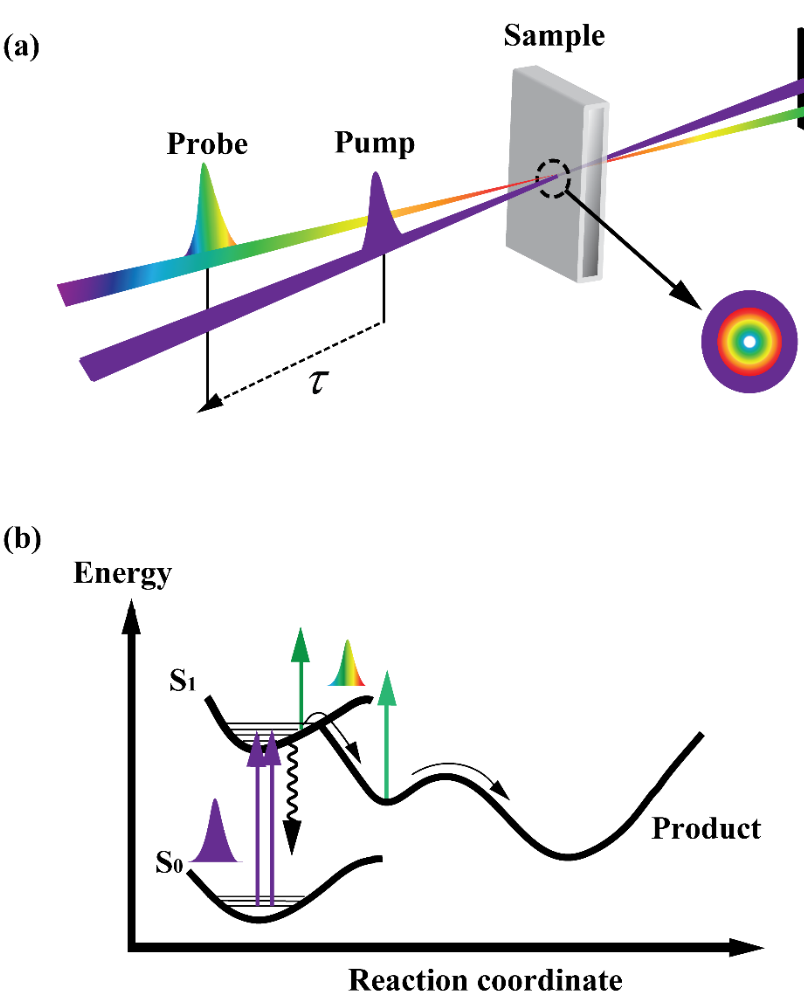

Figure 5.1: (a) Schematic depiction of the principle of TA spectroscopy. Two ultrashort laser pulses, the pump pulse and the probe pulse, are incident on a sample in which they are spatially overlapped. The transmitted probe pulse is recorded by the detector which can be a single-channel detection system, such as photodiode, or a multichannel detection system, such as CCD. The TA spectra are calculated as the difference absorbance between the excited sample and unexcited sample. (b) Energy level diagram representing the excited states dynamics. TA spectroscopy provides information about how the excited states are populated and relax.

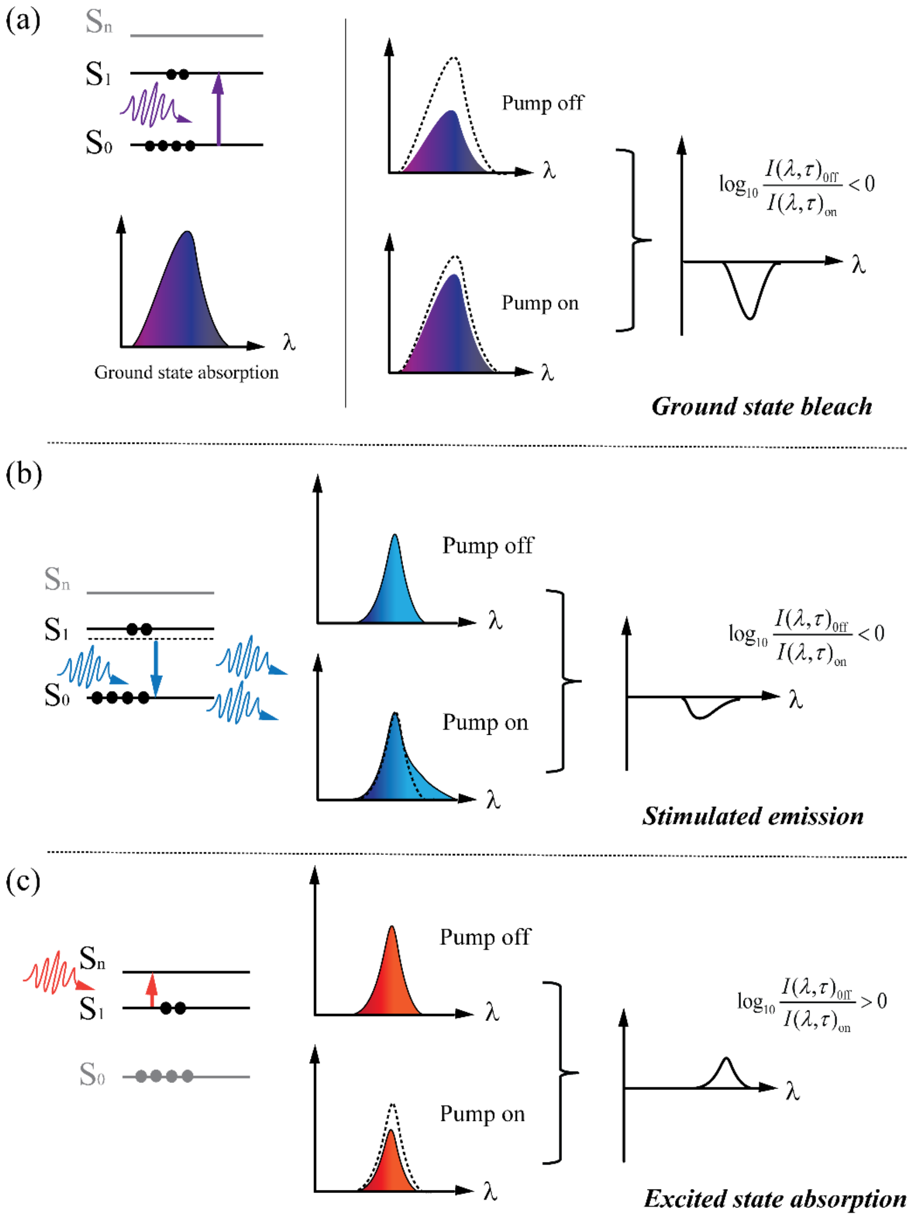

Figure 5.2: Different contributions to the transient absorption signal. When the pump light is on, a fraction of the molecules are excited to the excited state by the pump light, thus the number of molecules on the ground state is reduced. (a) The first contribution is from the *ground state bleach*. After excitation, the probe light in the region of the ground state absorption of the molecule is absorbed less resulting in a negative signal. (b) When the probe photon induces emission from the excited state, a negative signal called *stimulated emission* (SE) is observed. (c) The probe light can promote the population from the excited state to higher excited states, which gives a positive signal called *excited state absorption*.

5.1.1 Pump-probe experimental setup

In the previous chapters, the most relevant components employed in our TA pump-probe setup, such as the tunable UV pump source and the supercontinuum probe light, have been described in detail. In this section, the complete implementation of the whole pump-probe setup will be given, as shown in Figure 5.3. The idea behind the design and arrangement of the whole setup is that all optical paths of both pump pulses and probe pulses should be kept as short as possible to reduce the dispersion induced by air, whilst utilizing the minimum number of optics in order to avoid energy loss by either reflection or absorption. Moreover, an open layout of the pump-probe system is designed to facilitate the daily adjustment and operation. Finally, the setup is constructed to be flexible so that it can be routinely adapted to other possible experimental techniques, for example single-beam coherent anti-Stokes Ramen scattering (CARS) or shaped UV pulse TA spectroscopy.

As a light source, a regenerative Ti:sapphire amplifier system (CPA 1000 Clark-MXR) is utilized, which delivers 640 μJ-pulses at 800 nm with ~100 fs duration, 10 nm bandwidth and a repetition rate of 1kHz. The TA setup for our measurements is based on two tunable femtosecond UV pump sources (SHG and SFG NOPA) and two broadband continua (sapphire and CaF_2) for the wavelength selective pumping and probing, respectively. A general view of the pump and probe pulses are given here, and details have been discussed in chapter 2 and 4, respectively. For the pump, a 300 μJ/pulse portion is used to operate the SHG UV NOPA and 400 μJ pulses are selected to pump the SFG UV NOPA. The SHG UV NOPA is based on frequency doubling of the compressed visible pulses, which provides the generated UV pulses with tunable spectral range from 250-350 nm and sub-30 fs pulse duration. The other UV NOPA is based on frequency mixing between chirped 800 nm pulses and visible pulses, which creates an excitation spectrum with a tunable range from 300-350 nm. According to the static absorption spectrum of the sample to be investigated, the pump light can be easily switched between two UV NOPAs by flipping two aluminium mirrors. To adjust the pump energy to meet the needs of the sample, a neutral density filter is placed prior to the generation of UV pulses to attenuate the energy of the input visible pulses. The insertion of optics into the optical path after UV generation is avoided. In order to vary the delay time between the pump pulses and probe pulses, the pump is delayed with a retro-reflector mounted on a motorized, computer-controlled translation stage and the optical path of the probe light is kept constant. Every second pump pulse is blocked with a chopper wheel, which is controlled by a 500 Hz signal synchronized with the laser trigger. In this way, the sample is alternatively being excited and not excited.

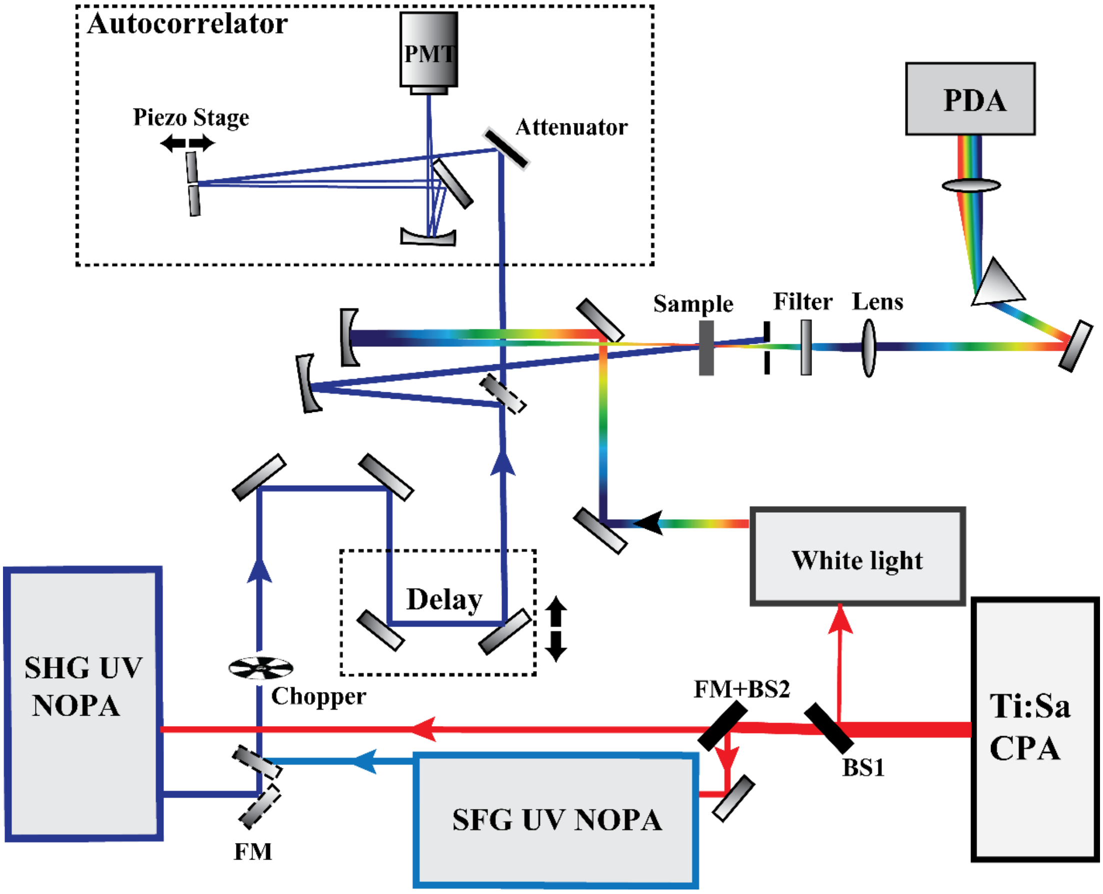

Figure 5.3: Schematic representation of the ultrafast UV TA experimental setup. 5 % of the output from the Ti:sapphire amplifier is split off and used to power a supercontinuum combination. The remaining energy is used to operate either the SHG UV NOPA or the SFG UV NOPA. After passing the chopper, the UV pump beam is sent through a delay line. The pump and probe beams are focused onto the sample, and the transmitted probe is detected by the multichannel detector. FM: flip mirror, BS1: 5 % reflection beam splitter, BS2: 70 % reflection beam splitter, PMT: photomultiplier tube, Attenuator: neutral density filter, PDA: photodiode array, Filter: FG3 filter (Schott), lens: quartz lens with 150 mm focal length.

The characterization of the UV pulses is realized using a solar-blind photomultiplier tube (PMT) via two photon absorption (for details see chapter 3). To ensure the UV pulses reaching in the sample have the same duration as measured in the PMT, the optical paths from UV generation to the PMT and to the sample are adjusted to be identical.

For the probe light, 5 % output of the CPA system is used to support several variants of supercontinuum generation: one comprises of a visible continuum generated in 2 mm sapphire, and the other are two UV-VIS continua generated in CaF_2 pumped by 800 nm and 400 nm, respectively. The whole supercontinuum spectrum spans from the deep UV 240 nm to near 800 nm. The desired spectral range of probe light can be chosen by flipping two aluminium mirrors. Most of our measurements are performed in solutions and therefore carried out at the magic angle (54.7°) to eliminate anisotropic effect.[138] Contrary to the traditional pump-probe experiments performed in the visible range, [132, 139, 140] we do not change the polarization of the pump pulses but rather the polarization of the probe pulses, which prevents any UV pulse distortion by passing through the 2 mm half wave plate. Due to the lack of accurate, broadband half wave plates working from 300-700 nm the polarization of the probe light is set by placing an 800 nm half wave plate before the continuum generation. The orientation of the continuum substrate is adjusted with respect to the polarization of the laser. A linear polarized continuum with a high extinction ratio is obtained.

The pump and probe pulses are spatially overlapped and focused into the sample with spherical mirrors of 30 cm and 25 cm focal length, respectively. The focusing spot of the pump light is slightly bigger than the probe. After passing through the sample, the pump light is blocked, and the continuum probe light is dispersed in a prism-based spectrometer and recorded by a photodiode array. Data recording is performed using Labview programs (homebuilt) in a PXI system (National Instruments), which provides high performance synchronization and fast data storage. The Labview-based program provides a visual control of all relevant data, which enables a real-time handling of the measurement parameters.

5.1.2 The design of the flow cell

For the measurements performed in solution, usually the sample is either placed in a static cuvette, or circulated in a flow cell to prevent overexposure of the same excited volume and accumulation of products. For our experiments, a flow cell was designed and constructed to exchange the solution continuously with controlled speed and volume, shown in Figure 5.4. The design of the flow cell follows two requirements. On one hand, the length of the optical path through the two windows and the spacer should be minimized to keep a good experimental time resolution. The group velocity mismatch between the pump and probe pulse, as well as material dispersion induced pulse lengthening, lead to deterioration of the time resolution. The thinnest windows we are able to commercially obtain are 200 μm polished quartz windows. It is important to note that the driving speed and volume of the flow cell have to be set carefully to prevent any mechanical break of such thin windows. Several spacers with different thickness, 500, 350 and 250 μm are produced by the mechanical workshop. Using an extremely thin spacer improves the time resolution at the cost of the sample concentration. On the other hand, as mentioned in the chapter of UV pulse characterization, the entrance window of the PMT falsifies the characterization of pulse duration. Therefore, to overcome this problem and make the pulse characterization reliable, the front window of the flow cell is designed to have a similar thickness as the PMT window.

The samples we are interested, coumarin dimers, are only available in very small amounts because of the low efficiency of dimerization.[141] However, a high concentration of the sample is required to reach a desired optical density (at least 0.3 OD) in the extremely thin flow cell. To save the limited amounts of sample for multiple measurements, the volume of the sample has to be kept as small as possible. The pump-head device (Masterflex, Console Drive 77390) is applied to drive the sample, which permits an overall volume of the sample as low as 3 ml.

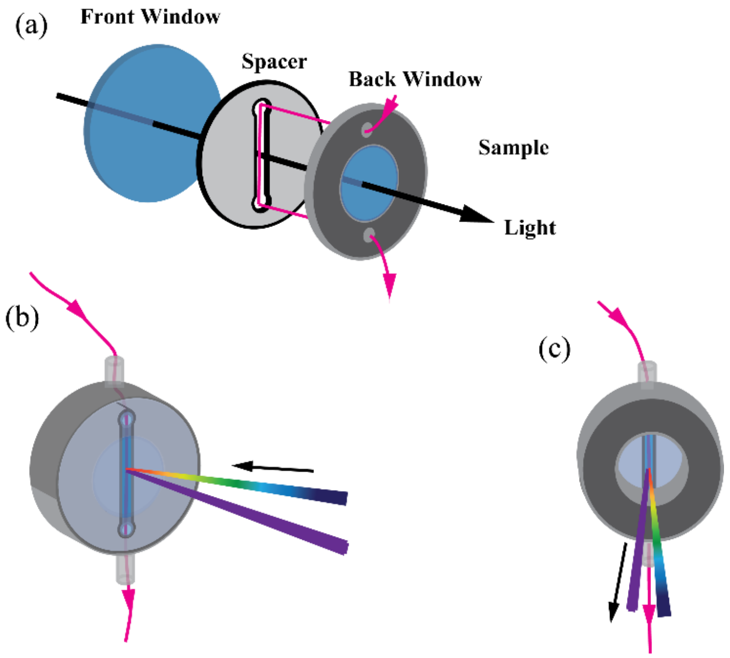

Figure 5.4: Scheme of the designed flow cell. (a) The thickness of the front window is about 1.5 mm and the back window is about 200 μm. The flow cell is held together by metal flanges, which can be mounted on a holder with three-dimension translation stage. (b) Front side of the flow cell. (c) Back side of the flow cell.

5.2 Data processing

The recorded experimental data contain not only substantial dynamical information of the sample to be studied, but also undesired coherent artifacts that arise from the pump-probe nonlinear interactions at the time zero, which are also solvent and substrate/window material dependent. Meanwhile, each spectral component of the chirped supercontinuum probe enters the sample at different times for any specific setting of the pump-probe delay (Figure 5.5 (a)), therefore the time zero of observed kinetics at each wavelength is different. These situations are disadvantageous as the coherent artifact notably distorts the data structure and subsequently increases the difficulty of the analysis for the initial dynamics, especially the amplitude is comparable to weak transient signals (Figure 5.5 (b)). However, the coherent artifact can help to determine the system's parameters, such as the instrument response function and correct the spectra for temporal dispersion. In the following, a theoretical model of the coherent artifact is studied, from which a simulated nonresonant signal is obtained. To extract the correct, artifact free TA spectra of the sample under study, coherent artifacts are subtracted and the time-zero is corrected.

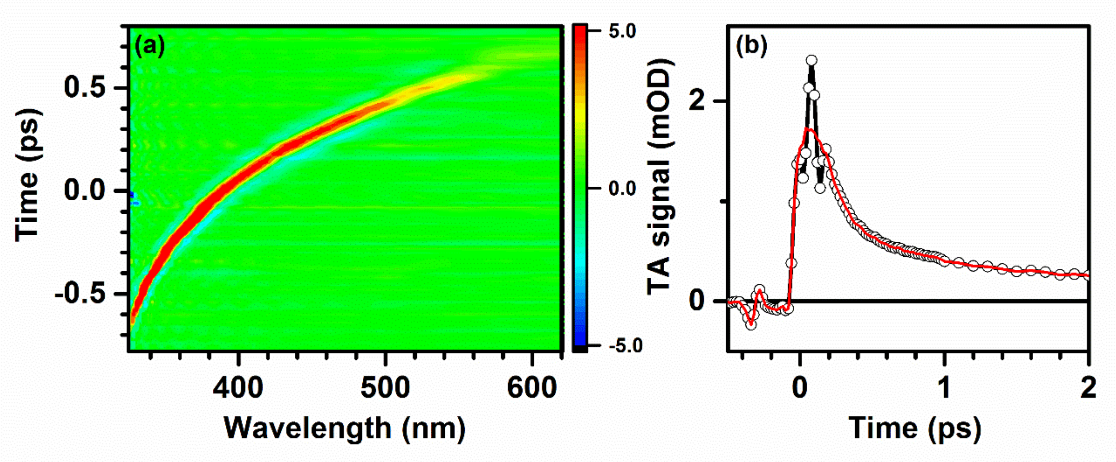

Figure 5.5: (a) TA signal measured in ethanol solvent (λ_{exc} = 280 nm, τ_{exc} = 28 fs, energy = 100 nJ). The time axis is associated with the delay time between the pump and the probe. The positive time means the pump pulse comes before the probe pulse. In our experiment, the supercontinuum probe is positively chirped, so the low frequency components travel faster than the high frequency components. The time-zero point is arbitrarily set at 390 nm. (b) TA trace of coumarin dimer taken at the probe wavelength of 375 nm (black dot-line), and pure kinetic trace without coherent artifacts (red line).

5.2.1 Coherent artifacts

Coherent artifacts are intrinsic to the TA pump-probe experiment, which are produced by the simultaneous nonlinear mixing between one photon from the pump pulse and another one from the probe pulse. There are mainly three nonlinear processes which contribute to coherent artifacts: two-photon absorption (TPA),[72, 85] stimulated Raman scattering (SRS)[142] and cross-phase modulation (XPM)[143]. Simultaneous absorption of a pump photon and a probe photon gives rise to TPA; the energy difference of two incident photons corresponding to the vibrational oscillation of the medium gives rises to SRS; the phase modulation of the probe pulse induced by the intense pump pulse gives rise to XPM.

In the TA measurements, when the frequencies of the pump and the probe match the condition $h\upsilon_{pump} + h\upsilon_{probe} > E$ (energy gap of the medium), the TPA is possible and more pronounced with the higher frequency component of the probe. TPA occurs in almost all organic solvents under UV pulse excitation below 350 nm.[144] According to Equation (5.2), the TPA induced absorption translates into a positive ΔOD signal (Figure 5.6 (a)). If TPA induced fluorescence takes place, a reverse negative signal can appear at a shorter wavelength. Since the self-induced TPA of the probe pulse can be neglected, according to Equation 3.5, the TPA signal increases linearly with pump intensity.

A SRS signal appears more likely when the frequency of the probe is partially red-shifted with respect to the frequency of the pump. The very broad spectrum of the supercontinuum probe provides a good chance that some components may fall into the spectral region being able to seed the coupling between the molecular vibrational ground state and a virtual energy level. The emission contribution from the SRS usually translates into a negative ΔOD signal (Figure 5.6 (c)). However, a reverse situation is also possible when the frequency of the probe pulse is higher than the pump pulse. The probe pulse is absorbed to reach the virtual Raman level and the pump pulse acts as a Stokes pulse. It is important to note that the pump pulse induced frequency modulation of the probe pulse can cause a small spectral shift in the observed SRS signal.[144] In our case, the contribution from SRS can be neglected, because the smallest energy separation between the pump pulse (270/280 nm) and the probe pulse (300-650 nm) is more than 3000 cm^{-1} which is out of the range of vibrational modes for ethanol and acetonitrile used in the experiments.

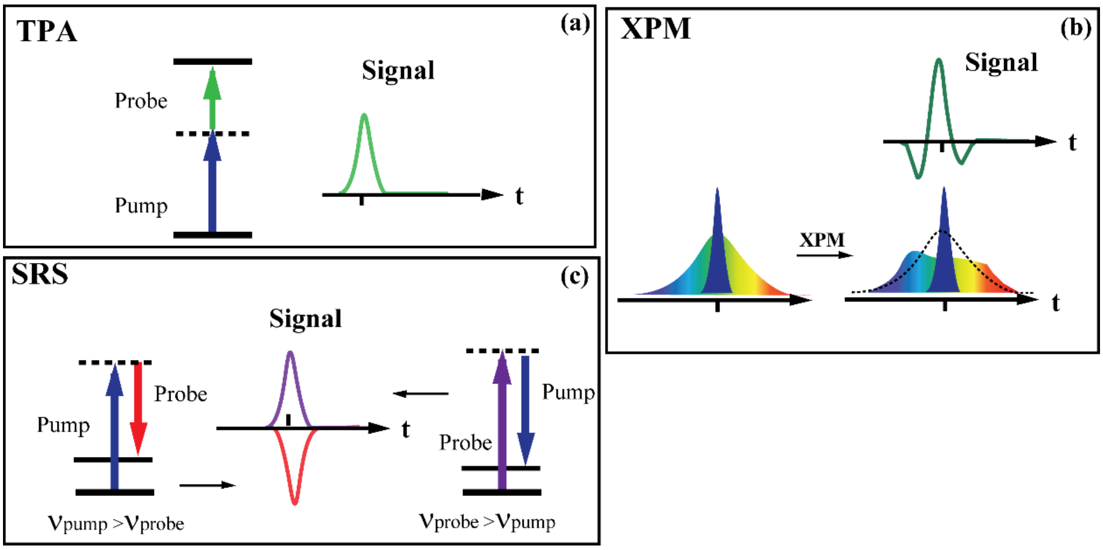

Figure 5.6: The contributions to the coherent artifact. (a) Simultaneous absorption of one pump photon and one probe photon gives rise to a positive TPA signal. (b) Frequency components of the probe interacting with the maximum of the pump pulse are pushed outwards resulting in decreasing intensity in the central part of the probe pulse and increasing in the probe pulse wings. (c) SRS contributions in two different conditions: the frequency of the pump is higher than the probe then the probe carries a negative signal, and the reverse, if the probe has higher frequency then it carries a positive signal.

For the XPM process, the phase modulation induced by intense pump pulses occurs in all spectral components of the probe pulse. Assuming the temporal distribution of the pump pulse is a Gaussian shape, $I_{pump}(t) = |A(t)|^2 = A_0^2 e^{-2t^2/\tau^2}$, the modulated probe pulse with centre frequency, ω_0, can be expressed as[144]

$$\omega_{probe}(t) = \omega_0 + \beta t + \frac{8n_2 L\omega_0}{c\tau^2} t I_{pump}(t) \tag{5.3}$$

where β is the coefficient of linear chirp, n_2 is the second order refractive index, L is the thickness of the sample. The modulation is dependent on the intensity of the pump pulse. The frequency modes around ω_0 overlapping with the maximum of the pump pulse experience the most modulation, thus the spectral density of those modes is decreased, which is observed as a positive ΔOD signal. The frequency modes $>\omega_0$ and $<\omega_0$ overlapping with the wing of the pump pulse experience the least modulation and subsequently gain amplification from the modulation of modes around ω_0, thus the spectral density of these frequency modes are increased, which translates into a negative signal. In summary, the spectral density is transferred from the centre of the probe to the wings. This trend features the XPM signal with a shape of peaked middle and dipped wings (Figure 5.6 (b)). The intensity of the XPM signal is proportional to $d\omega_{probe}(t)/dt$. From Equation (5.3), the XPM signal can be approximated as:

$$I \propto d\omega_{probe}(t)/dt = \beta + \frac{8n_2 L\omega_0}{c\tau^2}\left(I_{pump}(t) + t\frac{dI_{pump}(t)}{dt} \right) \tag{5.4}$$

which means higher frequencies, greater probe chirp and shorter pump pulses give greater XPM signal.

The resulting coherent artefact signal is a linear combination of the three nonlinear processes in different proportions, as each contribution is linearly dependent on its corresponding third-order polarization. In practice, the contributions from TPA and SRS are very small, therefore the coherent artifacts for non-chirped probing can be well fitted by the XPM function, or more precisely by an approximation of the XPM function with its time derivatives as[145]

$$S(t) = A_1 S_{\mathrm{XPM}}(t) + A_2\frac{dS_{\mathrm{XPM}}(t)}{dt} + A_3\frac{d^2 S_{\mathrm{XPM}}(t)}{dt^2} \tag{5.5}$$

where A_1-A_3 are constants.

If pump and probe wavelengths are different, the group velocity dispersion (GVD) has to be taken into account, which is dependent on the difference between refractive index values for pump (n_{pump}) and probe (n_{probe}). The velocity mismatch causes temporal broadening of the coherent artifact. For the chirped probing, the temporal width of the artifact varies with the probe wavelength. Except for the frequency difference between the pump pulse and probe pulse, the path length L also contributes to the temporal width of the artifact. To minimize the temporal width of the artifact, the flow cell should be designed to be as thin as possible.

The XPM function $S_{\mathrm{XPM}}(t)$ is given by [144]:

$$S_{\mathrm{XPM}}(t) = 2\log\left(1 + a\left(te^{-2t^2/\tau^2} - (t-\tau_{GVD})e^{-2(t-\tau_{GVD})^2/\tau^2}\right)\right) \tag{5.6}$$

where $a = \frac{8\omega_0 n_2 L A_0^2}{c\beta\tau^2\tau_{GVD}}$, and $\tau_{GVD} = \frac{L}{c}(n_{\text{pump}} - n_{\text{probe}})$. Because the second term in Equation (5.6) is usually much less than 1, then the XPM function is derived approximately by making use of the first term of the logarithm expansion:

$$S_{\text{XPM}}(t) \approx 0.86a\left(te^{-2t^2/\tau^2} - (t-\tau_{GVD})e^{-2(t-\tau_{GVD})^2/\tau^2}\right). \tag{5.7}$$

Inserting Equation (5.7) into (5.5), the coherent artifact signal is expressed as:

$$\begin{aligned} S_{CA}(t) &= A_1 a\left(te^{-2t^2/\tau^2} - (t-\tau_{GVD})e^{-2(t-\tau_{GVD})^2/\tau^2}\right) \\ &+A_2 a\left(\left(1-4t^2/\tau^2\right)e^{-2t^2/\tau^2} - \left(1-4\left(t-\tau_{GVD}\right)^2/\tau^2\right)e^{-2(t-\tau_{GVD})^2/\tau^2}\right) \\ &+A_3 a\left(\left(3-4t^2/\tau^2\right)\left(-4t/\tau^2\right)e^{-2t^2/\tau^2} - (3-4\left(t-\tau_{GVD}\right)^2/\tau^2)\left(-4\left(t-\tau_{GVD}\right)^2/\tau^2\right)e^{-2(t-\tau_{GVD})^2/\tau^2}\right). \end{aligned} \tag{5.8}$$

5.2.2 Time zero correction

The spectrally broad probe pulses are obtained using the generation of supercontinuum. The supercontinuum is temporally chirped, usually positively chirped due to the self-phase modulation (SPM) and GVD in the generation itself. As shown in Figure 5.5 (a), the time evolution of the coherent artifact is evidence of positive chirping of the probe pulse, as the pump pulse is almost transform limited. At certain settings of the pump-probe delay stage at t_d, different spectral components of the probe interact with the pump at different time, therefore for the frequency component ω of the probe the actual delay t in Equation (5.8) should be replaced as

$$t(\omega) = t_d + t_0(\omega) = t_d - \partial\varphi/\partial\omega \tag{5.9}$$

in which a time-zero function $t_0(\omega)$ is introduced and φ is the phase of the chirped probe pulse. The time zero corresponds to the delay setting where the pump and the probe are exactly overlapped in time. The most commonly used methods to obtain the time-zero function are based on the coherent artefact either from pure solvents or from a transparent substrate.[146, 147] Inserting Equation (5.9) into (5.8), a function of coherent artifacts for chirped probing is obtained, in which $t_0(\omega)$ presents as one of the parameters. Fitting this function to the coherent artifact data measured in the pure solvent, the values of $t_0(\omega)$ for all detected wavelengths are obtained (Figure 5.7 (c)). These points can be fit with a 3rd or 4th order polynomial function, which describes the time-zero function for the whole data set. Moreover, the trace of $t_0\,(\omega)$ can also be depicted by locating the peaks of coherent artifacts (Figure 5.7 (c)). The positive maximum of the coherent artefact signal shifts in time with the probe frequency, which reflects the dispersive features of the chirped probe pulse with an accuracy better than 10 fs. However, if the frequency of the probe pulse is very far apart from the pump pulse, GVD and XPM lead to multiple peaks in the coherent artefact signal (Figure 5.7 (b)), which may introduce errors in picking the correct peak. Therefore, for the UV-pump/visible-probe measurements, especially in the case when the frequency difference between the pump and probe is over 10000 cm^{-1}, by fitting coherent artifacts one can gain a more precise time zero correction. With the help of the time-zero function, the TA spectra can be temporally corrected by shifting the raw data along the time axis with the corresponding $t_0\,(\omega)$. The process of time zero correction can be considered as a synchronization for all probe wavelengths. The raw TA spectra and the spectra after time-zero correction are shown in Figure 5.9 (a) and (c).

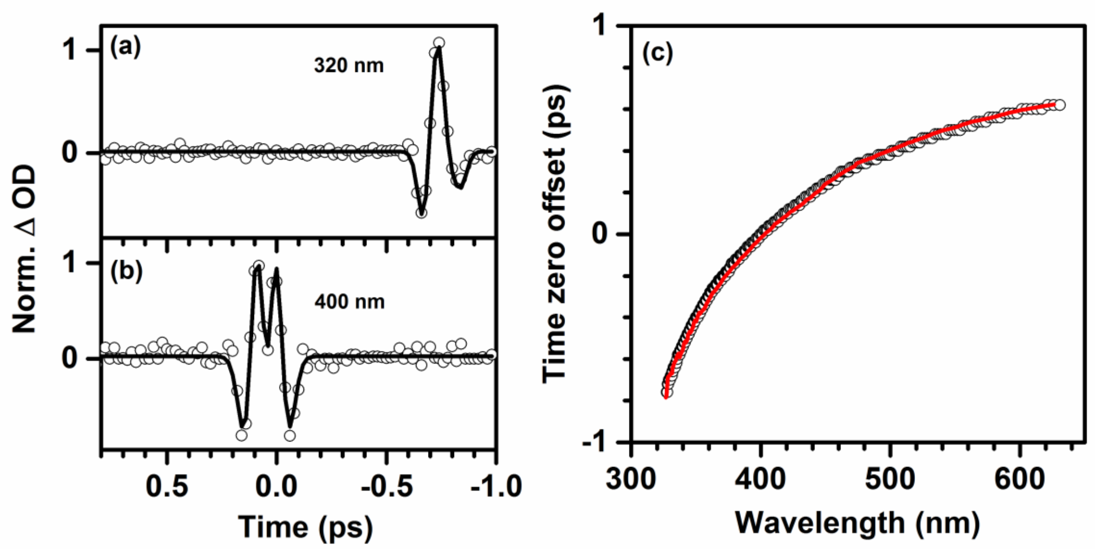

Figure 5.7: There is a ~ 0.75 ps temporal dispersion of the coherent artifacts between (a) 320 nm and (b) 400 nm. The open dots are experimental data and the solid lines are fits simulated by the coherent artifacts function. (c) The time-zero function (λ_{exc} = 330 nm, energy = 100 nJ, τ_{exc} = 30 fs) obtained by locating the peaks of the coherent artifact signal (empty circle) and the parameter $t_0\,(\omega)$ from the coherent artifact function (red line).

5.2.3 Coherent artifacts subtraction

Removing coherent artifacts from the raw TA data is challenging work because the nonresonant coherent artifacts are temporally overlapped with the resonant signal from the sample around time zero, and vary in shape and time depending on the wavelength of the probe. A procedure for artifact subtraction has been performed by directly subtracting the coherent artifact measured in pure solvents with a weighting factor, which is correlated to the pump pulse intensity.[144] However this method doesn't apply well in the UV-pump/VIS-probe experiment. The molecules under study modulate the refractive index of the solution slightly, therefore the XPM in solution with molecules is not a perfect match with the XPM in the pure solvent anymore, and the deviation can be even more severe in deeper UV pumped experiments. Other proposed methods like singular value decomposition can also be used to subtract coherent artifacts,[134] but the experimental data for delay times longer than the coherent artefact can be easily affected. The method used in our experiments is based on the coherent artifact function discussed in the section above and rate equation models containing kinetic information of the molecule under study. Briefly, the observed TA signal of a single spectral component as a function of delay time can be written as a sum of terms:

$$\Delta OD(t) = S_{CA}(t) + S_M(t) * F_{cc} \tag{5.10}$$

where the first term represents the signal of the coherent artifact and the second term represents the molecular response convoluted with the pump-probe cross correlation. Since the coherent artifact function has been elucidated in details, emphasis will be placed on the second term. In photochemical reactions, the kinetic trace at wavelength λ as a function of delay time can be described by an appropriate multi-exponential function, which will be elaborated on in the section for data analysis. As an example, a single TA trace of coumarin dimer in acetonitrile (Figure 5.8 (a)), pumped by 270 nm and probed at 325 nm, can be fitted with a rate equation function, which contains a rising contribution and two decaying contributions (for details see next section), as shown in the following equation

$$S_{M\_325nm}(t) = A\left(ae^{-t/\tau_{dec1}} + (1-a)e^{-t/\tau_{dec2}}\right)\cdot\left(1-e^{-t/\tau_{rise}}\right) \tag{5.11}$$

where A is the amplitude, a is scaling factor, τ_{dec1} and τ_{dec2} are decay time constants, and τ_{rise} is a rising time constant. Combing Equation (5.8) and (5.11) into Equation (5.10), a model describing the coherent artifact and molecular dynamics with two decay species is formed. Fitting of the model with experimental data is carried out by using the finite-difference Marquardt-Levenberg algorithm, which minimizes the sum of the squares of the residuals (fitted points minus data points) by varying fit parameters.[148, 149] Note that the algorithm does not supply error bars on individual parameters, because it always changes the entire parameter set. The best-fit trace is produced with minimal residual (Figure 5.8 (b)). A Labview routine is developed which runs the calculation and the iteration of the correction matrix for all possible pairs of fit parameters. It is often that the fits of kinetic traces result in a variation of the local minimum, which gives different values of parameters. Therefore, searching the space for best-fit parameters is restricted by the parameter boundaries, such as maximal to minimal values. By carefully choosing the parameter boundaries, and rate equation models, a set of parameters locating in the immediate vicinity of the "best-fit" can be obtained. Since the resulting trace is a linear combination of coherent artifacts and molecular response, the stimulated coherent artifacts can be easily separated. The clean TA data of the molecules is obtained by subtracting the stimulated coherent artifacts from the raw data. TA surface plots with and without coherent artifacts are shown in Figure 5.9. The artifacts-free signal shown in Figure 5.9 (d), allows an accurate analysis of the molecular system being studied.

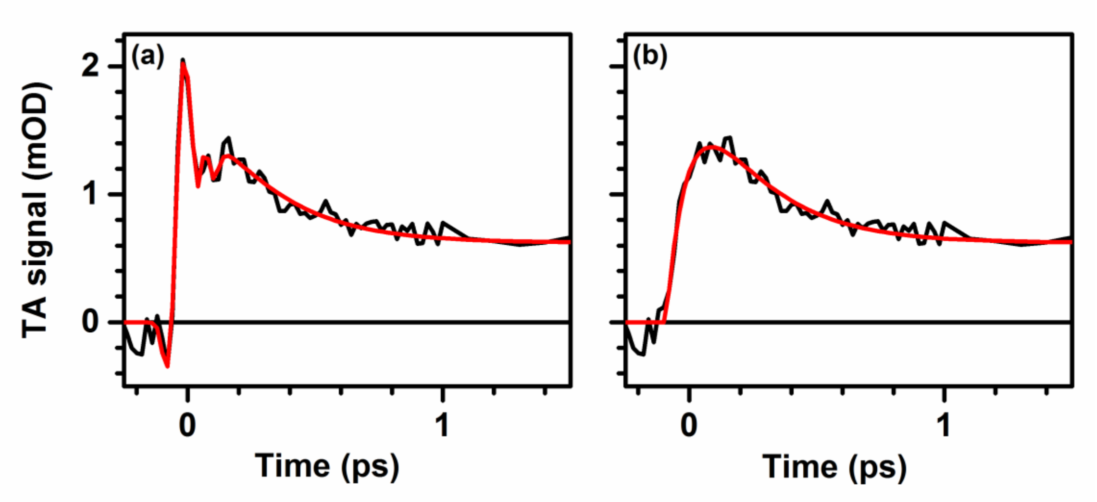

Figure 5.8: TA traces of coumarin dimer (a) with and (b) without coherent artifacts pumped by 270 nm and probed at 325 nm. Raw data are in black line and fitting traces are in red.

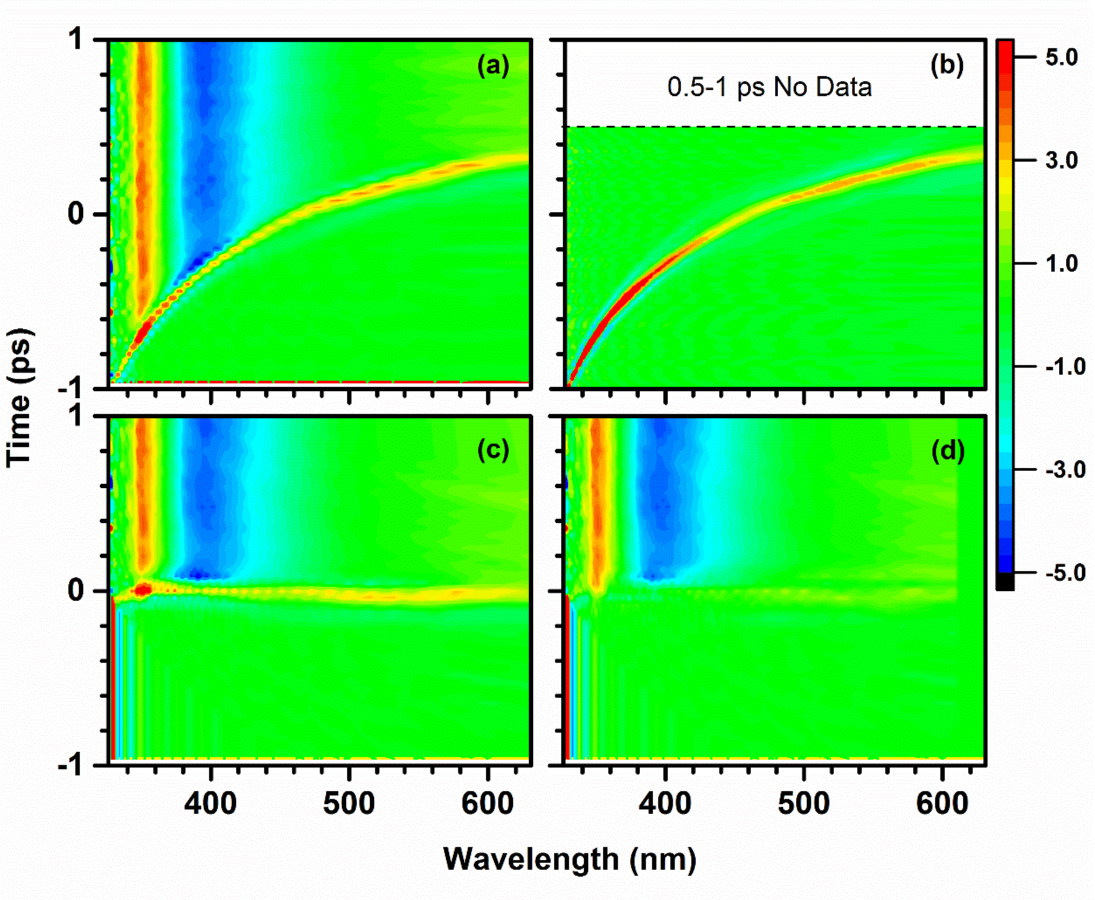

Figure 5.9: (a) Raw TA spectra of coumarin in ethanol (λ_{exc} = 330 nm, energy = 100 nJ, τ_{exc} = 30 fs). (b) Coherent artifacts measured in pure ethanol solvent. (c) Time corrected TA spectra with coherent artifacts. (d) Time corrected TA spectra with coherent artifacts subtracted.

5.3 Data analysis

The obtained experimental data from TA measurements contain a large amount of potential information regarding the dynamics and the nature of photoinduced reactions. The data set in our measurement consists of a series of spectra covering the wavelength range from 300 nm to 650 nm and spanning time delays from several femtoseconds to nanoseconds. These spectra are usually arranged in a data matrix **X** ($m \times n$) where one direction is related to the delay time between the pump and the probe and the other to the probe wavelength. Each row of data presents a spectrum recorded at a certain delay time, and each column corresponds to a kinetic trace as a function of time at a particular probe wavelength. In practice, this matrix is trimmed to exclude wavelengths where the noise overwhelms the signal.

In the analysis routine, the first step is to assess the complexity of the system under study, in other words, to gain an initial estimation of the number of components which are related to the different species, such as intermediate states and products. One simple and commonly used method is the exponential analysis of kinetic traces for different spectral regions. Single kinetic traces can be fitted by appropriate parametric exponential functions,[150] which provide qualitative descriptions of the data without the need of prior knowledge of the mechanistic model. In the simplest case, a transient trace at a probe wavelength λ is fitted to a single exponential, which is characterised by the amplitude A_0 and time constant τ:

$$A(t)_\lambda = A_0 e^{-t/\tau} \tag{5.12}$$

from which we may assume that there is one absorbing species ($A_0 > 0$) or a emission species ($A_0 < 0$) decays with a time constant τ at wavelength λ. Analyzing single kinetic traces by exponential function can work well only when each species has a very distinct spectrum, however, it is not the case in normal circumstances. Usually there are multiple absorbing species with a high degree of spectral overlap, which generates observed decays that do not fit to a single exponential but a multiexponenetial fit. The kinetic trace with multiexponential features can be presented as a sum of exponentials:

$$A(t)_\lambda = \sum_i A_i e^{-t/\tau_i} + \text{const.} \tag{5.13}$$

In our fitting routine of TA traces, a population generation function $B(t) = 1 - e^{t/\tau_{rise}}$ is considered regarding the population excited directly by the pump. Then Equation 5.13 is changed to be the following:

$$A(t)_\lambda = \left(\sum_i A_i e^{-t/\tau_i} + \text{const} \right) (1 - e^{t/\tau_{\text{rise}}}). \tag{5.14}$$

The rise time constant τ_{rise} corresponds to the laser pulse time profile. The generation function $B(t)$ can also be used to factor other processes such as a population increase due to product formation. The algorithm fitting optimization is implemented by Labview programs, and the sum of squares of the residuals is used to evaluate the quality of the fit. For a fitting function with a large number of parameters, the variation of the residuals due to a change in the value of one parameter can be compensated by adjusting the other parameters. When several exponential functions give very similar fitting results, the solution should go to the simplest one unless some prior knowledge exists to help eliminate those with the least physical meaning. In many cases we have some prior information about the system under study, therefore a target analysis can be applied by specifying the energy flow network model.[148] However, it is still problematic that for complex data with a large number of overlapped spectra, the best-fit model may not be unique.

Another method to determine the minimum number of components needed to model the system is singular value decomposition (SVD)[151], which explains the variation of the raw data on a completely model-free basis. Decomposition of the matrix **X** by using SVD can be written as:

$$\mathrm{SVD}\ (\mathbf{X})=\mathbf{USV}^{*} \tag{5.15}$$

where **U** and **V** are matrices of dimensions of $m \times m$ and $n \times n$, respectively. In the case of TA data considered here, each column of **U** can be seen as a spectrum, and each column of **V** can be seen as the trace associated with time. **S** is a $m \times n$ diagonal matrix and contains the singular values, which are arranged in descending order of magnitude. Generally, the largest singular values contain weight related to the physical signals, while the remaining values mainly contain noise. The number of components can be estimated from the first few singular values which are higher than noise-related values. SVD can also be used as a noise filter by eliminating the noise components. A noise-reduced matrix is obtained by reconstructing only the first few, strongest components. It should be reminded that individual SVD factors do not represent the physically relevant spectra but rather linear combinations of them. Generally, the dominant spectral component of **U** will be similar to the averaged TA spectrum and the other components show how the TA spectra evolves in time. Figure 5.10 shows an example of singular value decomposition analysis for a simulated data set which is based on a three-component parallel model (Figure 5.10 inset) with decay rate constants of 2, 1 and 0.2, respectively. The parallel model is commonly used to describe a molecular system, in which each species is independent of each other and depopulating in parallel. By SVD, the signal is captured in the 3 highest weighted components which is in accordance with the three-component model (Figure 5.10 (b)). The spectrum of the first component is very similar to the raw TA spectra as shown in Figure 5.10 (a).

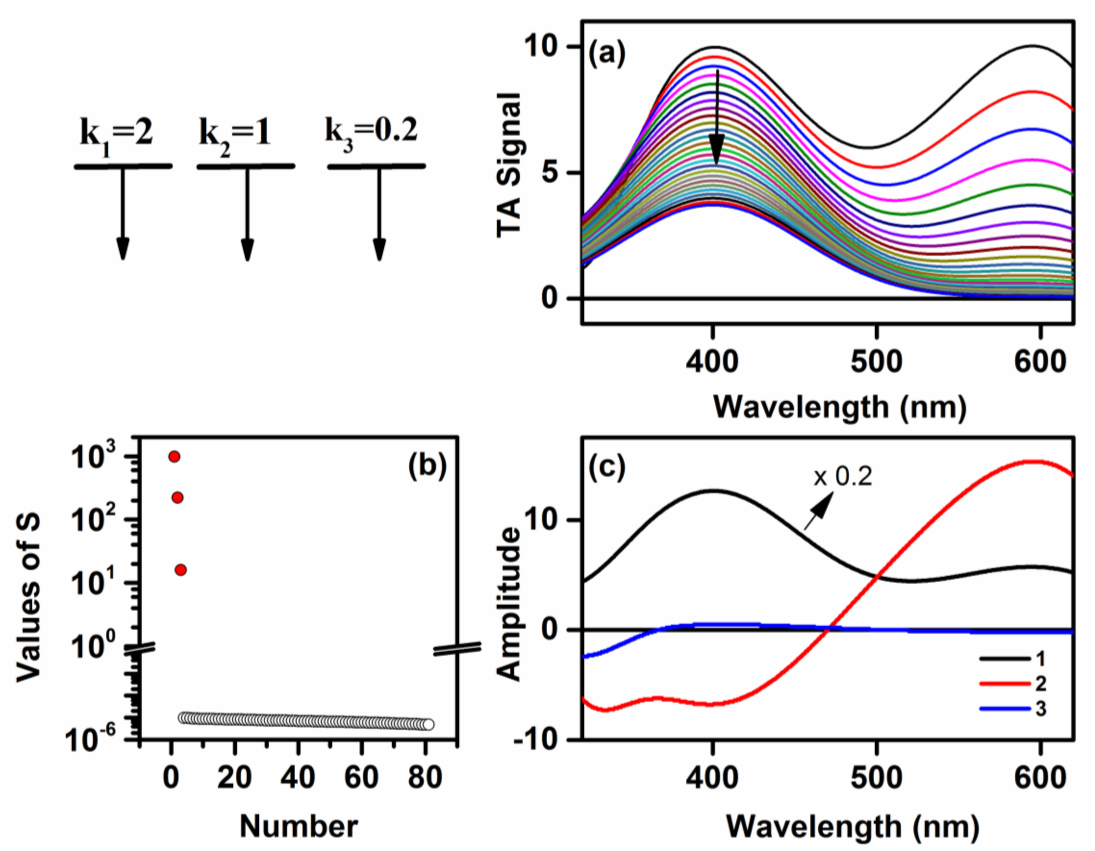

Figure 5.10: SVD analysis of simulated data. The model is a three-component parallel model, and each component has an individual decay rate. (a) Simulated TA spectra in the spectral range from 320 nm to 620 nm and time range from 10 fs to 4.95 ps. (b) Diagonal values of the **S** matrix. The three major components are marked as filled red circles. (c) First 3 spectral components of the **U** matrix.

Once the number of components and a reasonable understanding of the kinetics are obtained, the next step for a comprehensive data analysis would be to build a kinetic model for the whole chemical system under study. Global target analysis (GTA) is an extremely useful data analysis tool for the simultaneous analysis of multiple kinetic traces at different wavelengths with a particular target model.[152] The goal of GTA is to attempt to simplify the overwhelming amount of data into a small number of components. The global fitting algorithm of GTA is implemented using MATLAB (Ultrafast Spectroscopy Modelling Toolbox, Imperial College).[153] The measured TA data spectra is a superposition of the contributions from different components weighted by their respective time-dependent concentration, which can be expressed as:

$$\Delta OD(\lambda,t)=\sum_{i=1}^{n}c_i(t)\varepsilon_i\left(\lambda\right) \tag{5.16}$$

where $c_i\,(t)$ and $\varepsilon_i\,(\lambda)$ denote the concentration and spectrum of component i. Dependent on the chosen model, the time-dependent concentration is calculated by rate equations with the decay rates, and $\varepsilon_i\,(\lambda)$ corresponds to the molar absorptivity of the observable transient species. The first step to build a model with the assumed number of components, which can be obtained from SVD or exponential analysis, is to consider how the states are populated, and where population flows. Multiple possible models are tested, and the best-fit model is obtained with least residual and most physical meanings. Once the fitting algorithm is complete, we are left with the decay rates and the species associated spectrum (SAS) of each components.

To show the capability of GTA, an example is given using the simulated data introduced in Figure 5.10. The results of global analysis based on this model is shown in Figure 5.11. The SAS (Figure 5.11 (a)) corresponds to *difference* absorption spectra of three components. Note that the SAS of component 1 has a negative amplitude which is not observable in the TA spectra because component 1 is superimposed with component 2 and 3 which have positive amplitudes. From the concentration profile (Figure 5.11 (b)), rate constants of three components are obtained, which are in accordance with the rate parameters of the simulated data. In the global analysis, three species are disentangled. For a data set with a large number of spectrally overlapped components, several models can reproduce the experimental data with the same quality and thus identification of the best model sometimes will not be possible. Additional knowledge about the system being studied may help to judge the physical relevance of the calculated spectra and time constant. Moreover, multiple and complementary experiments, such as those performed in different molecular environments or at different probe regions can also help find a more precise description of the system.

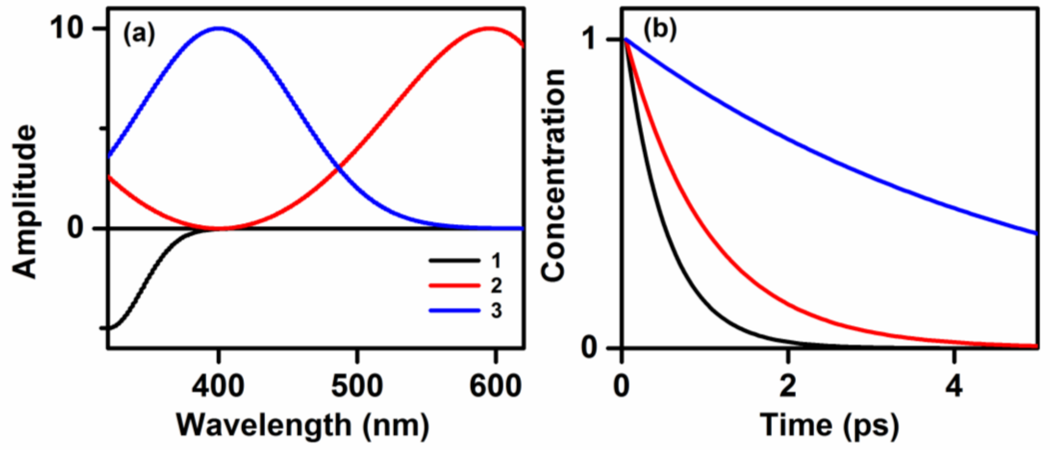

Figure 5.11: (a) SAS of the simulated data based on three-component model. (b) Concentration profile of the components (rate constants: $k_1=2$, $k_2=1$, $k_3=0.2$).

5.4 Study of 7-hydroxy coumarin in electronically excited state

The performance of the entire UV pump-probe system is tested in the study of the electronic levels and the dynamics in the excited state of 7-hydroxy coumarin. This molecule has been studied using time-resolved TA spectroscopy before, which makes it a good candidate to evaluate the experimental system in our laboratory.[154] 7-hydroxy coumarin is a substituted coumarin with a strong static absorption in the UV region (Figure 5.12), and high fluorescence efficiency.[155] The photochemical properties of 7-hydroxy coumarin in solution are significantly dependent on the polarity of the solvent.

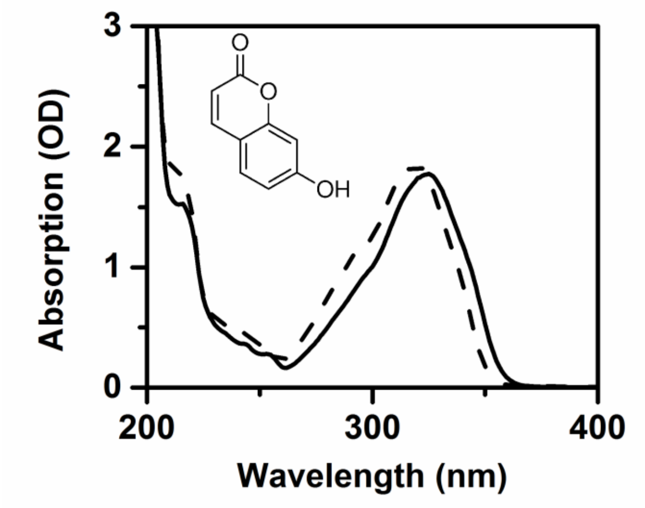

Figure 5.12: Static absorption of 7-hydroxy coumarin in ethonal (solid line) and acetonitrile (dashed line).

The sample was pumped at 327 nm and probed with a supercontinuum in the spectral range from 300 nm to 640 nm. The energy of the pump pulses were adjusted to be ~70 nJ. The shot-to-shot stability of the UV pump pulses was about 2.5 % (standard deviation of the average energy), and the stability of the probe pulses is given by the standard deviation of the intensity distribution divided by its root-mean-square value. The result of CaF_2 supercontinuum pumped under 800 nm is about 0.5 % around 330 nm. The experimental data were recorded by a PDA with 150 delay line positions and averaged over 300 laser shots with 20 scans. The duration of one experiment was about 1 hour and in such a short time the whole system can be assumed to be stable. The spectral resolution was about 0.5 nm in the UV region and 4 nm in the red edge of the spectrum. The sensitivity of the measurement was evaluated by the signal recorded after time zero. With 10 accumulated scans and 300 sampled points, an average sensitivity of about 5×10^{-5} OD over the whole detection window was obtained. By fitting a Gaussian and its two order derivatives to the coherent artifacts, the FWHM of the Gaussian was taken as the time resolution (Figure 5.13).[132]

Solutions of 7-hydroxy coumarin in different solvents (ethanol and acetonitrile) had an optical density, at the excitation wavelength (327 nm), of about 0.6 OD in a 350 μm optical flow cell. All solvents and coumarin were used without further purification.

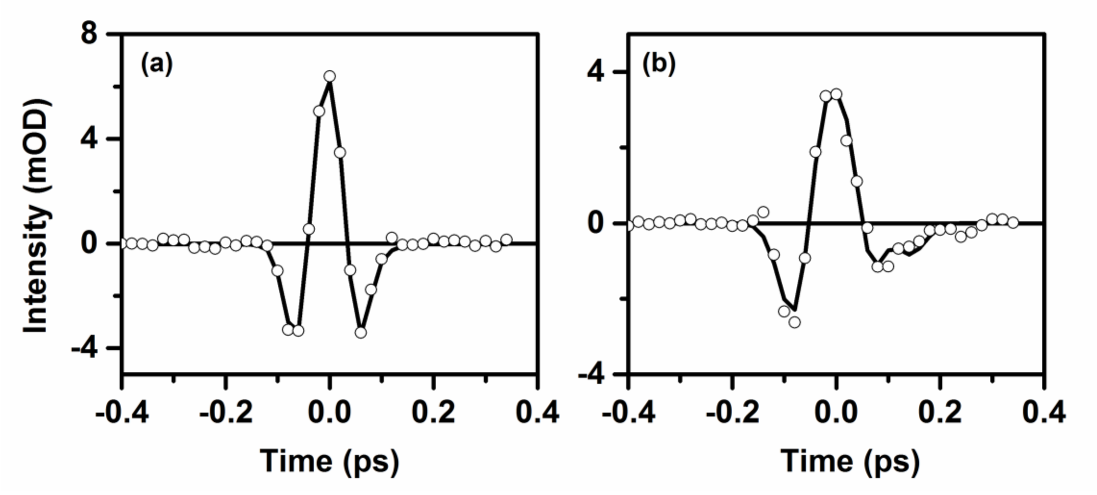

Figure 5.13: Fits of the coherent artifact (pumped under 327 nm and probed at 330 nm) in (a) ethanol and (b) acetonitrile, giving a time resolution of 60 fs and 72 fs, respectively.

TA spectra of 7-hydroxy coumarin in ethanol and acetonitrile are presented in Figure 5.14 and 5.15. The spectral structure in both solvents are similar. We observed two excited state absorption bands and one negative band. The first positive signal appears around 350 nm overlapping with the ground state bleach, and the second weak positive band covers almost the whole visible region (500-650 nm) of our detection window. The strong emission signal shows a maximum at 400 nm and extends up to 500 nm, which indicates the high fluorescence efficiency of 7-hydroxy coumarin. The main differences of the two solvents on the molecular dynamics can be explored by examining the kinetic traces at selected wavelengths, especially in the fluorescence related emission band. The selected kinetics traces differ significantly for well separated spectral regions. The excited state absorption band around 350 nm in ethanol shows a major decay component longer than 500 ps and a minor decay component with a time constant of 15 ps. The maximum of the stimulated emission at 400 nm is fitted with one rise time constant (7.8 ps) and two decay time constants (11.8 ps and 500 ps). The absorption band in acetonitrile around 350 nm shows a mono-exponential decay with a time constant of 35.7 ps, which is faster than in ethanol. The emission band in acetonitrile is shorter lived than in ethanol, and decays with two time constants of 4.6 ps and 32.8 ps. The long-time emission in ethanol indicates that the solvent with higher polarity leads to greater fluorescence emission in 7-hydroxy coumarin.

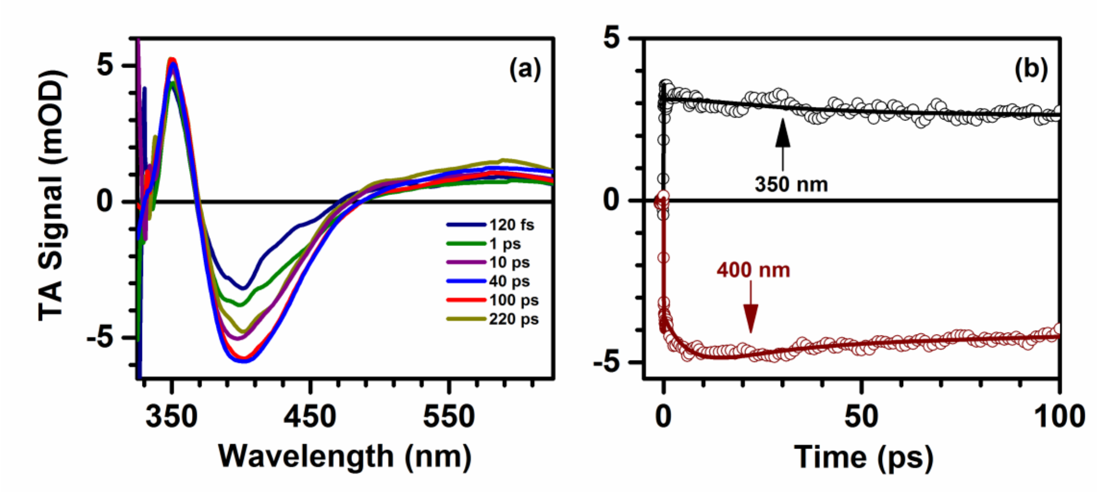

Figure 5.14: (a) Selected TA spectra of 7-hydroxy coumarin in *ethanol*, (b) TA traces and the corresponding kinetic fits at the maximum of absorption (350 nm) and emission (400 nm). The absorption band at 350 nm is fitted with two decay time constants (A: amplitude): τ_{dec1} = 15.0 ps (A_1 = 0.15), τ_{dec2} > 500 ps (A_2 = 0.85). For the kinetic trace at 400 nm, one rise time constant and two decay time constants are obtained: τ_{rise} = 7.8 ps (A = 1), τ_{dec1} = 11.8 ps (A_1 = 0.1), τ_{dec2} > 500 ps (A_2 = 0.9). For clarity, coherent artifacts have been fitted and subtracted.

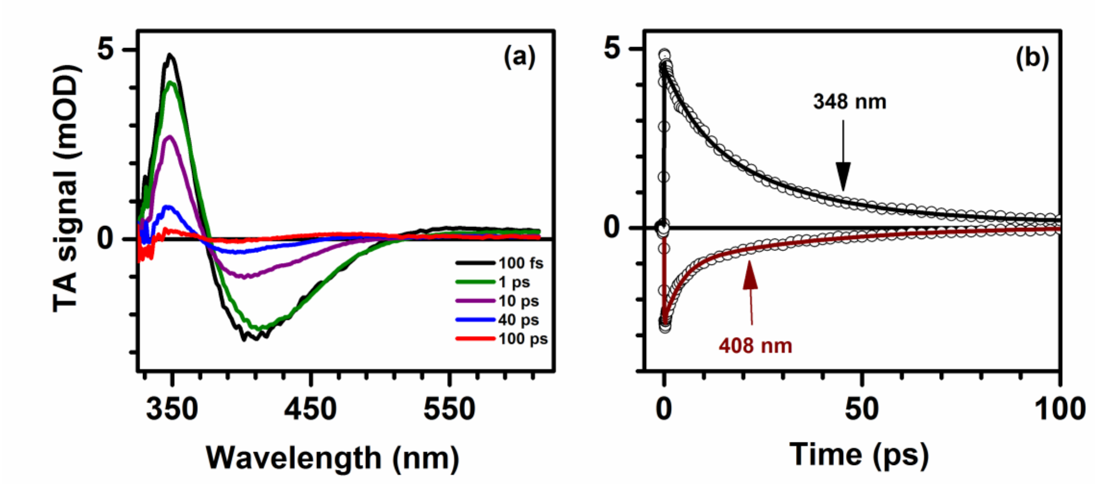

Figure 5.15: (a) Selected TA spectra of 7-hydroxy coumarin in *acetonitrile*, (b) TA traces and the corresponding kinetic fits at the maximum of the absorption (348 nm) and emission (408 nm) band. Decay time constant at 348 nm: τ_{dec} = 35.7 ps. Decay time constants at 408 nm: $\tau_{\mathrm{dec}1}$ = 4.6 ps (A_1 = 0.54), τ_{dec1} = 32.8 ps (A_1 = 0.46). For clarity, coherent artifacts have been fitted and subtracted.

To unravel the processes underlying the observable spectroscopic changes, a GTA was applied. The dynamics of 7-hydroxy-coumarin in both solvents can be very well described by a branched parallel model shown in Figure 5.16. This model is corroborated by an initial decomposition of the experimental data by SVD which shows four major components. Both positive absorption and negative emission signals are well fitted. The results of the GTA (Figure 5.17) are explained in the following way. After excitation into the Franck-Condon region, component A is populated and from this state parallel relaxation pathways along the components B and C start off. There is almost no emission from component B, while component C shows a strong emission contribution. The above processes can be interpreted as, the excited state population can relax in two different pathways after the optical excitation into the $\pi\pi^*$ state.[154] One relaxation takes place along the carbonyl stretching mode into the dark $n\pi^*$ state and the other one along the bright $\pi\pi^*$ state into the S_1 minimum. From the S_1 minimum it goes back to ground state or relaxes by fluorescence. In ethanol the relaxation rates for the two pathways are similar, while in acetonitrile the relaxation rates change dramatically and component B is more populated.

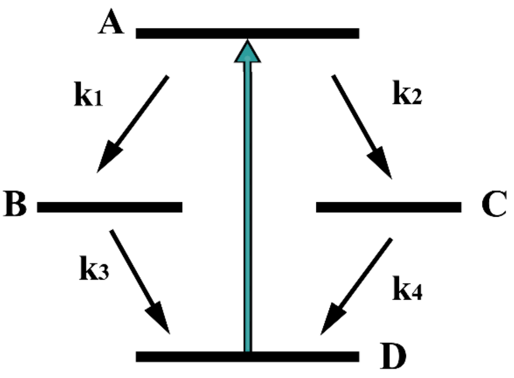

Figure 5.16: Relaxation model used in the GTA. k_1-k_4 are rate constants for the respective decays.

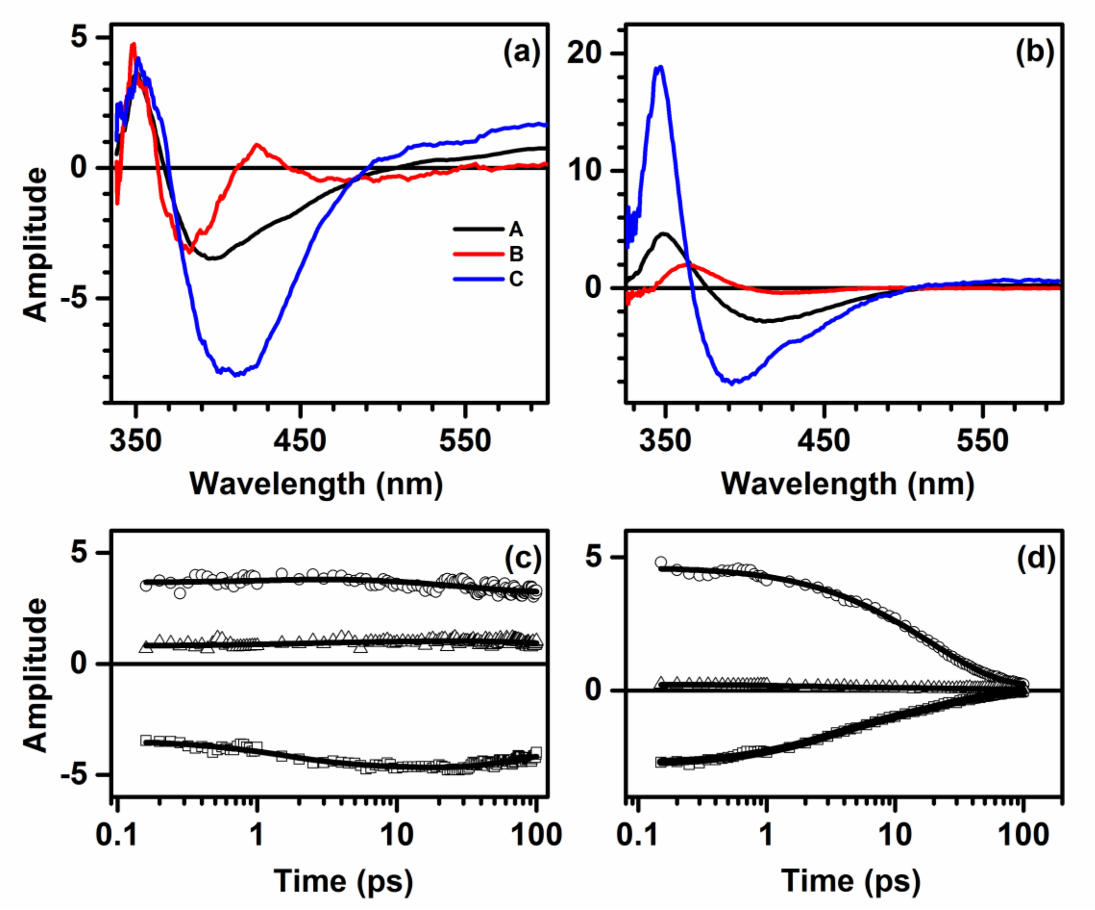

Figure 5.17: Global target analysis results for 7-hydroxy coumarin: SAS for measurements in (a) *ethanol* and (b) *acetonitrile*; selected TA traces for measurements in (c) *ethanol* and (d) *acetonitrile*, open points are experimental data, lines are global target fits. Time constants for ethanol: t_1 = 0.9 ps, t_2 = 1.1 ps, t_3 = 7.7 ps, t_4 = 37.0 ps, and for acetonitrile: t_1 = 3.0 ps, t_2 = 15.6 ps, t_3 = 7.8 ps, t_4 = 25.7 ps. (t_1- t_4 represent the decay times A→B, A→C, B→D and C→D, respectively)

From the experimental results and global analysis, the interaction between the electronics states and the solvent is observed as the dynamics differ in ethanol and acetonitrile. As suggested in Ref [154], the influence of solvent polarity is on the position of the conical intersection, which determines the branching ratio between the two pathways. The $n\pi^*$ state is more affected by the polarity of the solvent than the $\pi\pi^*$ state. The energy positive of the $n\pi^*$ state is up-shifted in polar solvents, which leads to the conical intersection moving close to the Franck-Condon region. Ethanol is more polar than acetonitrile, so the shifted conical intersection leads more transition from the initial $\pi\pi^*$ state to the $n\pi^*$ state, which explains the different branching ratio in ethanol (~1:1) and acetonitrile (~1:5).

The experimental data of 7-hydroxy coumarin in ethanol and acetonitrile obtained with the TA setup constructed in our laboratory very closely resemble those reported in Ref [154], which verifies quantitatively the performance of our experimental setup is sufficient and reliable. However some quantitative differences, such as the different signal amplitude, longer time constants in our case, are unavoidable because of the high sensitivity of the TA signal to spatial overlap between the pump and the probe, pump intensity as well as detection system, which is intrinsic to TA pump-probe measurements. The instrument characteristics and procedures of data analysis also could affect the results.

5.5 Conclusion

A newly designed UV transient absorption system is fully described. The setup has been put together under full consideration of all optical and technical components, which are necessary and essential to perform pump-probe measurements in the spectral domain of UV. The needs of good time resolution can be met by the ultrashort pump pulse together with the right choice of the sample cell. The performance of our setup is summarized in Table 5.1. In addition, a data processing and analysis procedure is established, which is specifically developed for ultrafast UV spectroscopy. The coherent artifact signal generated during TA measurements is discussed and a correction procedure is developed based on the XPM function. The study of 7-hydroxy coumarin in ethanol and acetonitrile was carried out to test the performance of the experimental system. The study was aimed to investigate the electronic states of 7-hydroxy coumarin and the solvent effects on the dynamics. The obtained TA data is in agreement with the reported results [154].

Table 5.1 The performance of the setup

Pump range	250-350 nm
Probe range	240-750 nm
Time resolution	~ 60 fs
Spectral resolution	0.5-4 nm
Sensitivity	5×10^{-5} OD
Comments	The whole system is stable and able to perform measurements for weeks continuingly without massive adjustment

Chapter 6

UV Transient Absorption Study of Coumarin Dimers

The photo-induced cleavage of a coumarin dimer into its two monomers is a promising mechanism for laser controlled medical applications. In this chapter, we focus chiefly on the dynamics of excited states of coumarin dimer and the mechanism of cleavage reaction in order to develop strategies for increasing the reaction efficiency. The unsubstituted coumarin dimers in three isomers: anti-head-to-head (anti-hh), syn-head-to-head (syn-hh) and syn-head-to-tail (syn-ht) are studied by UV transient absorption spectroscopy. This chapter starts with an introduction of up-to-date investigations of coumarin dimers. In the following, time-resolved experiments are performed and the experimental results of coumarin dimers are presented. From the data, two branched kinetic models are developed to describe the formation of monomers and dimer relaxation dynamics, to identify possible intermediate states, and to determine the quantum yields of the dimer splitting. Subsequently, a complementary information of coumarin monomer is given to gain a better understanding of cleavage mechanism of dimers. At the end, the differences in cleavage efficiency for the three dimer isomers are discussed.

6.1 Introduction

There have been various experimental and theoretical studies of coumarin photochemistry. Recently, UV pump (330 nm) transient absorption spectroscopy of coumarin and umbelliferone monomers permitted the study of the excited states photodynamics and deactivation channels.[154] The results indicated that after a vertical excitation to the $\pi\pi^*$ excited state two parallel branching pathways can take place: (1) through the dark $n\pi^*$ state back to the ground state in a few picoseconds or (2) relaxation along the bright $\pi\pi^*$ state which induces an opening of the coumarin π system. Furthermore, the ring opened coumarin was found to reform its closed structure in about 20 ps. This result was also confirmed by an investigation of coumarin and a related heterocyclic molecule, α-pyrone, by using transient vibrational absorption spectroscopy.[156] Following excitation at 310 nm, α-pyrone rapidly decays back to the closed form with 68% efficiency. In contrast, coumarin reforms its closed form with near 100% quantum yield under 330 nm excitation. An additional relaxation mechanism in the excited state of coumarin is the formation of triplet states. However, the properties of the triplet state have not been fully characterized, as it is still not clear from which singlet state the triplet manifold is populated.[154]

While the ultrafast relaxation dynamics of coumarin monomers seem to be well understood, the ultrafast dynamics of coumarin dimers is still not clarified. Theoretical investigations by Seifert et al. calculated the photoexcitation spectra of coumarin dimers and derivatives in the gas phase, which suggested similar response spectra at low energies for the anti-hh, syn-hh and syn-ht dimer.[157] Ab initio calculations of the ground and first excited states, combined with frontier orbital analysis provided some explanations of possible dimerisation products.[158] However, theoretical studies regarding the excited state dynamics of coumarin dimers and the cleavage reaction have not been conducted yet. There have been experimental approaches carried out regarding the time-independent properties of the photo-cleavage reaction. Three different types of cleavage mode for the coumarin dimers: symmetric, asymmetric and competitive, were observed under direct UV irradiation around 277 nm. On the basis of experimental results, it was concluded that the chemical structure of the coumarin dimers determines the cleavage mode for the cyclobutane ring.[22, 159] The cleavage reaction was also studied by UV-VIS and IR spectroscopy upon direct excitation at 254 nm in the absence and presence of triplet-state sensitizers.[160] The results of the study proposed the photocleavage occurs via a non-fluorescent short-lived singlet state with a splitting efficiency of around 0.2. This was further confirmed by two photon absorption experiments, which showed about 20 % efficiency for the cleavage reaction.[161, 162] Additionally, it was discovered that addition of substituents to the coumarin dimer can improve the cleavage reaction efficiency. However, it is still not clear how the substituents modify the cleavage dynamics, or how it generally leads to enhanced efficiencies compared to the unsubstituted coumarin dimer.

Due to the cleavage of two C-C bonds in the cyclobutane ring when the monomer products are formed, the photoreversions of cyclobutane-based compounds have often been explained in the framework of a pericyclic reaction (Figure 6.1 (a)) governed by the Woodward-Hoffmann rules.[163] For photochemical pericyclic reactions, a general feature is the pericyclic minimum on a two-electron excited state of the reactant, which collects population from any initially excited state transferring it to the ground state of product and reactant, respectively.[23] Fuß *et al.* have performed several time-resolved laser ionization measurements of pericyclic reactions in cyclohepta-1,3-diene and cycloocta1,3-diene, which indicated the depopulation time of the initial excited state into the two-electron excited state is under 100 fs.[24, 164] According to the Woodward-Hoffmann rule, the cleavage reaction proceeds in one step without any intermediate state, which means the two C-C bonds of cyclobutane ring are split simultaneously. However, some studies concerning the photocycloreversion of the cyclobutane ring have provided indication of an intermediate state (Figure 6.1 (b)).[165, 166] Zewail *et al.* observed the tetramethylene diradical intermediate state, and monitored its formation and decay dynamics using time-of-flight mass spectrometry.[4] The experimental data showed the diradical is formed in about 150 fs and decays in about 700 fs to form a cyclobutane ring and two ethylene molecules. However, a key question as to whether the cleavage reaction of the cyclobutane ring is concerted or a two-step, successive process is still not clearly addressed.

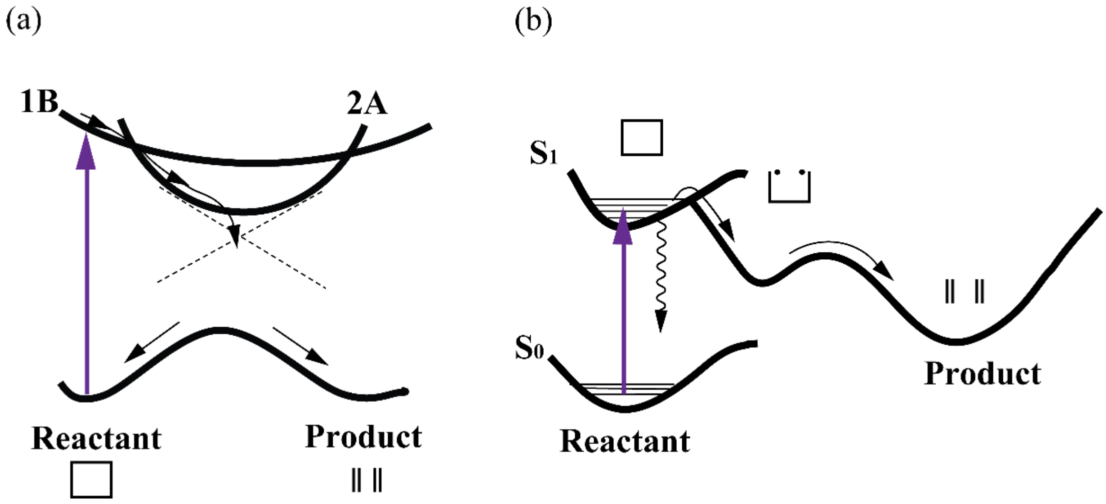

Figure 6.1: (a) Schematic energy curves for photo-induced pericyclic reaction: after vertical excitation, population flows into the pericyclic minimum on a two-electron excited state of the reactant, which collects population from any initially excited state transferring it to the ground state of the product and reactant, respectively. (b) Schematic energy curves for the cleavage reaction based on a two-step mechanism: beginning with the breakage of one σ-bond to form a diradical intermediate which in turn passes through a transition state to form the final product.

6.2 Experiment parameters

Our transient absorption setup was based on a tunable femtosecond UV pump source and a broadband supercontinuum for the wavelength selective probing. The pump pulses were generated from SHG NOPA with a tunable range from 250 nm to 300 nm. For excitation of the dimers, the pump wavelength was tuned to 280 nm or 270 nm. The pulse duration was less than 30 fs and energies up to 100 nJ. A single filament supercontinuum generated in CaF_2 plate served as the probe light spanning most of the visible range and extends to UV around 300 nm. The spectrally resolved intensity of each laser shot was recorded by the multichannel photodiode array. The time resolution of the measurements was about 60 fs, as estimated by Gaussian fitting of the observed cross-correlation signals between the pump and probe pulses. All measurements were carried out at the magic angle (54.7°) between pump and probe polarizations.

All dimer molecules were synthesized in a modified procedure following Ref [167]. The static absorption spectra of anti-hh, syn-hh and syn-ht dimers are shown in Figure 6.2. Samples (coumarin monomer and dimers) were used without further purification and diluted in acetonitrile in a 350 μm quartz windowed optical flow cell. The optical density of three dimer isomers was adjusted to be nearly the same value of about 0.3 OD at the corresponding pump wavelength.

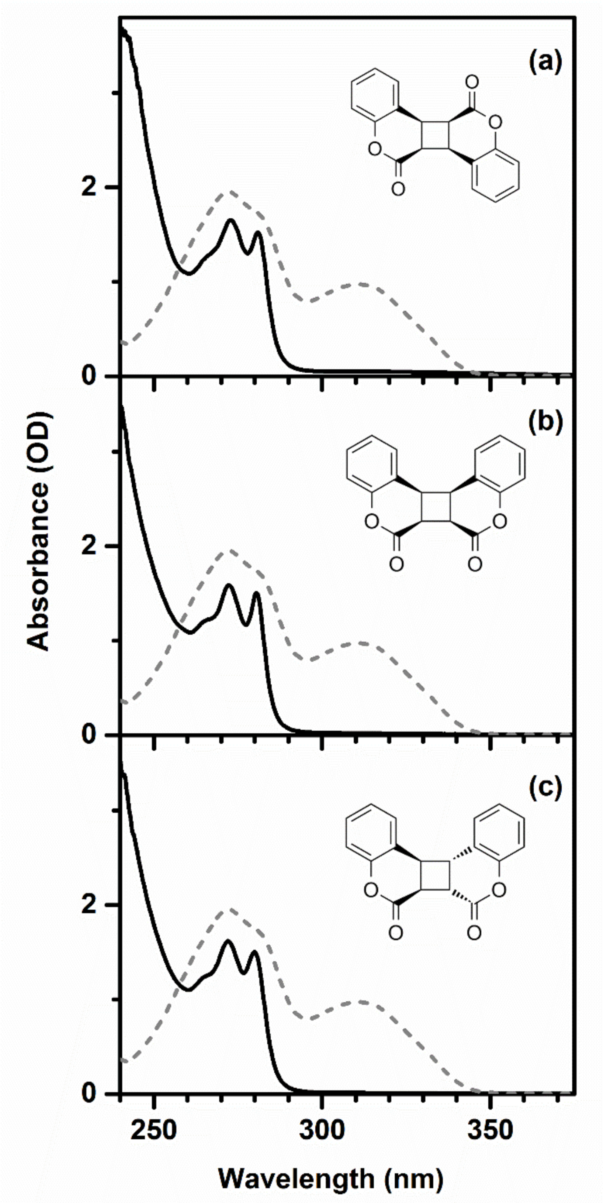

Figure 6.2: Static absorption spectra of coumarin dimers (solid line) and the respective monomer (dashed line) in acetonitrile. (a) syn-ht, the absorption peaks λ_{Abs_Peak} are at 272.8 nm and 280.8 nm, (b) syn-hh, λ_{Abs_Peak}= 272.2 nm, 280.4 nm, (c) anti-hh, λ_{Abs_Peak}= 272.0 nm, 280.0 nm.

6.3 Results

6.3.1 Transient absorption data

Figure 6.3 shows the transient absorption data obtained by pumping syn-ht, syn-hh and anti-hh dimers at 280 nm in acetonitrile. All coumarin dimer isomers were measured under the same experimental conditions. In comparing the TA spectra of three dimers, one can see similar characteristics and trends. The difference absorbance values evolve over the pump-probe delay time. A dominant positive signal spans almost the whole detection window from 310 nm to 650 nm showing an almost flat plateau with no observable simulated emission signal. Nevertheless, upon closer inspection several dynamics features can be seen. The excited state absorption in the blue region shifts from 375 nm to 325 nm and narrows with a time scale of about 30 ps, showing similar dynamics as the coumarin monomer.[154] As the delay time increases, the intensity of the positive signal continues to decay. In the time range between 80 fs and 1 ps, the transient signal of all wavelength components exhibits almost the same decay indicating a fast depopulation of excited states, with absorption covering almost all the detectable spectral range. After 4 ps, one peak around 330 nm is clearly identifiable, which shifts to 325 nm and remains unchanged up to a pump/probe delay time of 700 ps. Different from 325 nm, a red-shifted signal around 340 nm shows a complete decay to the baseline in a time scale of 30 ps. After 30 ps seconds there is no appreciable spectral variation across all wavelengths.

More interesting to note is the differences between the three dimers. At early times, the anti-hh dimer (Figure 6.3 (c)) features a stronger absorption than the other two dimers. After 4 ps, a broad absorption structure extending from 400 nm to 560 nm remains for both anti-hh and syn-hh dimers (Figure 6.3 (b)). This contribution has a weak but detectable amplitude of about 1-2 % in this spectral region. The absorption band at 325 nm in long time measurements shows slightly different amplitude for three dimers. The anti-hh dimer displays more intensity at 325 nm compared to the other two dimers. The most striking spectral difference is that the syn-ht dimer (Figure 6.3 (a)) has a well-resolved absorption band around 540 nm which could possibly be evidence of another photoproduct formation concomitant to photocleavage,[160] since coumarin monomers on the ground state don’t have absorption at this wavelength region (Figure 6.2). To identify this signal, an additional irradiation study on the syn-ht dimer was performed and its absorption difference was monitored by using UV/VIS absorption spectroscopy. After 3 hours of UV lamp irradiation at 252 nm, the absorption spectrum of the syn-ht dimer shows only an increase of absorbance at λ_{max}=310 nm and no absorption is observed around 540 nm (Figure 6.4), which is consistent with literature data.[167] Furthermore, a long time transient absorption measurement of up to 700 ps of syn-ht dimers shows a very slow decay behaviour around 540 nm (Figure 6.5). From this empirical analysis it seems the 540 nm signal is likely a very weakly absorbing excited state, which for reasons that remain unknown is more prominent in the syn-ht isomer.

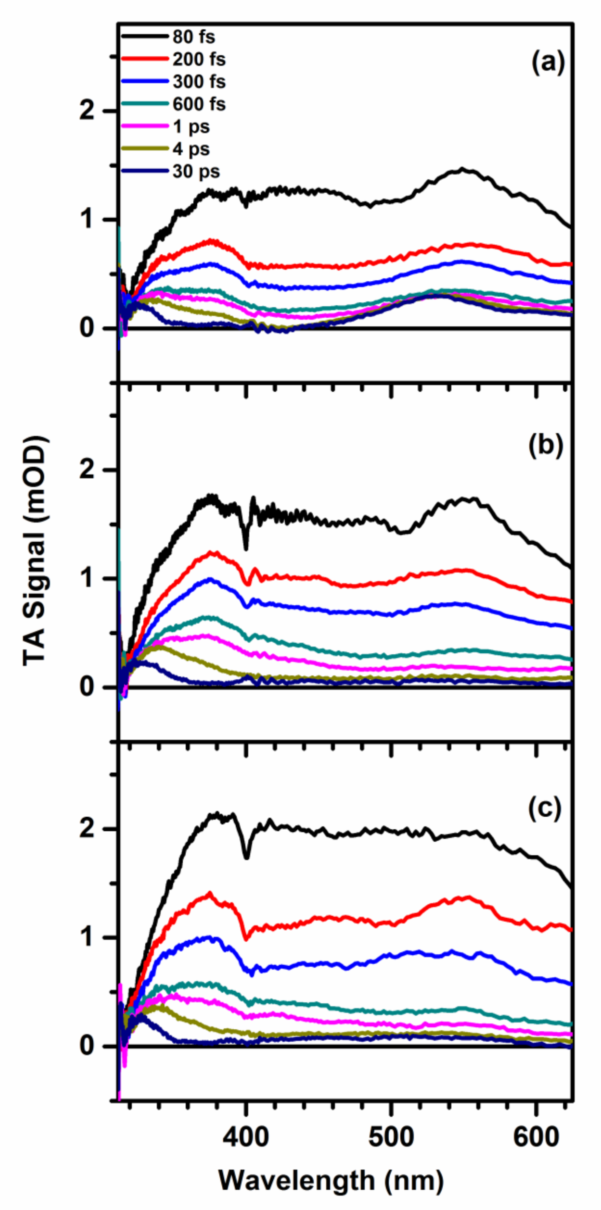

Figure 6.3: Selected transient spectra for (a) syn-ht, (b) syn-hh and (c) anti-hh dimer, following excitation at 280 nm. The small dip at about 400nm in all measurements is due to a malfunction of the detection system at this wavelength.

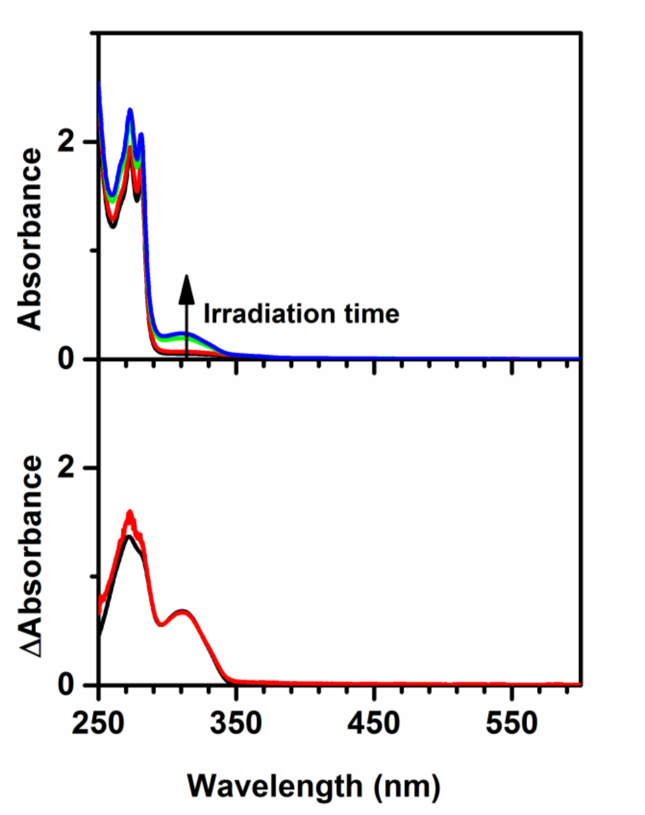

Figure 6.4: Direct irradiation of the syn-ht dimer by UV lamp at 252 nm: (a) absorption change upon irradiation time, (b) absorption difference after 3 hours irradiation time (red) and the static absorption of coumarin monomers (black).

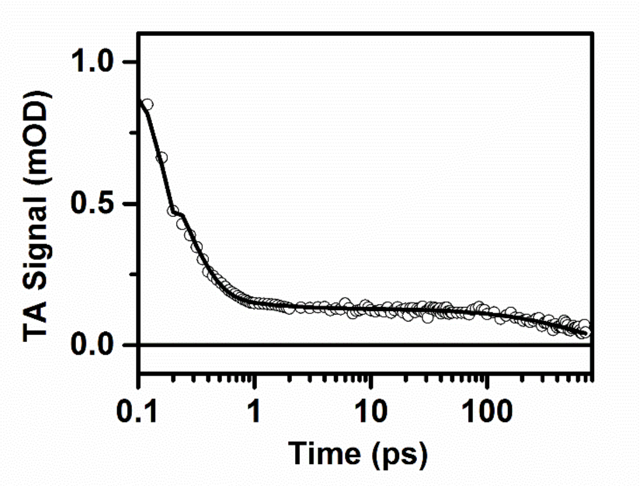

Figure 6.5: Transient absorption trace of the syn-ht dimer at 540 nm (empty circle) with the fitting trace (solid line). Three exponential contributions are obtained: t_1 =150 fs, t_2 =1.4 ps and t_3 = 600 ps.

6.3.2 Kinetic analysis

The features and differences of the three dimers can be observed more clearly by examining the kinetic data at selected wavelengths. Figure 6.6 depicts selected kinetics for the three dimers, which demonstrates a rich variety of population dynamics at early delay times (< 2 ps). In general, the signal measured at different probe wavelengths consists of three time constants (Table 6.1): an initial fast component (< 1 ps) with a high amplitude followed by a minor slower decay with a time constants of a few picoseconds. In addition, the much longer lived positive signals at 325 nm and 540 nm are fitted with nanoseconds time constants. As the three dimers have different isomeric structure, it is reasonable to expect different behaviours before the cleavage takes place. For the anti-hh dimer at 325 nm, we used a bi-exponential function revealing a time constant of 200 fs for the relaxation of the dimer excited states. A minor component with ~ 27% amplitude and a nanosecond lifetime suggests that a sizable fraction of the initially excited coumarin dimers evolved to form monomer photoproducts. At 340 nm, no long lived absorption can be observed. The signal is dominated by a major decay with a time constant of about 220 fs. A minor contribution with a time constant of about 33 ps is also observed, which is similar to the relaxation dynamics of coumarin monomers via lactone ring opening.[154] The absorption band at 540 nm, which is far away from the ground state absorption band of the coumarin monomer, shows a major decay component with a time constant of about 160 fs, and a minor decay component with a slower decay constant of about 1.5 ps.

Table 6.1 Decay time constants and normalized amplitudes at selected wavelengths

Molecule	λ (nm)	A1	t1/ps	A2	t2/ps	A3	t3/ps
anti-hh	325	0.73	0.20	0.27	>ns	/	/
	340	0.82	0.22	0.18	33	/	/
	540	0.95	0.16	0.03	1.5	0.02	>ns
syn-hh	325	0.77	0.17	0.23	>ns	/	/
	340	0.73	0.24	0.27	31	/	/
	540	0.94	0.16	0.06	1.5	0.01	>ns
syn-ht	325	0.87	0.10	0.13	>ns	/	/
	340	0.81	0.18	0.19	30	/	/
	540	0.92	0.13	0.02	1.7	0.07	>ns

Syn-hh dimer is very similar to anti-hh dimer with only a slightly faster decay at 325 nm (170 fs) and slower decay at 340 nm (240 fs). It is interesting to note that the syn-ht dimer exhibits identifiable features not only in the transient absorption spectra, but also in the dynamics. The syn-ht dimer has the fastest initial dynamics of the three isomers with more than 80 % of the initially excited population relaxing in less than 200 fs.

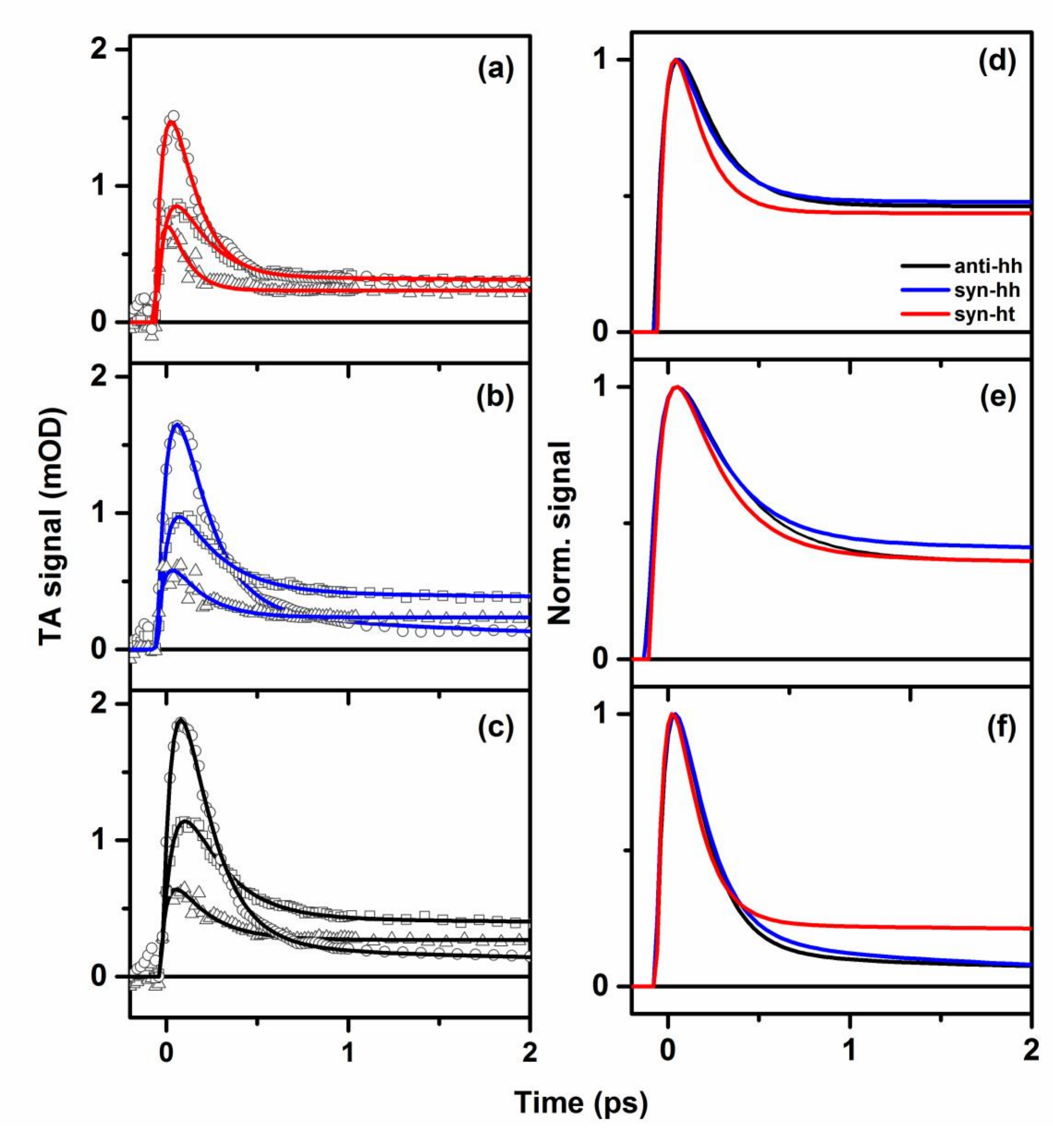

Figure 6.6: Transient absorption traces of the three dimers (a) syn-ht, (b) syn-hh and (c) anti-hh with corresponding fits at 325 nm (empty triangle), 340 nm (empty square) and 540 nm (empty cirlce). Kinetics comparison of the three isomers for the probing wavelengths at (d) 325 nm, (e) 340 nm and (f) 540 nm. For clarity the coherent artefact has been subtracted, and the comparison of kinetics are performed by the normalized fits.

6.3.3 Quantum yield

The efficiency of the single photon induced cleavage is characterized by the quantum yield Φ, which is defined as the ratio of the number monomers N_M formed divided by two (since one cleaved dimer molecule leads to the formation of two monomer molecules) and the number of excited dimer molecules N_D:

$$\Phi = \frac{N_M}{2N_D} \tag{6.1}$$

Since the TA absorption band of coumarin dimers around 325 nm, at very long delay times, matches perfectly the linear absorption of monomers in the ground state (see Figure 6.7), the number of produced monomers can be directly calculated according to the Lambert-Beer law. The number of excited dimers N_D is not directly available from the TA signal, since no ground state bleach of the dimers is detectable in our experiment. It can be calculated though by the number of absorbed pump pulse photons. By using the molar absorption coefficients of three dimers in acetonitrile at 280 nm ($\varepsilon_{\text{anti-hh}}$=2647, $\varepsilon_{\text{syn-hh}}$=2324 and $\varepsilon_{\text{syn-ht}}$=2888 $\text{L*mol}^{-1}\text{cm}^{-1}$) and the solution's optical density, the number of absorbed photons can be easily calculated. Moreover, since the experiments for all three isomers were performed under the same experimental conditions, the quantum yields can be expressed as a normalized relative quantum yield and experimental parameters like absolute pump pulse fluence, excitation and probe beam areas are not required. By assuming a quantum yield of 20% for the single photon induced cleavage of the anti-hh dimer coumarin,[167] quantum yields of the other two dimers can be obtained (Table 6.2).The quantum yield of syn-ht dimers calculated this way matches very well the value (15 %) obtained in static irradiation experiments by other groups[160], hence supporting the methods validity.

Table 6.2 Quantum yield (QY) of coumarin dimers

Molecule	Normalized QY	QY %	Error
Anti-hh	1	20.0	±1.0
Syn-hh	0.855	17.1	±1.2
Syn-ht	0.755	15.1	±1.2

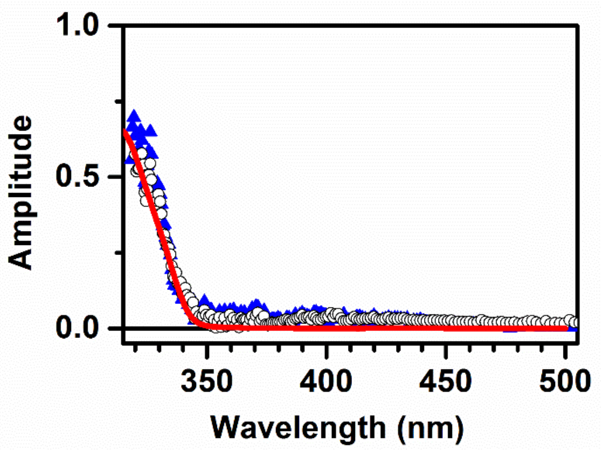

Fig. 6.7: Static absorption of coumarin monomer (res line), TA signal of anti-hh dimers after 100 ps (solid blue triangle), and the species associated spectra (SAS) of the last species in the global target analysis of anti-hh dimers (empty black circle).

6.4 Discussion

The profoundly similar static absorption spectra for the three dimers is expected as each dimer contains the same pair of isoelectric, yet electrically decoupled π-conjugated rings. Electronic interaction between the two π-systems is prohibited by the bridging four-membered ring. All three dimers have similar Franck-Condon state absorption (Figure 6.2) under 280 nm pumping, which is associated with the HOMO-LUMO transition.[157] This indicates that a relatively small geometry change accompanies the $S_0 \rightarrow S_1$ transition. The fast 200 fs decay component (Figure 6.6) can be contributed to the relaxation of the low excited electronic state of the dimers. The absence of any negative signal (Figure 6.3) suggests the low excitation state of the coumarin dimer is a non-fluorescent, short-lived singlet state which corresponds to the previous report concerning the cleavage mechanism of coumarin dimers.[160] The very distinctive absorption band of the syn-ht dimer around 540 nm more likely arises from a slowly decayed singlet state, instead of a triplet state, because the absorption bands of the lowest excited triplet state of coumarin monomers have been identified in the region between 400 and 450 nm and with a decay time of 300-500 ns.[168, 169] Dimer molecules contain the pair of isoelectric, yet electrically decoupled π-conjugated rings. The coumarin dimer π-conjugation is even more restricted to the phenyl rings than the monomer system. Electric interaction between the two π-system is prohibited by the bridging four-membered ring, thus the triplet transition of dimers within the π-system is not expected to be 4000 cm^{-1} shifted compared to the parent monomer molecule. However, triplet sensitisation experiments or alternative techniques, such as electron paramagnetic resonance, would be required to test for contribution from a coumarin dimers triplet state.

It is expected that the transient spectra at detection wavelengths below 325nm resembles the absorption spectra of the monomer product at very long probe delays. The spectra for delays larger than 30ps match well indeed with the ground state absorption spectrum of the monomer (Figure 6.7). Nevertheless, the lack of any variation in the kinetic traces at these wavelengths (e.g. at 325nm) after about 500 fs provides little insight on when exactly the ground state of the monomer is formed. As illustrated in Figure 6.8, the kinetics at 325nm can be described by a kinetic model where the monomer is formed initially in the excited state, decaying via an intermediate state and finally to the ground state of the monomer. Alternatively, the same kinetics can be equally well described by a kinetic model where the monomer ground state is formed directly from the excited state of the dimer without any intermediate. In the model with an intermediate state, the ground state of the monomer is predicted to form within about 20 ps, whilst in the kinetic model without an intermediate state the ground state of the monomer is formed much quicker within 300 fs. As explained in chapter 5, the unambiguous modelling of the monomer formation derives from the strong spectral overlapping of different states in these spectral region. This makes it very challenging to identify the underlying kinetic model by using only the blue shifted probe wavelengths in the analysis. To assist in distinguishing whether an intermediate state is involved or not, examination of the transient spectra at other detection wavelengths is required. In the next part, we will discuss the possible mechanisms for the cleavage reaction by applying global target analysis (GTA) in order to give a more-detailed picture about the evolution of monomer formation.

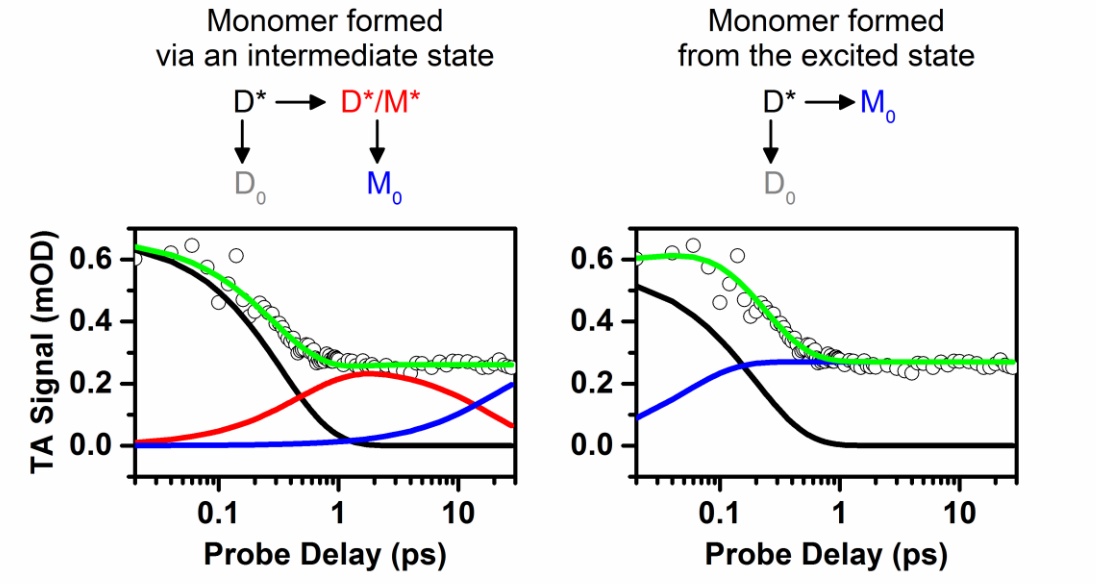

Figure 6.8: Schemes for the kinetic models for the formation of coumarin monomer. The green line is the sum of all contributions in each model: black represents the population in the excited state of the dimer, while blue describes the ground state of the monomer. The red trace represents an intermediate state between the excited dimer and ground state of the monomer.

6.4.1 Global target analysis

Theoretical and experimental findings, in particular the photocleavage quantum yields (~ 20%) of coumarin dimers, suggest there must be at least one competing relaxation pathway that opposes the dimer ring opening.[24, 161, 170] From the data obtained, the most likely competing process is fast non-radiative decay back to the ground state of coumarin dimers. Initial decomposition of the experimental data by singular value decomposition (SVD) shows four major components for all three isomers. Therefore, a global target analysis was carried out for the experimental data sets with two models both comprising 5 levels (A-E) and 4 rate constants (Figure 6.9). Other kinetics models involving fewer species or less channels were also tested but either could not fit the experimental data, produced unrealistic dynamics or spectra.

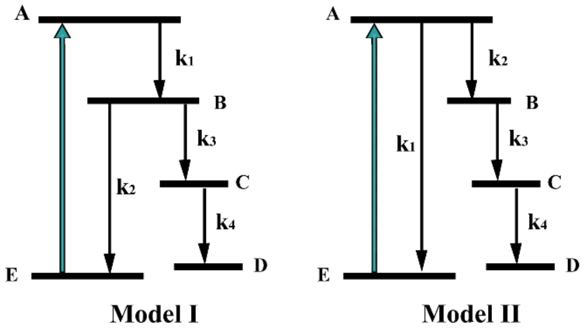

Figure 6.9: Relaxation models used in the global target analysis. k_1-k_4 are rate constants for the respective decays.

In this section, a GTA for the anti-hh dimer is presented. Species associated spectra (SAS) and dynamics fittings of the anti-hh dimer at selected wavelengths are shown in Figure 6.10, and the obtained decay constants are summarized in Table 6.3. Results for the other two isomers are similar, so the SAS will not be shown here (see Appendix) and the obtained decay constants are given in Table 6.3. In this analysis, the coherent artefacts from the solvent and flowing-cell window have been fitted and subtracted. The set of SAS and time constants acquired result in a very good fit of the anti-hh dimer over the whole data range. Both target models give the same residuals and quality of fit to the experimental data.

Table 6.3 Time constants of dimers obtained by GTA

Molecule	Model	τ_1 (ps)	τ_2 (ps)	τ_3 (ps)	τ_4 (ps)	Residual
Anti-hh	I	0.16	1.01	4.04	19.06	20.17
	II	0.21	0.71	0.81	19.00	20.17
Syn-hh	I	0.19	1.50	6.95	19.20	47.96
	II	0.23	0.98	1.23	19.20	47.96
Syn-ht	I	0.14	1.33	7.40	23.00	15.17
	II	0.16	0.94	1.12	23.00	15.16

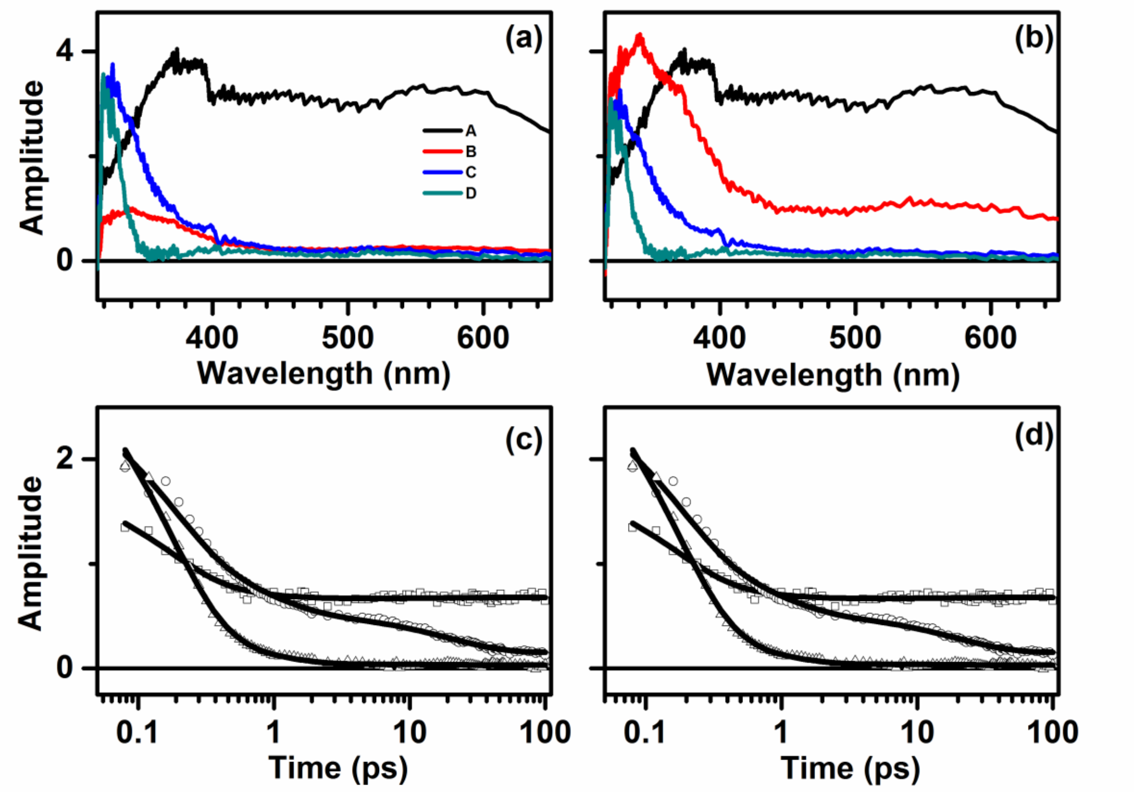

Fig. 6.10: Global target analysis results of the anti-hh dimer: SAS obtained for (a) model I and (b) model II, transient absorption traces for (c) model I and (d) model II. Open points are experimental data, solid lines are global target fittings.

Model I is based on one sequential decay A → B, followed by a branching from B to E and C. A similar model has been used to describe the kinetics of Flavin-Thymine dimers.[7] The SAS of the GTA results depicts a broad absorption (Figure 6.10 (a)) with a decay shorter than 160 fs showing a major loss of excited state absorption, similar to that seen in the kinetic fitting of the raw data (Table 6.1). The branching starts from the second species B, and the fitted time constants reveal two time constants for B → E and B → C of about 1 ps and 4 ps, respectively. Note, the quantum yield calculated from these two time constants matches the experimentally measured quantum yield of 20 %. There is a large difference in shape between species A and species B, which may indicate the overlap between absorption of different states or simply indicate that species A and B originate from different electronic states.[152] Comparatively, species B has a relatively flat absorption with lower amplitude, which decays with a time constant of ~ 800 fs ($1/(\tau_2^{-1} + \tau_3^{-1})$). After branching, two species C and D, which have similar absorption, display two sequential decays with lifetimes of 4 ps and 19 ps, respectively. Additionally, species D resembles the static absorption of the coumarin monomer (Figure 6.7).

Instead of starting with a sequential channel, model II begins directly with branching pathways A → E and A → B with time constants 210 fs and 710 fs, respectively. The quantum yield from the calculation of branching rate constants is about 22.8 %, similar to that obtained from model I. The SAS of species A (Figure 6.10 (b)) is the same as in model I and decays with the same time constant of ~ 160 fs ($1/(\tau_1^{-1} + \tau_2^{-1})$). Species B in both models decays also with the same time constant (800 fs). The SAS of two species B have approximately the same spectral shape, but different in the overall amplitude. The subsequent reaction of species B has three sequential channels leading to complete product formation in a total time of ~ 20 ps. In model I and II, two D species are identical and are required to fit the offset which is the discrepancy to the static absorption of coumarin monomer, known as long-lived weak contribution from 400 nm to 560 nm.

6.4.2 Electronic state assignment

The almost perfect agreement between the fitting traces based on model I and II in the target analysis and the experimental data enables an assignment of the electronic states of dimers. The SAS and time constant of the initial species A do not differ at all between the two models. After a vertical excitation, the excited state of dimer is populated and decays in 160 fs. The assumption of a single species A, which is assigned to the excited state S_1 of coumarin dimer, is justified by the lack of any strong spectral evolution in the first 200 fs. Note that the intermediate species B is required in both target models with the same life time about 800 fs. The most pronounced difference between the models is located at the branching point. For model I, population flows into the intermediate state B, from here two competing relaxation pathways start off. One is back to the ground state of dimer, the other pathway leading to the formation of monomer products. In model II, branching takes place directly from the Franck-Condon state A. According to the pericyclic reaction, by vertical excitation, population initially leads to the lowest $\pi\pi^*$ state, and flows to the dark two electron excited state via surface crossing. The pericyclic minimum on the two electron excited state acts as a population collection well from where partitioning to the ground state of reactant and products takes place without forming an intermediate state.[23] A significant point to address is whether the cleavage arises from a concerted bond cleavage as displayed in pericyclic reactions, or a successive bond cleavage. If the cleavage process is pericyclic, the branching states of both models play as the pericyclic minimum. In model I, species B acts as pericyclic minimum, where one would expect similar spectral features as species A because they originate from the same potential. However, the large difference of spectra between species A and B is in contrast to the pericyclic reaction. Model II is even more unlikely to be interpreted by pericyclic reaction because at least one intermediate B is involved. Therefore, the actual reaction mechanisms of model I and II are more favour of the view that one-bond cleavage preceded the other. Moreover, the basic semi-empirical calculations of the anti-hh ground state show the HOMO-LUMO levels, and four levels adjacent for each other, show none to very little orbital density across the cyclobutane ring (see Appendix). It does not seem that the initial excited state is coupled to the cyclobutane ring, which further support for non-pericyclic mechanism.

In both models, species C and D have SAS spectra with similar features, which hints they may be originated from the same electronic potential. Because of the agreement between species D and the static absorption of coumarin monomer, species D is assigned to the ground state of monomer products (Figure 6.7). The results of the GTA applied to the syn-hh dimer give almost the same decay times (~19 ps) from species C to D (shown in Table 6.4). For syn-ht dimers, the path C→D is populated within 23 ps, but by fixing the time constant to 19 ps instead, the fit quality of the experimental data is only 0.3% worse. It indicates species C is not strongly isomer dependent, and therefore from here the monomer product is already formed. The cleavage reaction in both models can be interpreted that the UV excitation first causes a bond scission of the cyclobutane ring to generate species B, which subsequently undergoes the second bond cleavage leading to species C. Nevertheless, it is not clear at this stage, whether the monomer product is formed on its excited state by the adiabatic pathway,[171, 172] or directly landed on the high vibrational ground state. In this regard, an additional transient absorption measurement was performed on coumarin monomer in order to observe a complementary photoinduced behaviour. Different from previously reported 330 nm pumping measurements,[154] a shorter pump wavelength at 280 nm was used. A three species based SAS for coumarin monomer is shown in Figure 6.11. Species C of the coumarin monomer is depopulated in about 19 ps, which is reminiscent of the reported lactone ring opening relaxation,[154] and similar to species C of the coumarin dimer. However, comparing the shape and position of species C of the monomer and species C from the dimer, it is still difficult to decide if species C of coumarin dimer can be ascribed to the ring opening state. If the coumarin monomer is formed on the high vibrational ground state, then the time scale of ~ 19 ps is from vibrational cooling in the ground state. Transient changes of the vibrational population in the S_0 ground state give rise to a shifted electronic absorption which can explain the blue shift of species C to D in SAS. After a complete cyclobutane ring cleavage, the redistribution of the excess energy supplied by the pump pulses could stimulate a hot vibrational state, and result in a concomitant relaxation by interaction with the solvent.[173] From this it can be concluded that state C is associated with the coumarin monomer photoproduct, and shall be referred to as a “hot” state.

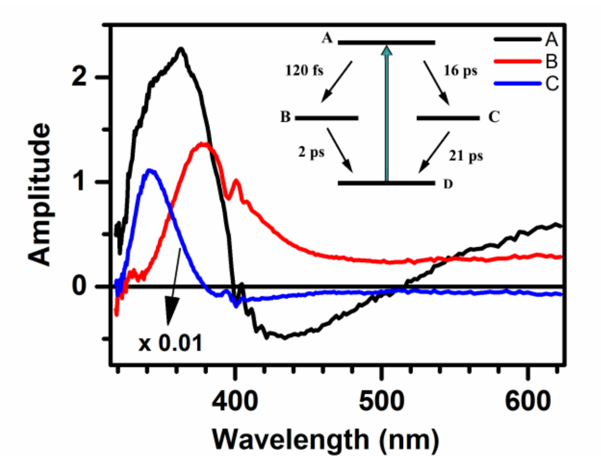

Figure 6.11: Global target analysis results of coumarin monomer

In summary, both models are numerically in good agreement with the experimental results. The quantum yields estimated from the rate constants of GTA, 20.0 % for model I and 22.8 % for model II, are very close to the value of 20.0 % calculated from the experimental TA data. The deactivation from state C to the ground state D of monomers doesn’t differ from models. Model I and II both present the cyclobutane splitting is a successive two C-C bond cleavage process with an intermediate state B. However, intermediate state B in model I has comparatively smaller optical cross-section compared to model II, which is compensated by more abundant population. Two models fail to provide a distinctive global minimum numerical solution, which means that effectively linear combinations can also give the same output fit.

6.4.3 Isomeric effect

The dependence of the quantum efficiency of cleavage reaction on the stereoisomer (Table 6.2) reveals more details of the photocleavage reaction mechanism. The successive two-bond cleavage mechanism can be rationalised on the basis of sterics and radical stabilization, and conveniently permits a simple rational for the difference in cleavage quantum yields between the isomers.

For cyclobutane compounds, the repulsion between the substitution groups can accelerate the bond cleavage by lowering the activation energy.[174] It has also been invoked to explain very large differences between 5-fluorouracil-coumarin crossdimers (Table 6.4).[175] Another mechanism to explain different cleavage reaction yields in cyclobutane compounds is the mesomeric stabilization of charges and resonances.[175] Charge stabilization effect has been observed for oxetanones compounds, where substitution groups may hinder stabilization of charges after initial opening of the cyclobutane ring. In general, resonances and charge delocalization due to different electronegativity of substituents can lead to bond weakening. Both effects, namely charge delocalization as well as repulsion between the substitution groups, explain the difference between the three dimers investigated in this work.

In the anti-hh case, cleavage of the cyclobutane, C-C bond closest to the two ester groups would permit radical formation with resonance stabilization into the ester C=O π-system. Additionally, the anti-facial arrangement gives the smallest degree of steric hindrance as both phenyl groups and C=O are well apart from each other. Conversely, the syn-ht isomer is symmetric across both C-C bonds, and therefore it is kinetically equivalent if either bond is cleaved. However, in the syn-facial arrangement the two coumarin monomer units lie in the same face. This means that when one bond is cleaved there is likely to be larger, steric repulsions between the carbonyl from one unit and the phenyl group of the other. These unfavourable interactions could promote an increase in bond reformation. Additionally, in the syn-ht isomer only one radical can be stabilized by the adjacent ester group, whilst the other radical can only resonate into the adjacent phenyl group. The syn-hh case is midway between the other two isomers: it has the same radical resonance stabilisation as the anti-hh, but similar, unfavourable sterics of the syn-ht isomer. For syn-hh, the carbonyls of both units are in close proximity, and likewise the phenyl groups are also in close, special proximity. From this rationalization, one might expect the quantum yield for ring cleavage to favour: anti-hh>syn-hh>syn-ht. This explanation certainly fits the trend of the experimentally determined quantum yields.

The interplay between charge delocalization and repulsion forces of substitution groups is of course very sensitive to the chemical properties of substitution groups. Nevertheless, our results for unsubstituted coumarin as well as one-photon excitation studies of other coumarin derivatives show that indeed head-to-tail isomers often show a smaller quantum yield than the respective head-to-head isomers.[160, 175] This is even the case for cyclobutane pyrimidine dimers (Table 6.4).[170] This suggests that a general chemistry strategy to optimize the quantum yields of the cleavage of cyclobutane-based compounds in applications should avoid using head-to-tail isomers, but focus on head-to-head isomers in order to weak the cyclobutane bonds.

Table 6.4 Comparison of the cleavage efficiencies (in %) for several dimers of cyclobutane-based compounds and their isomers.

Coumarin Dimers		Coumarin-5-fluorouracil[175]		Cyclobutane Pyrimidine[170]	
Anti-hh	20	Syn-hh	18.9	Syn-hh	3.4
Syn-hh	17.1	Syn-ht	9.2	Anti-hh	0.3
Syn-ht	15.1	Anti-ht	2.9	Anti-ht	Not possible

6.5 Conclusion and outlook

In this work we have investigated the photo-induced cleavage reaction of three coumarin dimer isomers (anti-hh, syn-hh and syn-ht) by using time-resolved femtosecond spectroscopy. The experimental data combined with the global analysis provide a comprehensive picture of the cyclobutane-based cleavage reaction of coumarin dimers (Figure 6.12):

1) In this work, it is confirmed that the mechanism of photocleavage reaction is via non-fluorescent short-lived singlet states. The excited state of coumarin dimers relaxes rapidly in a time constant less than 200 fs.
2) Two branching models are developed which describe the relaxation dynamics of coumarin dimers and suggest the monomer formation is a successive two C-C bonds cleavage process. Independent of the model, the first bond cleavage occurs in less than 200 fs, while the second bond cleaves in a timescale of a few picoseconds, depending on the isomer.
3) The direct cleavage of dimers is characterized by quantum yields of 20.0%, 17.1% and 15.1% for anti-hh, syn-hh and syn-ht dimers, respectively. The values of quantum yield obtained by using the absorption of monomers and rate constants from GTA are in the order of anti-hh > syn-hh > syn-ht. Differences in the observed experimental quantum yields obtained for the three stereoisomers are due to the interplay between stereo forces between substitution groups and charge delocalization leading to C-C bond weakening. With regard to the design of cyclobutane-based linker systems with high cleavage efficiency, head-to-head configuration is of high relevance.

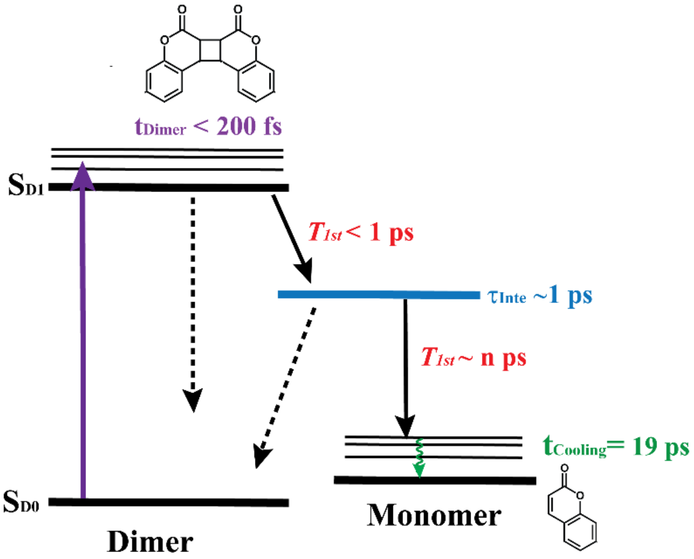

Figure 6.12: Detailed kinetic model for the excited state dynamics of the coumarin dimers and the time constants of monomer formation. The excited state of coumarin dimers relaxes in less than 200 fs. Two kinetic models suggest the population can go back to the ground state either via the excited state of coumarin or the intermediate state. The first bond cleavage takes place in less than 1 ps. The life time of the intermediate state is about 1 ps. The monomer product is formed in a few picoseconds and landed on a “hot” state. The vibrational cooling time is about 19 ps independent of the isomer.

It has to be mentioned though, that two undistinguishable target models which give the same residuals and quality of fits of the experimental data makes the identification of the precise timescale of monomer formation impossible. One possible approach to clarify which model gives a more precise description of the cleavage mechanism is by observing the repopulation of the ground state of coumarin dimers. As shown in Figure 6.13, the ground states E of coumarin dimer in model I and model II are repopulated with different time constants. If the ground state bleach is observed, by comparing the recovery time of the bleach with the time constant derived from the target model it is not difficult to determine the correct mechanism. However, it is necessarily that the ground state bleach is accompanied by a potentially-overlapping band of the excited state absorption. Since the underlying dynamics of the excited state of coumarin dimers has been understood in our study, the identification of the ground state signal wouldn’t be problematic. By the current detection window, we cannot observe the bleach signal. There are two possible ideas to overcome this problem, one is applying the ground-state recovery experiment by using a weak delayed replica of the pump pulse as the probe. The other one is using the supercontinuum generated in CaF_2 under 400 nm pumping, which has been recently realized in our laboratory.

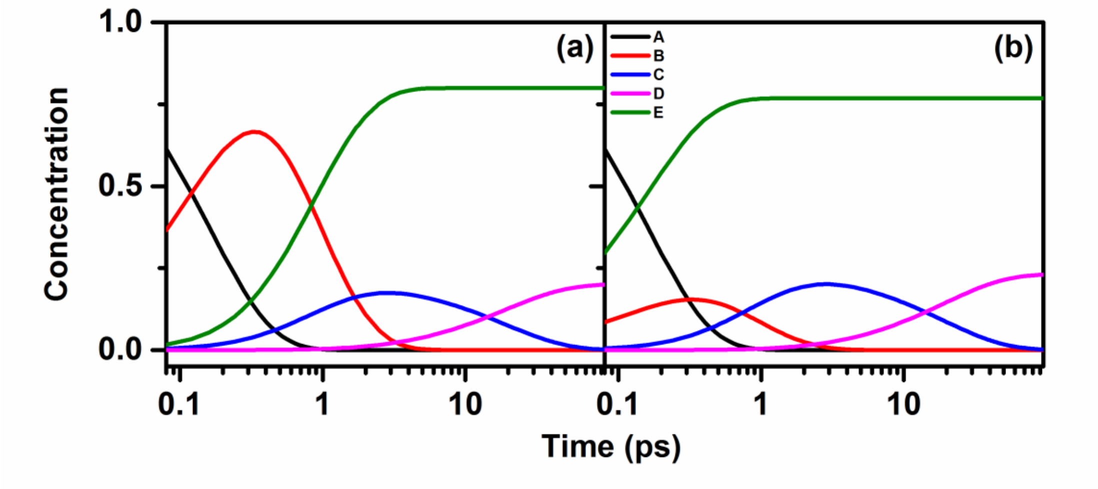

Figure 6.13: Concentration profile of the anti-hh dimer in (a) model I and (b) model II. Curves A-E represent the population evolution of states A-E, respectively. The ground state of coumarin dimers is repopulated with a time constant of 1.01 ps in model I, as described in the green line of (a) and 210 fs in model II, as described in the green line of (b).

Chapter 7

Conclusions and Outlook

7.1 UV transient absorption spectroscopy

In this thesis, a UV-pump/UV-Vis-probe setup with sub-60 fs temporal resolution was successfully developed. For the UV pump pulse, tunable femtosecond pulses were generated based on two nonlinear up-conversion processes: *frequency doubling* of precompressed visible pulses, and *sum frequency generation* between broadband visible pulses and chirped NIR pulses, giving a total tuning range from 250 nm to 350 nm. The duration of the generated UV pulses is overall sub-30 fs and close to the transform limit. Temporal characterization was carried out using a simple autocorrelator based on two-photon absorption in a photomultiplier tube. For probe pulses, the supercontinuum (SC) generated in CaF_2 can cover the spectral range of 300-750 nm and 240-360 nm by simply changing the pump input. Achievable experimental sensitivity was greater than 5×10^{-5} OD. Finally, the whole TA experimental system was tested on the study of ultrafast relaxation of 7-hydroxy coumarin and the solvent effect on its dynamics.

The existing system will serve as a stable, easy to use system to permit studies of a variety of interesting UV absorbing materials. Our system will also act as a platform for future development of nonlinear, UV pulse generating systems. Immediate avenues to pursue, chirp-assisted harmonic generation and sum frequency mixing are efforts to increase both the UV pulse spectral bandwidth, thereby permitting shorter transform limited pulses and increasing the output pulse energies. Type II phase matching and achromatic doubling are also our most likely candidates to explore. Reinvestigation of third harmonic pumped NOPAs, which can give broadband, shorter wavelength (350-500 nm) pulses, may be an interesting line to explore as a direct source for near UV pulses and as sources forming deeper UV pulses (< 240 nm). Successful realization of faster and/or higher frequency UV pulses has huge ramifications for many applied physical sciences. Some immediate examples include blue-emitting LED and lasing technologies and the femtosecond photophysics of UV-induced damage to biological.

7.2 Cleavage reaction of coumarin dimers

In the study of photo-induced cleavage reaction of coumarin dimer, three dimer isomers were excited at 280 nm and probed in the spectral rang of UV and visible (300-650 nm). By using time-resolved spectroscopy, it is the first time experimentally confirmed that the photocleavage reaction occurs through a short-lived nonradiative singlet state in less than 200 fs. After UV excitation only one product was identified for the three isomers, which is the original monomer molecule. With the help of global target analysis, two branching models were developed which suggest the monomer formation is a successive two C-C bonds cleavage process involving with an intermediate state, instead of a concerted process following the pericyclic reaction. This assumption is further rationalized in terms of steric repulsion and charge delocalization, which have great impacts on the quantum yield of cleavage reaction. The anti-hh dimer shows the highest cleavage efficiency with a value of about 20 %, for syn-hh and syn-ht, the values are 17.1 % and 15.1 %, respectively. The difference of quantum yield for the three isomers is originated from the isomeric structure. The anti-facial arrangement gives the smallest degree of steric hindrance between the different parts of the dimer. Charge stabilization of the two ester groups is more favourable to head to head type molecule. As a result, the anti-hh gives the best performance on the cleavage reaction. With regard to the strategy of enhancing the cleavage of coumarin dimers, head-to-head configuration is of high relevance.

Based on the works presented in this thesis, a comprehensive picture of the cyclobutane–based cleavage reaction of coumarin dimers is provided. However, so far, two undistinguishable target models make the identification of the precise timescale of monomer formation impossible. Despite the initial similarity of the two models, they correspond to substantially different dynamics behaviors of the population back to the ground state. By performing ground-state recovery experiment, we will be able to verify which mechanism model is closer to the actual one and therefore identify the timescale of the cleavage reaction. Additionally, although the experimental findings do not support a “pericyclic-type” cleavage mechanism as the HOMO-LUMO levels show none to very little orbital density across the cyclobutane ring, it would be interesting to investigate a different cleavage reaction by exciting the dimer into higher excited states which are coupled to the cyclobutane ring. For a pericyclic cleavage reaction, all bonding changes occur at the same time and in a single step. It can be expected that three isomer will give a similar quantum yield because no intermediate state is involved and the influence of charge delocalization on the radical will be small. For experimental realization, higher photon energies of the pump are required, for example higher than 5 eV. If a broad bandwidth pump is realized successfully, 2-demensional (2D) spectroscopy can be applied. An additional dimension of the excitation frequency allows to investigate the excitation-frequency dependence of the dynamics by observing qualitatively different spectral shape along the pump frequency axis. These above mentioned complementary studies would provide deeper insights into the cleavage reaction of cyclobutane-based molecules.

Bibliography

1. Zewail, A. H., Femtochemistry. Past, present, and future. *Pure Appl Chem* **2000**, 72, 2219-2231.

2. Zewail, A. H., Femtochemistry: Atomic-scale dynamics of the chemical bond. *J Phys Chem A* **2000**, 104, 5660-5694.

3. Zewail, A. H., Femtochemistry: Atomic-Scale Dynamics of the Chemical bond using ultrafast lasers - (Nobel lecture). *Angew Chem Int Edit* **2000**, 39, 2587-2631.

4. Pedersen, S.; Herek, J. L.; Zewail, A. H., The Validity of the Diradical Hypothesis - Direct Femtosecond Studies of the Transition-State Structures. *Science* **1994**, 266, 1359-1364.

5. Reardon, J. T.; Sancar, A., Recognition and repair of the cyclobutane thymine dimer, a major cause of skin cancers, by the human excision nuclease. *Gene Dev* **2003**, 17, 2539-2551.

6. Fenick, D. J.; Carr, H. S.; Falvey, D. E., Synthesis and Photochemical Cleavage of Cis-Syn Pyrimidine Cyclobutane Dimer Analogs. *J Org Chem* **1995**, 60, 624-631.

7. Kao, Y. T.; Song, Q. H.; Saxena, C.; Wang, L. J.; Zhong, D. P., Dynamics and Mechanism of DNA Repair in a Biomimetic System: Flavin-Thymine Dimer Adduct. *J Am Chem Soc* **2012**, 134, 1501-1503.

8. Michl, M. K. a. J., *Excited States and Photochemistry of Organic Molecules*. VCH, New York: 1995.

9. Feldman, D.; Pike, J. W.; Adams, J. S., *Vitamin D: Two-Volume Set*. Elsevier Science: 2011.

10. Dillon, J., The Photophysics and Photobiology of the Eye. *J Photoch Photobio B* **1991**, 10, 23-40.

11. Decker, C., The use of UV irradiation in polymerization. *Polym Int* **1998**, 45, 133-141.

12. Pavia, D. L.; Lampman, G. M.; Kriz, G. S.; Vyvyan, J. A., *Introduction to Spectroscopy*. Cengage Learning: 2008.

13. Orchin, R. A. F. a. M., *Ultraviolet Spectra of Aromatic Compounds*. Wiley, New York: 1951.

14. Reitze, D. H.; Ahn, H.; Downer, M. C., Optical-Properties of Liquid Carbon Measured by Femtosecond Spectroscopy. *Phys Rev B* **1992**, 45, 2677-2693.

15. Cavanagh, R. R.; Germer, T. A.; Heilweil, E. J.; Stephenson, J. C., Time-Resolved Measurements of Substrate to Adsorbate Energy-Transfer. *Faraday Discuss* **1993**, 96, 235-243.

16. Rodriguez, G.; Roberts, J. P.; Taylor, A. J., Ultraviolet Ultrafast Pump-Probe Laser-Based on a Ti-Sapphire Laser System. *Opt Lett* **1994**, 19, 1146-1148.

17. Backus, S.; Peatross, J.; Huang, C. P.; Murnane, M. M.; Kapteyn, H. C., Ti-Sapphire Amplifier Producing Millijoule-Level, 21-Fs Pulses at 1 Khz. *Opt Lett* **1995**, 20, 2000-2002.

18. Cerullo, G.; De Silvestri, S., Ultrafast optical parametric amplifiers. *Rev Sci Instrum* **2003**, 74, 1-18.

19. Kozma, I. Z.; Baum, P.; Lochbrunner, S.; Riedle, E., Widely tunable sub-30 fs ultraviolet pulses by chirped sum frequency mixing. *Opt Express* **2003**, 11, 3110-3115.

20. Baum, P.; Lochbrunner, S.; Riedle, E., Tunable sub-10-fs ultraviolet pulses generated by achromatic frequency doubling. *Opt Lett* **2004**, 29, 1686-1688.

21. Homann, C.; Lang, P.; Riedle, E., Generation of 30 fs pulses tunable from 189 to 240 nm with an all-solid-state setup. *J Opt Soc Am B* **2012**, 29, 2765-2769.

22. Yonezawa, N.; Yoshida, T.; Hasegawa, M., Symmetric and Asymmetric Photocleavage of the Cyclobutane Rings in Head-to-Head Coumarin Dimers and Their Lactone-Opened Derivatives. *J Chem Soc Perk T 1* **1983**, 1083-1086.

23. Fuss, W.; Lochbrunner, S.; Muller, A. M.; Schikarski, T.; Schmid, W. E.; Trushin, S. A., Pathway approach to ultrafast photochemistry: potential surfaces, conical intersections and isomerizations of small polyenes. *Chem Phys* **1998**, 232, 161-174.

24. Fuss, W.; Schmid, W. E.; Trushin, S. A.; Billone, P. S.; Leigh, W. J., Forward and backward pericyclic photochemical reactions have intermediates in common, yet cyclobutenes break the rules. *Chemphyschem : a European journal of chemical physics and physical chemistry* **2007**, 8, 592-598.

25. Dembitsky, V. M., Bioactive cyclobutane-containing alkaloids. *J Nat Med-Tokyo* **2008**, 62, 1-33.

26. Kim, H. C.; Hartner, S.; Behe, M.; Behr, T. M.; Hampp, N. A., Two-photon absorption-controlled multidose drug release: a novel approach for secondary cataract treatment. *Journal of biomedical optics* **2006**, 11.

27. Kim, H. C.; Hartner, S.; Hampp, N., Single- and two-photon absorption induced photocleavage of dimeric coumarin linkers: Therapeutic versus passive photocleavage in ophthalmologic applications. *J Photoch Photobio A* **2008**, 197, 239-244.

28. Backus, S.; Peatross, J.; Zeek, Z.; Rundquist, A.; Taft, G.; Murnane, M. M.; Kapteyn, H. C., 16-fs, 1-mu J ultraviolet pulses generated by third-harmonic conversion In air. *Opt Lett* **1996**, 21, 665-667.

29. Ghotbi, M.; Trabs, P.; Beutler, M., Generation of high-energy, sub-20-fs pulses in the deep ultraviolet by using spectral broadening during filamentation in argon. *Opt Lett* **2011**, 36, 463-465.

30. Fuji, T.; Horio, T.; Suzuki, T., Generation of 12 fs deep-ultraviolet pulses by four-wave mixing through filamentation in neon gas. *Opt Lett* **2007**, 32, 2481-2483.

31. Zuo, P.; Fuji, T.; Suzuki, T., Spectral phase transfer to ultrashort UV pulses through four-wave mixing. *Opt Express* **2010**, 18, 16183-16192.

32. Eimerl, D.; Davis, L.; Velsko, S.; Graham, E. K.; Zalkin, A., Optical, Mechanical, and Thermal-Properties of Barium Borate. *J Appl Phys* **1987**, 62, 1968-1983.

33. Chen, C.; Lin, Z.; Wang, Z., The development of new borate-based UV nonlinear optical crystals. *Appl Phys B-Lasers O* **2005**, 80, 1-25.

34. Zhang, H.; Wang, G.; Guo, L.; Geng, A.; Bo, Y.; Cui, D.; Xu, Z.; Li, R.; Zhu, Y.; Wang, X.; Chen, C., 175 to 210 nm widely tunable deep-ultraviolet light generation based on KBBF crystal. *Appl Phys B-Lasers O* **2008**, 93, 323-326.

35. Yang, J.; Yang, F.; Zhang, J. Y.; Cui, D. F.; Peng, Q. J.; Xu, Z. Y., Pulse broadening of deep ultraviolet femtosecond laser from second harmonic generation in KBe2BO3F2 crystal. *Opt Commun* **2013**, 288, 114-117.

36. Kurdi, G.; Osvay, K.; Csatari, M.; Ross, I. N.; Klebniczki, J., Optical parametric amplification of femtosecond ultraviolet laser pulses. *Ieee J Sel Top Quant* **2004**, 10, 1259-1267.

37. Beutler, M.; Ghotbi, M.; Noack, F.; Brida, D.; Manzoni, C.; Cerullo, G., Generation of high-energy sub-20 fs pulses tunable in the 250-310 nm region by frequency doubling of a high-power noncollinear optical parametric amplifier. *Opt Lett* **2009**, 34, 710-712.

38. Banks, P. S.; Feit, M. D.; Perry, M. D., High-intensity third-harmonic generation in beta barium borate through second-order and third-order susceptibilities. *Opt Lett* **1999**, 24, 4-6.

39. Kummrow, A.; Wittmann, M.; Tschirschwitz, F.; Korn, G.; Nibbering, E. T. J., Femtosecond ultraviolet pulses generated using noncollinear optical parametric amplification and sum frequency mixing. *Appl Phys B-Lasers O* **2000**, 71, 885-887.

40. Baum, P.; Lochbrunner, S.; Riedle, E., Generation of tunable 7-fs ultraviolet pulses: achromatic phase matching and chirp management. *Appl Phys B-Lasers O* **2004**, 79, 1027-1032.

41. Zhao, B. Z.; Jiang, Y. L.; Sueda, K.; Miyanaga, N.; Kobayashi, T., Sub-15fs ultraviolet pulses generated by achromatic phase-matching sum-frequency mixing. *Opt Express* **2009**, 17, 17711-17714.

42. Varillas, R. B.; Candeo, A.; Viola, D.; Garavelli, M.; De Silvestri, S.; Cerullo, G.; Manzoni, C., Microjoule-level, tunable sub-10 fs UV pulses by broadband sum-frequency generation. *Opt Lett* **2014**, 39, 3849-3852.

43. Tzankov, P.; Fiebig, T.; Buchvarov, I., Tunable femtosecond pulses in the near-ultraviolet from ultrabroadband parametric amplification. *Appl Phys Lett* **2003**, 82, 517-519.

44. Dubietis, A.; Jonusauskas, G.; Piskarskas, A., Powerful Femtosecond Pulse Generation by Chirped and Stretched Pulse Parametric Amplification in Bbo Crystal. *Opt Commun* **1992**, 88, 437-440.

45. Wnuk, P.; Stepanenko, Y.; Radzewicz, C., High gain broadband amplification of ultraviolet pulses in optical parametric chirped pulse amplifier. *Opt Express* **2010**, 18, 7911-7916.

46. Darginavicius, J.; Tamosauskas, G.; Piskarskas, A.; Dubietis, A., Generation of 30-fs ultraviolet pulses by four-wave optical parametric chirped pulse amplification. *Opt Express* **2010**, 18, 16096-16101.

47. He, J.; Kobayashi, T., Generation of sub-20-fs deep-ultraviolet pulses by using chirped-pulse four-wave mixing in CaF2 plate. *Opt Lett* **2013**, 38, 2938-2940.

48. Jailaubekov, A. E.; Bradforth, S. E., Tunable 30-femtosecond pulses across the deep ultraviolet. *Appl Phys Lett* **2005**, 87.

49. Nagy, T.; Simon, P., Generation of 200-mu J, sub-25-fs deep-UV pulses using a noble-gas-filled hollow fiber. *Opt Lett* **2009**, 34, 2300-2302.

50. Durfee, C. G.; Backus, S.; Kapteyn, H. C.; Murnane, M. M., Intense 8-fs pulse generation in the deep ultraviolet. *Opt Lett* **1999**, 24, 697-699.

51. Durfee, C. G.; Rundquist, A. R.; Backus, S.; Herne, C.; Murnane, M. M.; Kapteyn, H. C., Phase matching of high-order harmonics in hollow waveguides. *Phys Rev Lett* **1999**, 83, 2187-2190.

52. Rhodes, C. K., Generation of Extreme Ultraviolet-Radiation with Excimer Lasers. *Aip Conf Proc* **1982**, 112-116.

53. Rhodes, C. K., Vacuum Ultraviolet and Extreme Ultraviolet Generation with Excimer Lasers. *Phys Today* **1984**, 37, S42-S43.

54. Rhodes, C. K.; Egger, H.; Johann, U.; Luk, T. S.; Muller, W.; Pummer, H., Extreme-Ultraviolet Generation with Picosecond Excimer Lasers. *J Opt Soc Am A* **1984**, 1, 1262-1262.

55. Mukamel, S., *Principles of nonlinear optical spectroscopy*. Oxford Univ. Press: New York [u.a.], 1995.

56. Zhang, S. K.; Fujita, M.; Yamanaka, M.; Nakatsuka, M.; Izawa, Y.; Yamanaka, C., Study of the stability of optical parametric amplification. *Opt Commun* **2000**, 184, 451-455.

57. Shen, Y. R., *The Principles of Nonlinear Optics*. Wiley: 1984.

58. Shen, Y. R., Recent Advances in Nonlinear Optics. *Rev Mod Phys* **1976**, 48, 1-32.

59. Osvay, K.; Ross, I. N., Broadband sum-frequency generation by chirp-assisted group-velocity matching. *J Opt Soc Am B* **1996**, 13, 1431-1438.

60. Sidick, E.; Dienes, A.; Knoesen, A., Ultrashort-Pulse 2nd-Harmonic Generation .2. Non-Transform-Limited Fundamental Pulses. *J Opt Soc Am B* **1995**, 12, 1713-1722.

61. Sidick, E.; Knoesen, A.; Dienes, A., Ultrashort-Pulse 2nd-Harmonic Generation .1. Transform-Limited Fundamental Pulses. *J Opt Soc Am B* **1995**, 12, 1704-1712.

62. Ellingson, R. J.; Tang, C. L., High-Power, High-Repetition-Rate Femtosecond Pulses Tunable in the Visible. *Opt Lett* **1993**, 18, 438-440.

63. Backus, S.; Asaki, M. T.; Shi, C.; Kapteyn, H. C.; Murnane, M. M., Intracavity Frequency-Doubling in a Ti Sapphire Laser - Generation of 14-Fs Pulses at 416-Nm. *Opt Lett* **1994**, 19, 399-401.

64. Duhr, O.; Nibbering, E. T. J.; Korn, G.; Tempea, G.; Krausz, F., Generation of intense 8-fs pulses at 400 nm. *Opt Lett* **1999**, 24, 34-36.

65. B. Schmidt, M. H., G. Stobrawa, T. Feurer LAB2-A virtal femtosecond laser lab. http://www.lab2.de

66. Diels, J. C. M.; Fontaine, J. J.; Mcmichael, I. C.; Simoni, F., Control and Measurement of Ultrashort Pulse Shapes (in Amplitude and Phase) with Femtosecond Accuracy. *Appl Optics* **1985**, 24, 1270-1282.

67. Ishida, Y.; Yajima, T.; Watanabe, A., A Simple Monitoring-System for Single Subpicosecond Laser-Pulses Using an Sh Spatial Auto-Correlation Method and a Ccd Image Sensor. *Opt Commun* **1985**, 56, 57-60.

68. Ganeev, R. A.; Ganikhanov, F. S.; Gorelik, I. G.; Dakhin, A. A.; Kunin, D. G.; Usmanov, T.; Zinoviev, A. V., Laser-Pulse Duration Measurements in the Range of 0.2 to 50 Picosecond. *Opt Commun* **1995**, 114, 432-434.

69. Isaenko, L. I.; Dragomir, A.; McInerney, J. G.; Nikogosyan, D. N., Anisotropy of two-photon absorption in BBO at 264 nm. *Opt Commun* **2001**, 198, 433-438.

70. Divall, M.; Osvay, K.; Kurdi, G.; Divall, E. J.; Klebniczki, J.; Bohus, J.; Peter, A.; Polgar, K., Two-photon-absorption of frequency converter crystals at 248 nm. *Appl Phys B-Lasers O* **2005**, 81, 1123-1126.

71. Edelstein, D. C.; Wachman, E. S.; Cheng, L. K.; Bosenberg, W. R.; Tang, C. L., Femtosecond Ultraviolet Pulse Generation in Beta-Bab2o4. *Appl Phys Lett* **1988**, 52, 2211-2213.

72. Dadap, J. I.; Focht, G. B.; Reitze, D. H.; Downer, M. C., 2-Photon Absorption in Diamond and Its Application to Ultraviolet Femtosecond Pulse-Width Measurement. *Opt Lett* **1991**, 16, 499-501.

73. Takagi, Y., Simple Autocorrelator for Ultraviolet Pulse-Width Measurements Based on the Nonlinear Photoelectric Effect. *Appl Optics* **1994**, 33, 6328-6332.

74. Wong, K. S.; Sun, T.; Fung, B. K. K.; Sou, I. K.; Wong, G. K. L., Visible to ultraviolet femtosecond autocorrelation measurements based on two-photon absorption using ZnSSe photodetector. *J Cryst Growth* **2001**, 227, 717-721.

75. Kleimeier, N. F.; Haarlammert, T.; Witte, H.; Schuhle, U.; Hochedez, J. F.; BenMoussa, A.; Zacharias, H., Autocorrelation and phase retrieval in the UV using two-photon absorption in diamond pin photodiodes. *Opt Express* **2010**, 18, 6945-6956.

76. Mohring, J.; Buckup, T.; Motzkus, M., Shaper-assisted full-phase characterization of UV pulses without a spectrometer. *Opt Lett* **2010**, 35, 3916-3918.

77. Homann, C.; Krebs, N.; Riedle, E., Convenient pulse length measurement of sub-20-fs pulses down to the deep UV via two-photon absorption in bulk material. *Appl Phys B-Lasers O* **2011**, 104, 783-791.

78. Mohring, J.; Buckup, T.; Lehmann, C. S.; Motzkus, M., Generation of phase-controlled ultraviolet pulses and characterization by a simple autocorrelator setup. *J Opt Soc Am B* **2009**, 26, 1538-1544.

79. Streltsov, A. M.; Ranka, J. K.; Gaeta, A. L., Femtosecond ultraviolet autocorrelation measurements based on two-photon conductivity in fused silica. *Opt Lett* **1998**, 23, 798-800.

80. Rudolph, W.; SheikBahae, M.; Bernstein, A.; Lester, L. F., Femtosecond autocorrelation measurements based on two-photon photoconductivity in ZnSe. *Opt Lett* **1997**, 22, 313-315.

81. Shin, S. I.; Lim, Y. S., Simple Auto correlation Measurement by Using a GaP Photoconductive Detector. *J Opt Soc Korea* **2016**, 20, 435-440.

82. Morita, N.; Yajima, T., A nonlinear correlation method using multiphoton ionization for the measurement of uv ultrashort pulses. *Applied Physics B* **1982**, 28, 25-29.

83. Hutchinson, M. H. R.; Mcintyre, I. A.; Gibson, G. N.; Rhodes, C. K., Measurement of 248-Nm, Subpicosecond Pulse Durations by 2-Photon Fluorescence of Xenon Excimers. *Opt Lett* **1987**, 12, 102-104.

84. Imasaka, T.; Hamachi, A.; Okuno, T.; Imasaka, T., A Simple Method for the Evaluation of the Pulse Width of an Ultraviolet Femtosecond Laser Used in Two-Photon Ionization Mass Spectrometry. *Appl Sci-Basel* **2016**, 6.

85. Reuther, A.; Laubereau, A.; Nikogosyan, D. N., A simple method for the in situ analysis of femtosecond UV pulses in the pump-probe spectroscopy of solutions. *Opt Commun* **1997**, 141, 180-184.

86. Chen, C. T.; Wu, B. C.; Jiang, A. D.; You, G. M., A New-Type Ultraviolet Shg Crystal - Beta-Bab2o4. *Sci Sin B-Chem B a M* **1985**, 28, 235-243.

87. Omenetto, F. G.; Schroeder, W. A.; Boyer, K.; Longworth, J. W.; McPherson, A.; Rhodes, C. K., Measurement of 160-fs, 248-nm pulses by two-photon fluorescence in fused-silica crystals. *Appl Optics* **1997**, 36, 3421-3424.

88. Ihara, K.; Zaitsu, S.; Imasaka, T., Autocorrelator consisting of a solar-blind photomultiplier for use in the near-ultraviolet region. *Rev Sci Instrum* **2005**, 76.

89. Nighan, W. L.; Gong, T.; Liou, L.; Fauchet, P. M., Self-Diffraction - a New Method for Characterization of Ultrashort Laser-Pulses. *Opt Commun* **1989**, 69, 339-344.

90. Schulz, H.; Schuler, H.; Engers, T.; Vonderlinde, D., Measurement of Intense Ultraviolet Subpicosecond Pulses Using Degenerate 4-Wave Mixing. *Ieee J Quantum Elect* **1989**, 25, 2580-2585.

91. Lozovoy, V. V.; Pastirk, I.; Dantus, M., Multiphoton intrapulse interference. IV. Ultrashort laser pulse spectral phase characterization and compensation. *Opt Lett* **2004**, 29, 775-777.

92. Miranda, M.; Arnold, C. L.; Fordell, T.; Silva, F.; Alonso, B.; Weigand, R.; L'Huillier, A.; Crespo, H., Characterization of broadband few-cycle laser pulses with the d-scan technique. *Opt Express* **2012**, 20, 18732-18743.

93. Miranda, M.; Fordell, T.; Arnold, C.; L'Huillier, A.; Crespo, H., Simultaneous compression and characterization of ultrashort laser pulses using chirped mirrors and glass wedges. *Opt Express* **2012**, 20, 688-697.

94. Trebino, R.; DeLong, K. W.; Fittinghoff, D. N.; Sweetser, J. N.; Krumbugel, M. A.; Richman, B. A.; Kane, D. J., Measuring ultrashort laser pulses in the time-frequency domain using frequency-resolved optical gating. *Rev Sci Instrum* **1997**, 68, 3277-3295.

95. Kane, D. J.; Taylor, A. J.; Trebino, R.; Delong, K. W., Single-Shot Measurement of the Intensity and Phase of a Femtosecond Uv Laser-Pulse with Frequency-Resolved Optical Gating. *Opt Lett* **1994**, 19, 1061-1063.

96. Michelmann, K.; Feurer, T.; Fernsler, R.; Sauerbrey, R., Frequency resolved optical gating in the UV using the electronic Kerr effect. *Appl Phys B-Lasers O* **1996**, 63, 485-489.

97. Logothetis, E. M., 2-Photon Photoelectric Spectroscopy in Csi. *Phys Rev Lett* **1967**, 19, 1470-+.

98. Samson, J. A.; Ederer, D. L., *Vacuum Ultraviolet Spectroscopy*. Elsevier Science: 2000.

99. Roth, J. M.; Murphy, T. E.; Xu, C., Ultrasensitive and high-dynamic-range two-photon absorption in a GaAs photomultiplier tube. *Opt Lett* **2002**, 27, 2076-2078.

100. Kozma, I. Z.; Baum, P.; Schmidhammer, U.; Lochbrunner, S.; Riedle, E., Compact autocorrelator for the online measurement of tunable 10 femtosecond pulses. *Rev Sci Instrum* **2004**, 75, 2323-2327.

101. Sheikbahae, M.; Said, A. A.; Wei, T. H.; Hagan, D. J.; Vanstryland, E. W., Sensitive Measurement of Optical Nonlinearities Using a Single Beam. *Ieee J Quantum Elect* **1990**, 26, 760-769.

102. Heisel, P. C.; Bergmann, J.; Paa, W.; Triebel, W.; Zeuner, T.; Stafast, H., 197 nm femtosecond laser-pulse duration: comparison of autocorrelation measurements. *Appl Phys B-Lasers O* **2013**, 112, 49-53.

103. Tomita, Y.; Shibata, M.; Bergquist, J., Pulsewidth Dependence of Time-Resolved 2-Photon Absorption with Picosecond Pump-Probe Excitation. *J Appl Phys* **1992**, 71, 2102-2105.

104. Rosete-Aguilar, M.; Estrada-Silva, F. C.; Bruce, N. C.; Roman-Moreno, C. J.; Ortega-Martinez, R., Calculation of temporal spreading of ultrashort pulses propagating through optical glasses. *Rev Mex Fis* **2008**, 54, 141-148.

105. Alfano, R. R.; Shapiro, S. L., Emission in Region 4000 to 7000 a Via 4-Photon Coupling in Glass. *Phys Rev Lett* **1970**, 24, 584-&.

106. Alfano, R. R.; Shapiro, S. L., Observation of Self-Phase Modulation and Small-Scale Filaments in Crystals and Glasses. *Phys Rev Lett* **1970**, 24, 592-&.

107. Yu, J. W.; Kang, T. J.; Berg, M., Subpicosecond Relaxation of Solvent Perturbations of Nonpolar Electronic States Measured by Transient Hole Burning. *Journal of Chemical Physics* **1991**, 94, 5787-5795.

108. Lozovik, Y. E.; Dobryakov, A. L.; Ernsting, N. P.; Kovalenko, S. A., New method of non-Fermi liquid study by pump-supercontinuum probe femtosecond spectroscopy. *Phys Lett A* **1996**, 223, 303-307.

109. Fork, R. L.; Shank, C. V.; Yen, R.; Hirlimann, C. A., Femtosecond Optical Pulses. *Ieee J Quantum Elect* **1983**, 19, 500-506.

110. Krebs, N.; Pugliesi, I.; Riedle, E., Pulse Compression of Ultrashort UV Pulses by Self-Phase Modulation in Bulk Material. *Appl Sci-Basel* **2013**, 3, 153-167.

111. Wittmann, E.; Bradler, M.; Riedle, E. Direct Generation of 7 fs Whitelight Pulses from Bulk Sapphire. In *Ultrafast Phenomena XIX: Proceedings of the 19th International Conference, Okinawa Convention Center, Okinawa, Japan, July 7-11, 2014*, Yamanouchi, K.; Cundiff, S.; de Vivie-Riedle, R.; Kuwata-Gonokami, M.; DiMauro, L., Eds.; Springer International Publishing: Cham, 2015, pp 725-728.

112. Reed, M. K.; Steinershepard, M. K.; Negus, D. K., Widely Tunable Femtosecond Optical Parametric-Amplifier at 250-Khz with a Ti-Sapphire Regenerative Amplifier. *Opt Lett* **1994**, 19, 1855-1857.

113. Yakovlev, V. V.; Kohler, B.; Wilson, K. R., Broadly Tunable 30-Fs Pulses Produced by Optical Parametric Amplification. *Opt Lett* **1994**, 19, 2000-2002.

114. Dharmadhikari, A. K.; Rajgara, F. A.; Mathur, D., Systematic study of highly efficient white light generation in transparent materials using intense femtosecond laser pulses. *Appl Phys B-Lasers O* **2005**, 80, 61-66.

115. Nagura, C.; Suda, A.; Kawano, H.; Obara, M.; Midorikawa, K., Generation and characterization of ultrafast white-light continuum in condensed media. *Appl Optics* **2002**, 41, 3735-3742.

116. Qin, Y. D.; Wang, D. L.; Wang, S. F.; Gong, Q. H., Spectral and temporal properties of femtosecond white-light continuum generated in H2O. *Chinese Phys Lett* **2001**, 18, 390-392.

117. Brodeur, A.; Chien, C. Y.; Ilkov, F. A.; Chin, S. L.; Kosareva, O. G.; Kandidov, V. P., Moving focus in the propagation of ultrashort laser pulses in air. *Opt Lett* **1997**, 22, 304-306.

118. Brodeur, A.; Chin, S. L., Band-gap dependence of the ultrafast white-light continuum. *Phys Rev Lett* **1998**, 80, 4406-4409.

119. Yang, G. Z.; Shen, Y. R., Spectral Broadening of Ultrashort Pulses in a Nonlinear Medium. *Opt Lett* **1984**, 9, 510-512.

120. Mejean, G.; Kasparian, J.; Yu, J.; Frey, S.; Salmon, E.; Ackermann, R.; Wolf, J. P.; Berge, L.; Skupin, S., UV-supercontinuum generated by femtosecond pulse filamentation in air: Meter-range experiments versus numerical simulations. *Appl Phys B-Lasers O* **2006**, 82, 341-345.

121. Penzkofer, A.; Laubereau, A.; Kaiser, W., Stimulated Short-Wave Radiation Due to Single-Frequency Resonances of Chi-3. *Phys Rev Lett* **1973**, 31, 863-866.

122. Kolesik, M.; Katona, G.; Moloney, J. V.; Wright, E. M., Physical factors limiting the spectral extent and band gap dependence of supercontinuum generation. *Phys Rev Lett* **2003**, 91.

123. Stark, S. P.; Travers, J. C.; Russell, P. S., Extreme supercontinuum generation to the deep UV. *Opt Lett* **2012**, 37, 770-772.

124. Ritucci, A.; Tomassetti, G.; Reale, A.; Arrizza, L.; Zuppella, P.; Reale, L.; Palladino, L.; Flora, F.; Bonfigli, E.; Faenov, A.; Pikuz, T.; Kaiser, J.; Nilsen, J.; Jankowski, A. F., Damage and ablation of large bandgap dielectrics induced by a 46.9 nm laser beam. *Opt Lett* **2006**, 31, 68-70.

125. Brodeur, A.; Chin, S. L., Ultrafast white-light continuum generation and self-focusing in transparent condensed media. *J Opt Soc Am B* **1999**, 16, 637-650.

126. Riedle, E.; Bradler, M.; Wenninger, M.; Sailer, C. F.; Pugliesi, I., Electronic transient spectroscopy from the deep UV to the NIR: unambiguous disentanglement of complex processes. *Faraday Discuss* **2013**, 163, 139-158.

127. Akozbek, N.; Becker, A.; Scalora, M.; Chin, S. L.; Bowden, C. M., Continuum generation of the third-harmonic pulse generated by an intense femtosecond IR laser pulse in air. *Appl Phys B-Lasers O* **2003**, 77, 177-183.

128. Theberge, F.; Liu, W.; Luo, Q.; Chin, S. L., Ultrabroadband continuum generated in air (down to 230 nm) using ultrashort and intense laser pulses. *Appl Phys B-Lasers O* **2005**, 80, 221-225.

129. Johnson, P. J. M.; Prokhorenko, V. I.; Miller, R. J. D., Stable UV to IR supercontinuum generation in calcium fluoride with conserved circular polarization states. *Opt Express* **2009**, 17, 21488-21496.

130. Krebs, N.; Pugliesi, I.; Hauer, J.; Riedle, E., Two-dimensional Fourier transform spectroscopy in the ultraviolet with sub-20 fs pump pulses and 250-720 nm supercontinuum probe. *New J Phys* **2013**, 15.

131. Bradler, M.; Baum, P.; Riedle, E., Femtosecond continuum generation in bulk laser host materials with sub-mu J pump pulses. *Appl Phys B-Lasers O* **2009**, 97, 561-574.

132. Megerle, U.; Pugliesi, I.; Schriever, C.; Sailer, C. F.; Riedle, E., Sub-50 fs broadband absorption spectroscopy with tunable excitation: putting the analysis of ultrafast molecular dynamics on solid ground. *Appl Phys B-Lasers O* **2009**, 96, 215-231.

133. Kartazaev, V.; Alfano, R. R., Polarization properties of SC generated in CaF2. *Opt Commun* **2008**, 281, 463-468.

134. Ernsting, N. P.; Kovalenko, S. A.; Senyushkina, T.; Saam, J.; Farztdinov, V., Wave-packet-assisted decomposition of femtosecond transient ultraviolet-visible absorption spectra: Application to excited-state intramolecular proton transfer in solution. *J Phys Chem A* **2001**, 105, 3443-3453.

135. Shen, Y. R., Self-Focusing: Experimental. *Prog. Quantum Electron.* **1975**, 4, 1.

136. Brazard, J.; Bizimana, L. A.; Turner, D. B., Accurate convergence of transient-absorption spectra using pulsed lasers. *Rev Sci Instrum* **2015**, 86.

137. Berera, R.; van Grondelle, R.; Kennis, J. T. M., Ultrafast transient absorption spectroscopy: principles and application to photosynthetic systems. *Photosynth Res* **2009**, 101, 105-118.

138. Lessing, H. E.; Jena, A. V., Separation of Rotational Diffusion and Level Kinetics in Transient Absorption Spectroscopy. *Chemical Physics Letters* **1976**, 42, 213-217.

139. Buckup, T.; Sarter, C.; Volpp, H. R.; Jaschke, A.; Motzkus, M., Ultrafast Time-Resolved Spectroscopy of Diarylethene-Based Photoswitchable Deoxyuridine Nucleosides. *J Phys Chem Lett* **2015**, 6, 4717-4721.

140. Herz, J.; Buckup, T.; Paulus, F.; Engelhart, J. U.; Bunz, U. H. F.; Motzkus, M., Unveiling Singlet Fission Mediating States in TIPS-pentacene and its Aza Derivatives. *J Phys Chem A* **2015**, 119, 6602-6610.

141. Wolff, T.; Görner, H., Photodimerization of coumarin revisited: Effects of solvent polarity on the triplet reactivity and product pattern. *Phys. Chem. Chem. Phys.* **2004**, 6, 368-376.

142. Kovalenko, S. A.; Dobryakov, A. L.; Ruthmann, J.; Ernsting, N. P., Femtosecond spectroscopy of condensed phases with chirped supercontinuum probing. *Phys Rev A* **1999**, 59, 2369-2384.

143. Alfano, R. R.; Baldeck, P. L.; Ho, P. P.; Agrawal, G. P., Cross-Phase Modulation and Induced Focusing Due to Optical Nonlinearities in Optical Fibers and Bulk Materials. *J Opt Soc Am B* **1989**, 6, 824-829.

144. Lorenc, M.; Ziolek, M.; Naskrecki, R.; Karolczak, J.; Kubicki, J.; Maciejewski, A., Artifacts in femtosecond transient absorption spectroscopy. *Appl Phys B-Lasers O* **2002**, 74, 19-27.

145. Margolin, L. G.; Shashkov, M.; Smolarkiewicz, P. K., A discrete operator calculus for finite difference approximations. *Comput Method Appl M* **2000**, 187, 365-383.

146. Maciejewski, A.; Naskrecki, R.; Lorenc, M.; Ziolek, M.; Karolczak, J.; Kubicki, J.; Matysiak, M.; Szymanski, M., Transient absorption experimental set-up with femtosecond time resolution. Femto- and picosecond study of DCM molecule in cyclohexane and methanol solution. *J Mol Struct* **2000**, 555, 1-13.

147. Klimov, V. I.; McBranch, D. W., Femtosecond high-sensitivity, chirp-free transient absorption spectroscopy using kilohertz lasers. *Opt Lett* **1998**, 23, 277-279.

148. Wohlleben, W.; Buckup, T.; Herek, J. L.; Cogdell, R. J.; Motzkus, M., Multichannel carotenoid deactivation in photosynthetic light harvesting as identified by an evolutionary target analysis. *Biophys J* **2003**, 85, 442-450.

149. Marquardt, D. W., An Algorithm for Least-Squares Estimation of Nonlinear Parameters. *J Soc Ind Appl Math* **1963**, 11, 431-441.

150. Istratov, A. A.; Vyvenko, O. F., Exponential analysis in physical phenomena. *Rev Sci Instrum* **1999**, 70, 1233-1257.

151. Golub, G. H.; Van Loan, C. F., *Matrix Computations*. Johns Hopkins University Press: 1996.

152. van Stokkum, I. H. M.; Larsen, D. S.; van Grondelle, R., Global and target analysis of time-resolved spectra. *Bba-Bioenergetics* **2004**, 1657, 82-104.

153. van Wilderen, L. J. G. W.; Lincoln, C. N.; van Thor, J. J., Modelling Multi-Pulse Population Dynamics from Ultrafast Spectroscopy. *PLoS One* **2011**, 6.

154. Krauter, C. M.; Mohring, J.; Buckup, T.; Pernpointner, M.; Motzkus, M., Ultrafast branching in the excited state of coumarin and umbelliferone. *Phys Chem Chem Phys* **2013**, 15, 17846-17861.

155. Heldt, J. R.; Heldt, J.; Stori, M.; Diehl, H. A., Photophysical Properties of 4-Alkylcoumarin and 7-Alkoxycoumarin Derivatives - Absorption and Emission-Spectra, Fluorescence Quantum Yield and Decay Time. *Spectrochim Acta A* **1995**, 51, 1549-1563.

156. Murdock, D.; Ingle, R. A.; Sazanovich, I. V.; Clark, I. P.; Harabuchi, Y.; Taketsugu, T.; Maeda, S.; Orr-Ewing, A. J.; Ashfold, M. N. R., Contrasting ring-opening propensities in UV-excited alpha-pyrone and coumarin. *Phys Chem Chem Phys* **2016**, 18, 2629-2638.

157. Joswig, J. O.; Lorenz, T.; Seifert, G., Photoexcitation in Dimers of Coumarin and 6-Alkylcoumarins. *Z Phys Chem* **2014**, 228, 243-251.

158. D'Auria, M.; Racioppi, R., The photodimerisation of coumarin. *J Photoch Photobio A* **2004**, 163, 557-559.

159. Yonezawa, N.; Yamashita, T.; Kanoe, T.; Saigo, K.; Hasegawa, M., Application of Anisotropic Photocleavage of Head-to-Head Type Cyclobutane Compounds. *Ind Eng Chem Prod Rd* **1985**, 24, 593-598.

160. Wolff, T.; Görner, H., Photocleavage of dimers of coumarin and 6-alkylcoumarins. *Journal of Photochemistry and Photobiology A: Chemistry* **2010**, 209, 219-223.

161. Buckup, T.; Dorn, J.; Hauer, J.; Hartner, S.; Hampp, N.; Motzkus, M., The photoinduced cleavage of coumarin dimers studied with femtosecond and nanosecond two-photon excitation. *Chemical Physics Letters* **2007**, 439, 308-312.

162. Buckup, T.; Southan, A.; Kim, H. C.; Hampp, N.; Motzkus, M., Optimisation of two-photon induced cleavage of molecular linker systems for drug delivery. *Journal of Photochemistry and Photobiology A: Chemistry* **2010**, 210, 188-192.

163. R. B. Woodward, R. H., The Conservation of Orbital Symmetry. *Angew Chem Int Edit* **1969**, 8, 781-932.

164. Fuss, W.; Panja, S.; Schmid, W. E.; Trushin, S. A., Competing ultrafast cis-trans isomerization and ring closure of cyclohepta-1,3-diene and cyclo-octa-1,3-diene. *Mol Phys* **2006**, 104, 1133-1143.

165. Kobashi, H.; Ikawa, H.; Kondo, R.; Morita, T., Effect of Conformation on Ring-Opening of Cis and Trans Dimers of Acenaphthylene in the Triplet-State - Direct Detection of Hydrocarbon Biradical, 1,1'-Biacenaphthene-2,2'-Diyl. *B Chem Soc Jpn* **1982**, 55, 3013-3018.

166. Tsuchida, A.; Yamamoto, M.; Nishijima, Y., Laser Photolysis Studies on [2+2]-Photocycloreversion and Photoisomerization Reactions of Trans-1,2-Di(1-Pyrenyl)Cyclobutane and Cis-1,2-Di(1-Pyrenyl)Cyclobutane Dimers through Radical Ion Intermediates. *B Chem Soc Jpn* **1991**, 64, 3402-3410.

167. Kim, H. C.; Kreiling, S.; Greiner, A.; Hampp, N., Two-photon-induced cycloreversion reaction of coumarin photodimers. *Chemical Physics Letters* **2003**, 372, 899-903.

168. Crozet, P., Triplet-Triplet Absorption of Coumarin and 7-Hydroxycoumarin. *Chem Phys Lett* **1974**, 25, 114-118.

169. Wolff, T.; Gorner, H., Photodimerization of coumarin revisited: Effects of solvent polarity on the triplet reactivity and product pattern. *Phys Chem Chem Phys* **2004**, 6, 368-376.

170. Epple, R.; Wallenborn, E. U.; Carell, T., Investigation of flavin-containing DNA-repair model compounds. *J Am Chem Soc* **1997**, 119, 7440-7451.

171. Yang, N. C.; Chen, M. J.; Chen, P., Chemistry of Benzene Anthracene Cyclodimers. *J Am Chem Soc* **1984**, 106, 7310-7315.

172. Albini, A.; Fasani, E., Adiabatic and Charge-Transfer Pathways in the Photocleavage of Dimers and Cycloadducts of Some Aromatic-Molecules. *J Am Chem Soc* **1988**, 110, 7760-7763.

173. Elsaesser, T.; Kaiser, W., Vibrational and Vibronic Relaxation of Large Polyatomic-Molecules in Liquids. *Annual Review of Physical Chemistry* **1991**, 42, 83-107.

174. Schaumann, E.; Ketcham, R., 2+2 -Cycloreversions. *Angew. Chem.-Int. Edit. Engl.* **1982**, 21, 225-247.

175. Behrendt, P. J.; Kim, H. C.; Hampp, N., Photochemical cleavage of individual stereoisomers of coumarin-5-fluorouracil crossdimers via single- and two-photon-absorption. *Chemical Physics Letters* **2013**, 588, 91-96.

Appendix

A. Global target analysis of syn-hh and syn-ht dimers

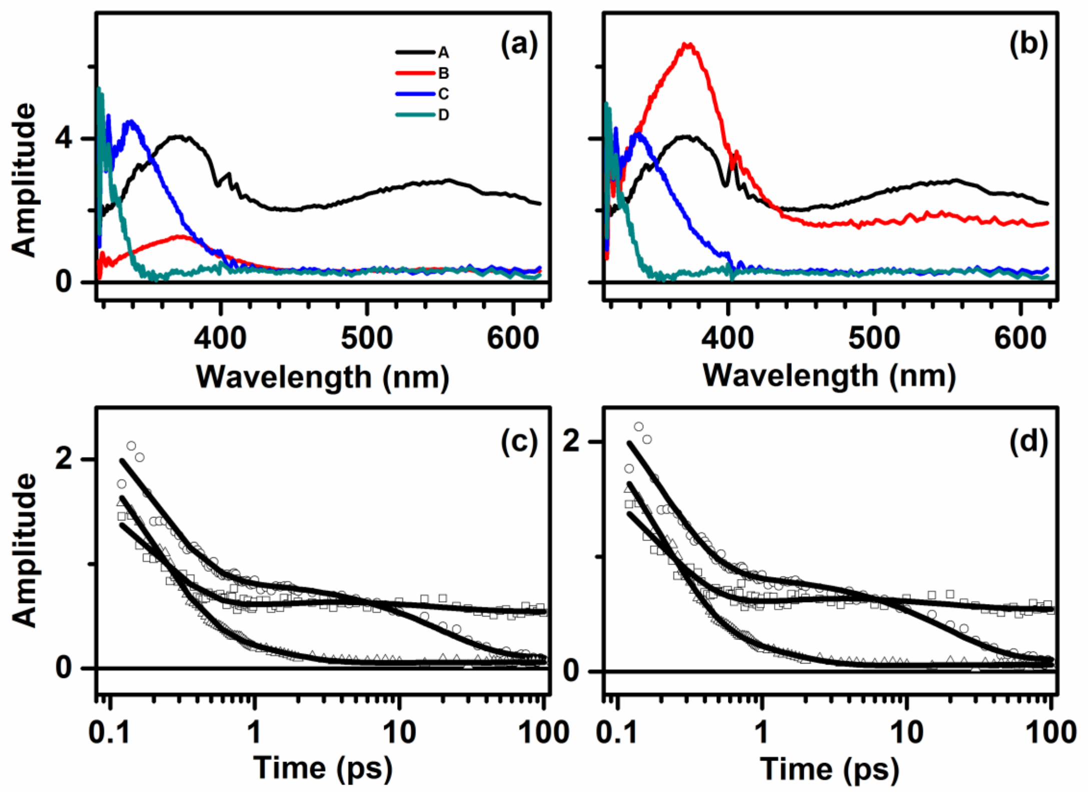

A.1: Global target analysis results of syn-hh dimer: SAS obtained for (a) model I and (b) model II, transient absorption traces for (c) model I and (d) model II. Open points are experimental data, lines are obtained from the global target analysis.

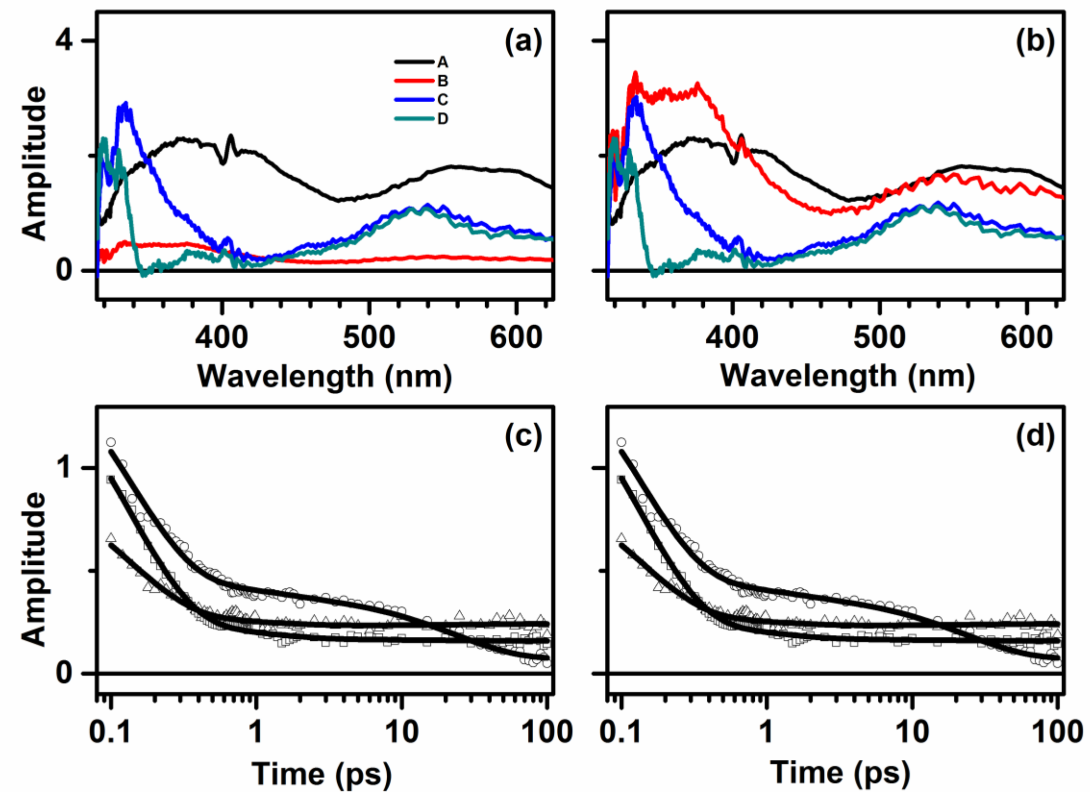

A.2: Global target analysis results of syn-ht dimer: SAS obtained for (a) model I and (b) model II, transient absorption traces for (a) model I and (b) model II. Open points are experimental data, lines are obtained from the global target analysis.

B. Computational calculations of anti-hh dimer

Calculations were performed using the freely available ArgusLab (4.0.1, 2004 Mark Thompson and Planaria Software) package. Geometry optimization was performed in a step wise manner. Molecular mechanics (Unified Force Field, UFF) was used to relax the geometry to a local, ground state minimum. After successful minimization, semi-empirical methods using the PM3 model were used to further minimize the equilibrium geometry. Careful attention was paid to ensure the cyclobutane ring was in the expected, distorted, “boat” geometry. Optimizations were susceptible to local minima where the cyclobutane ring is in the higher energy, flat arrangement. Once completed, the energies and molecular orbitals were generated.

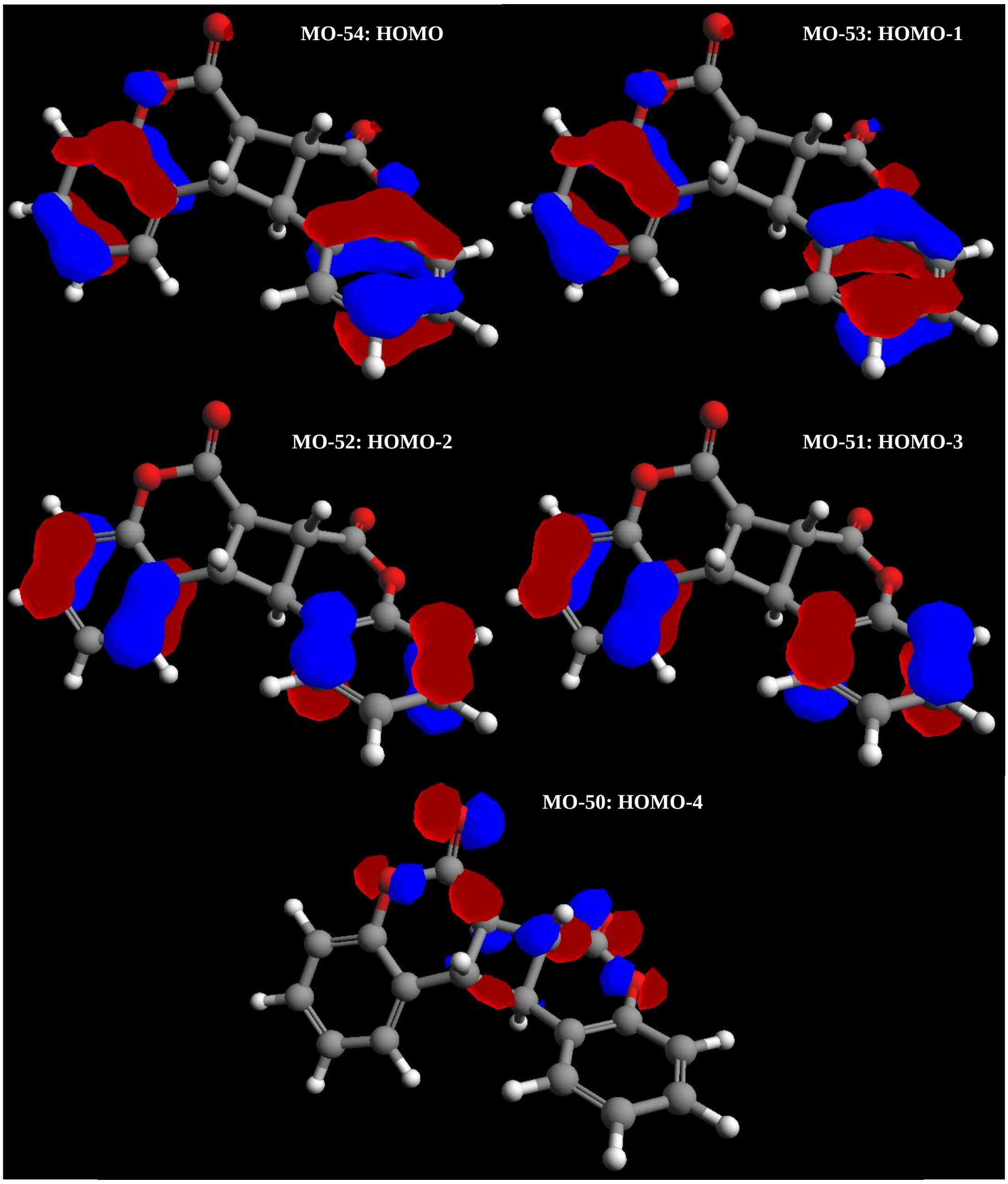

B.1: Occupied, ground state molecular orbitals for the anti-hh dimer in its relaxed (energy minimum) geometric arrangement.

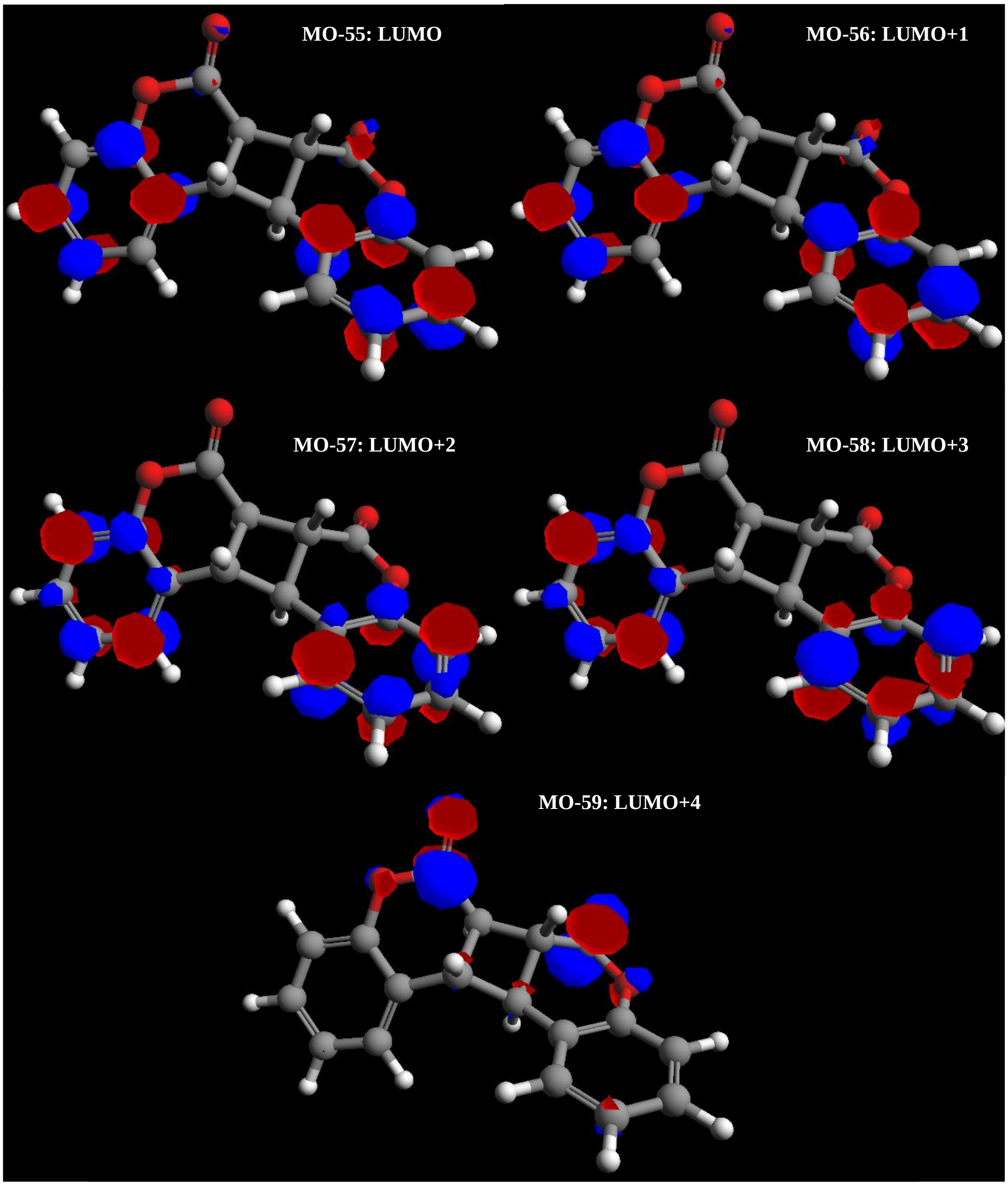

B.2: Vacant, ground state molecular orbitals for the anti-hh dimer in its relaxed (energy minimum) geometric arrangement.

Acknowledgement

First of all, I would like to thank Deutscher Akademischer Austauschdienst for the financial support during the three and half years of my PhD study.

I would like to express my sincerest appreciation to my supervisor Prof. Marcus Motzkus, for giving me the opportunity to pursue my PhD study in the topic of UV transient absorption spectroscopy, and for keeping me on the right track throughout my research. He endowed me with considerable freedom for developing my ideas during the time of building the UV lab. I want to sincerely acknowledge him for his immense patience and guidance.

I also would like to thank Prof. Thomas Pfeifer who kindly agreed to be my second referee of this thesis. I am thankful for his time invested in reading my thesis. I am grateful to Prof. Thomas Gasenzer and Prof. Annemarie Pucci for agreeing to be my examiners of the final examination.

Starting with an empty lab, starting with no working experience with spectroscopy, without the guidance of Dr. Tiago Buckup, it would be impossible to build up the entire UV lab. It is him who provides a lot of inspiring ideas and discussions throughout my study. Besides of being an excellent supervisor, Tiago was as close as a good friend to me.

Many thanks for Prof. Hans-Robert Volpp, for the nice laser safety conversation on my first days in Heidelberg and all these inspiring questions in seminar talks.

A huge thanks goes to our postdoc. Dr. Nick Paul for following the coumarin-dimer project from the beginning of the experiment to the paper writing, and having dedicated lots of time in teaching me chemistry and answering all the questions in very fine details. Moreover, I profit a lot from his experience by providing me useful hints to my thesis.

I offer my cordially thanks to all my current and former group members for their helps during my doctoral study, and their kindly tolerance and patience for my temper during the stressful period. Special thanks to Dr. Julia Herz for always being a big sister to me, and it is great fun to work with Julia as a colleague and a friend. I thank Lukas Brückner for providing valuable suggestions related to the Labview programming and sharing the joy of successes with me. Thanks a lot to Elisabeth Brühl for helping my German abstract, and I enjoyed our working time as much as our funny chats. I thank Takeshi Miki for offering me helps on moving heavy electronic instruments in the lab and always being

kind to everyone. I also would like to thank my officemates Partha Roy who answers my dummy chemistry questions and gives me the best office atmosphere when I buried my head in the thesis, and Nicolo Alagna, for the efforts to make me laugh and save me from being panic. Many thanks to my first officemate Dr. Alexander Wipfler, he has been one of the most friendly face I have met here. Thanks a lot to Cinzia Emmanuello and Mariana Ishikawa for the delicious chocolates and tiramisus, as well as these sweet girl's talks we had. Additionally, I want to thank Daniel Gerz and Andreas Lugwig for making my days at work more pleasant. I extend my acknowledgments to my former colleagues Dr. Jean Rehbinder, Dr. Philip Kraack, Dr. Marie Marek and Dr. Sajjad Hoseinkhani for helpful conversations.

Special thanks to our secretary Ms. Sylvia Boganski for taking care of me as own daughter during these years in Heidelberg. I thank Sylvia for the beautiful birthday presents every year, for these warm hugs when I am exhausted or sad, for all these small "lectures" when I made mistakes by my own naivety. I also thank Ms. Angelika Neuner, for being so kind and available for any questions and problems, and saving me from the time-consuming bureaucracy.

Finally, to my dear sister, I cannot thank you more for loving me and supporting me. I would need a whole other list to thank you properly. My deepest gratitude is for my parents: we love you forever.

Eidesstattliche Erklärung

Bei der vorliegenden Dissertation handelt es sich um meine eigenständig erbrachte Leistung. Ich habe nur die angegebenen Quellen und Hilfsmittel benutzt und mich keiner unzulässigen Hilfe Dritter bedient. Insbesondere habe ich wörtlich oder sinngemäß aus anderen Werken übernommene Inhalte als solche kenntlich gemacht.

Heidelberg, 27. November 2016

Man Jiang